Studies of the Spectroscopy and Collision Dynamics of some Ion-Pair States of I_2 using Laser Optical-Optical Double Resonance Excitation

by

Andrew J. Holmes

Doctor of Philosphy

University of Edinburgh

1989

To my wife Helen, with love.

Declaration

I hereby declare that I have composed this thesis and the work described is my own and was carried out at the University of Edinburgh, except where due acknowledgement is made.

Signature:

Date: 13/2/89

Acknowledgements

Firstly, I would like to thank my two research supervisors, Professor Robert Donovan and Dr. Patrick Langridge-Smith for their advice and encouragement throughout the course of my PhD studies. I also wish to thank Dr. Trevor Ridley, without whose assistance the experimental work described in this thesis could not have been carried out. In addition, I also appreciate the many helpful conversations with Dr. Kenneth Lawley on theoretical aspects of ion-pair state spectroscopy and quenching, and also for access to the spectroscopic simulation programme, "SPECFUSE".

I have found the laser spectroscopy group at the University of Edinburgh a critical and stimulating enviroment and I wish to record my thanks to the many members of the group, past and present, with whom I have been privileged to work.

Throughout the course of my studies, I have made extensive use of the computing facilties at the University of Edinburgh and I extend my thanks to all those people responsible for this fine service. The EMAS-SCRIBE word-processing package was used to prepare this thesis and I am indebted to Roger Hare for allowing me to use his private SCRIBE database.

Finally, I would like to thank my wife Helen for her help in typing and preparing this thesis and also for her patience throughout the last five months.

Abstract

The spectroscopy of the $f(0_g^+)$ ion-pair state of I_2 was studied in detail and dispersed fluorescence spectra obtained for a range of single rovibronic levels, up to v'=88. The electronic transition dipole moment function, $\mu_{21}(r)$, has been determined from direct simulation of the transition $f(0_g^+, v'=88, J'=70) \rightarrow B(0_u^+, v''=n)$. $\mu_{21}(r)$ displays a maximum close to r_e for the f state, but decreases on going to smaller and larger internuclear separations. This has been explained using LCAO and separated-ion descriptions for the molecular electronic wavefunctions.

Product state vibrational distributions have been determined for collisional relaxation of $I_2(f0_g^+)$ by $I_2(X0_g^+)$. These distributions are interpreted in terms of an orbiting-controlled and a long range resonant model for the transfer into the $F(0_u^+)$ state.

New fluorescence emission systems have been observed following excitation of the lowest vibrational levels of the $E(0_g^+)$, $\beta(1_g)$, $\gamma(1_u)$ ion-pair states of I_2. These systems have been assigned from measurements of line positions and by direct spectral simulations. Following this, several previously unidentified features in the emission spectrum of I_2, in the presence of argon, have been assigned.

Finally, the excitation function for formation of $XeI^*(B^2\Sigma_{1/2})$, following OODR excitation of Xe/I_2 mixtures, has been measured as a function of vibrational level in the $f(0_g^+)$ ion-pair state. State-specific rate constants for reaction and total removal have

been estimated, assuming a radiative lifetime of 20 ns for the $f(0_g^+)$ state. These indicate that the branching ratio for reaction is a function of excitation energy. A simple harpooning model was employed in order to explain the observation that the yield of XeI^* increases as a function of vibronic energy.

Table of Contents

Chapter 1
INTRODUCTION

1.1 The Ion-Pair States of I_2

The ion-pair states of I_2 which may be excited using ultraviolet and vacuum ultraviolet radiation diabatically dissociate to $I^+5s^25p^4$ and $I^-5s^25p^6$ and lie at energies between 40000 and 50000cm^{-1} above the $X(0_g^+)$ ground valence state. These states are characterised by potential curves having long, shallow attractive limbs arising from the long range Coulombic attraction between the ions. Accordingly, they are deeply bound (D_e>30000cm^{-1}) and support excited vibrational states which have very large amplitudes of motion. Many of these states lie below the first known Rydberg state of I_2 ($^2\Pi_{3/2}$; $6s\sigma_g$, 2_g), but, as they have greater diabatic dissociation limits, are expected to mix with the Rydberg states at large internuclear separations.

1.2 Clustering of the ion-pair states of I_2

The dominant contribution to the potential energy of halogen ion-pair states , X^+X^-, at long range, arises from the $-e^2/r$ electrostatic attraction term. This applies to all ion-pair states and hence the potential energy curves for these states are all expected to possess attractive limbs of similiar gradient, with those of shared ionic parentage being closely grouped together. In the case of the diatomic halogens, the anionic parent, $X^-(^1S_0)$, is common to all of the ion-pair states which can be accessed by UV and VUV excitation. Thus, the ion-pair states of these molecules are clustered together according to the energy of the X^+ ion. The lowest lying states of I^+ are ^3P, ^1D and ^1S. The $^3P_2$ and $^1D_2$ configurations are partially mixed[1], as are the $^3P_0$ and $^1S_0$ states, distorting the ionic spacings

FIGURE 1.1

Potential curves for the valence and ion-pair states of I_2 (schematic).

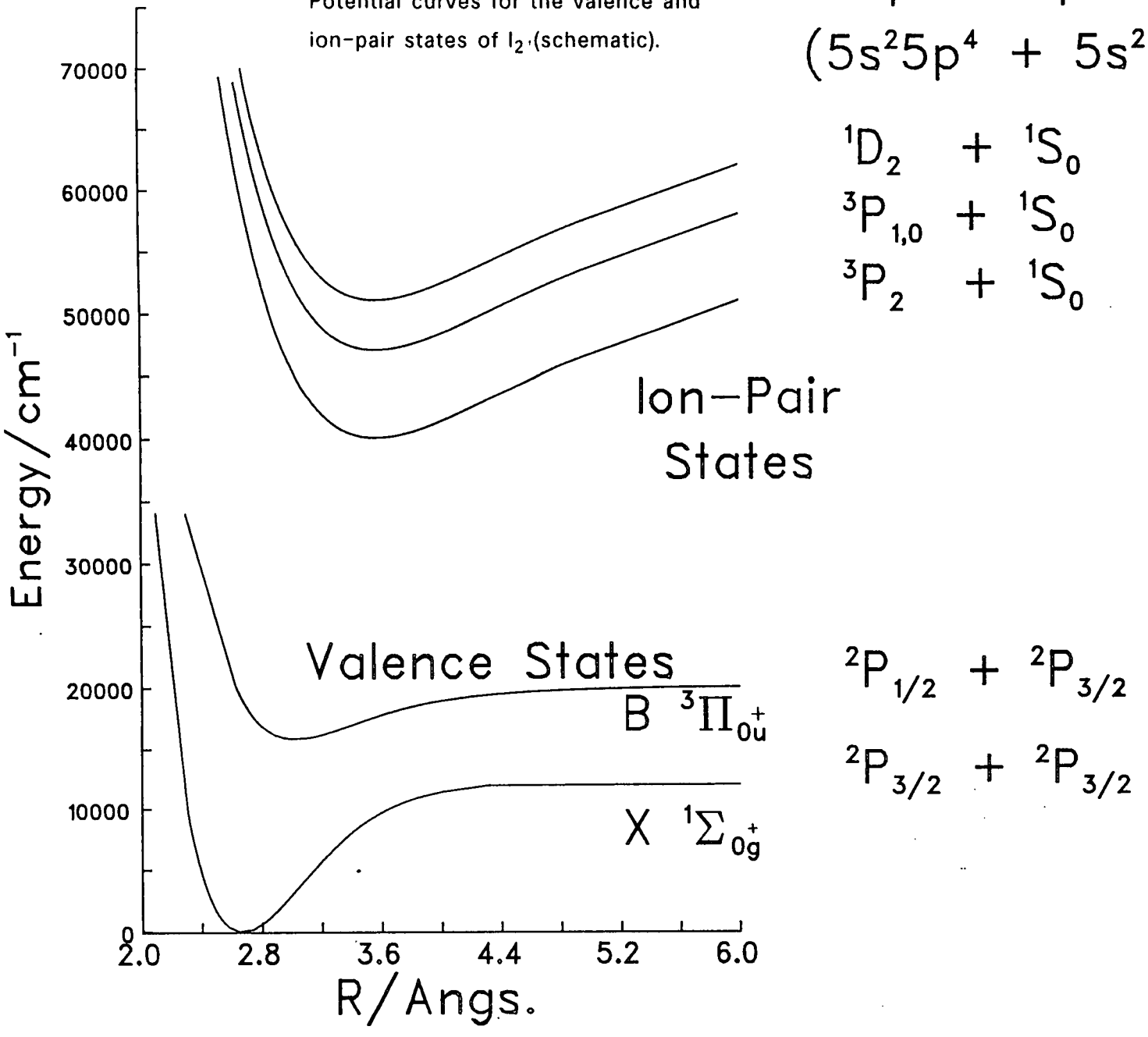

with the result that the $^3P_0$ and $^3P_1$ states lie ca. 7000cm^{-1} higher than $^3P_2$. $I^+(^1D_2)$ is higher still by ca. 7000cm^{-1} (see Figure 1) . On this basis, Mulliken predicted three clusters of six ion-pair states each correlating with $I^+(^3P_2)$, $I^+(^3P_{0,1})$ and $I^+(^1D_2)$ [2]. With two states arising from $I^+(^1S_0)+I^-(^1S_0)$ lying at much higher energies, this gives twenty ion-pair states in total. When Mulliken originally predicted clustering of ion-pair states, there was insufficent experimental knowledge of the potential curves of the halogens to verify his proposal. A great deal of experimental evidence now gives support to this picture for all homo- and heteronuclear diatomic halogen molecules (see Figure 2) . Table 1.1 summarises the known spectroscopic constants for the ion-pair states of I_2. It can be clearly seen from this table that the T_e values for the known ion-pair states lie in three distinct groups.

Further evidence in favour of the clustering model comes from the determination of the ionic parentage of the states within these groups. It has been shown that the potential curves for these molecules can be fitted to the "truncated-Rittner" expansion, derived by Brumer and Karplus[15] to model the ionic ground states of alkali halide molecules.

$$V(r) = T_\infty + Aexp(-br) - e^2/r - (\alpha_a-\alpha_b)/2r^4 - C_6/r^6 \quad (1.1)$$

where r=interionic distance, α = ion polarizability and C_6/r_6 is the London approximation to the Van der Waals attraction. The term Aexp(-br) is empirically derived to describe the repulsive limb of the potential. The various constants in equation (1.1) are all known for I^+ and I^-[6] and hence, experimental potential curves for the ion-pair

Table 1.1

Summary of the principal spectroscopic constants for the ion-pair states of I_2

State	$T_e(cm^{-1})$	$\omega_e(cm^{-1})$	$r_e(Å)$	Diss. Limit	Refs.
$F'(0_u^+)$	51706.2	131.0	3.48	$^1S_0 + {}^1D_2$	13,15
$f'(0_g^+)$	(51400)	(100±3)		"	14
$G(1_g)$	47559.1	106.6	3.53	$^1S_0 + {}^3P_1$	12
$F(0_u^+)$	47217.4	96.3	3.60	$^1S_0 + {}^3P_0$	10,11
0_g^-	47070	105.7	3.55	$^1S_0 + {}^3P_1$	9
$f(0_g^+)$	47025.9	104.2	3.57	$^1S_0 + {}^3P_0$	8
$\delta(2_u)$	41789	100.2	4.0	$^1S_0 + {}^3P_2$	7
$\gamma(1_u)$	41621.3	95.0	3.68	"	7
$E(0_g^+)$	41411.8	101.4	3.65	"	6
$D(0_u^+)$	41028.6	95.0	3.58	"	5
$\beta(1_g)$	40821.0	105.0	3.61	"	4
$D'(2_g)$	40388.3	104.0	3.61	"	3

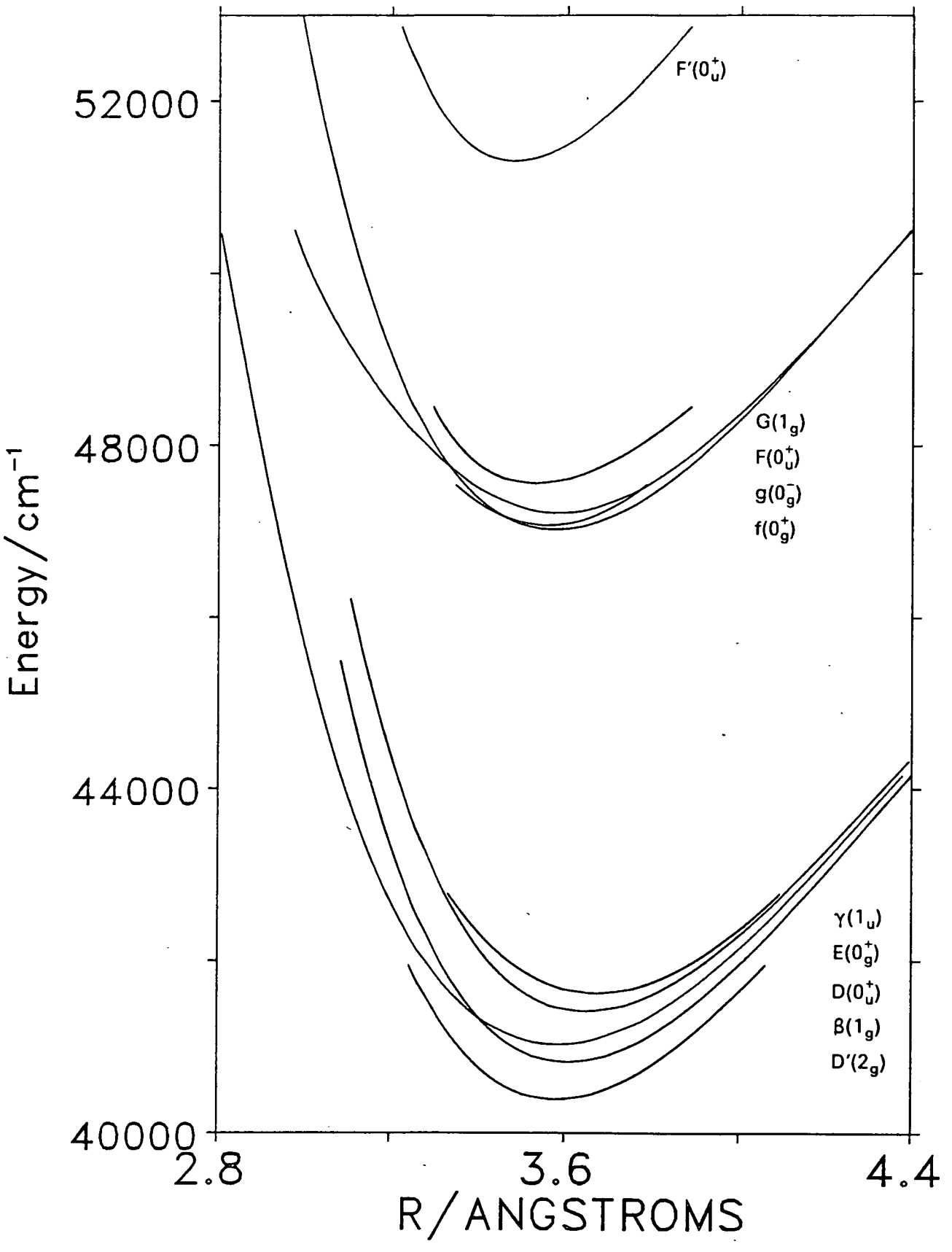

FIGURE 1.2

Known potential curves for the ion-pair states of I_2 [3–15].

states of I_2 can be tested to see if they obey the "truncated-Rittner" function. A value of T_∞ for the ion-pair state being tested can be derived, where:

$$T_\infty = T_e + D_e \qquad (1.2)$$

T_e is the energy of the ion-pair potential minimum relative to that of the X state and D_e is the diabatic dissociation energy. This analysis has been applied to the $E(0_g^+)$, $\beta(1_g)$, $f(0_g^+)$ and $G(1_g)$ states of I_2 by Brand et al[6,15]. The E and β states lie in the lowest experimentally observed cluster and hence are expected to correlate with $I^+(^3P_2)$, whilst the f and G states are in the second cluster and should correlate with $I^+(^3P_0)$ and $I^+(^3P_1)$, respectively. The results clearly show that the four curves have very similiar attractive limbs, with the E and β states having values of T_∞ which lie very close to the asymptotic value for $I^+(^3P_2)+I^-(^1S_0)$, whilst the f and G states appear to dissociate to $I^+(^3P_{0,1})+I^-(^1S_0)$. This procedure has been applied to the known ion-pair states of other halogen diatomics, with equally positive results. Indeed, it is now standard practice to extend the potential curves for ion-pair states outside the experimentally determined regions by using the Rittner function.

1.3 Experimental studies of the ion-pair states of I_2

The first observations of emission in the ultraviolet from I_2 were reported by McLennan in 1913[16]. Gaseous I_2 was excited with atomic radiation from a mercury arc lamp and extensive diffuse emission in the 250-500nm wavelength range was recorded. It was not until 1971, however, that the first convincing assignments of

these bands were made by Mulliken[2]. In particular, the strong system with a red extremum close to 325nm was assigned as fluorescence from the $D(0_u^+)$ ion-pair state of I_2 to the $X(0_g^+)$ ground state.

The ultraviolet absorption spectrum of I_2 shows a closely spaced series of bands in the region 170-200nm which have been assigned to absorption from the ground state into the $D(0_u^+)$ state [2]. However, until recently the D state was the only ion-pair state identified from the absorption spectrum, out of the 9 ungerade ion-pair states expected to lie at energies between 40000 and 50000cm^{-1}. Transitions to the other 8 states are either forbidden or expected to have very weak transition dipole moments. Donovan and co-workers have recently demonstrated that the $F(0_u^+)$ and $F'(0_u^+)$ states can also be excited, following single photon absorption at 169 and 158nm respectively[17,18].

Prior to 1974, the most successful studies of ion-pair states employed discharge tubes. Tellinghuisen and co-workers identified several ion-pair states of I_2 by analysing emission from isotopically pure I_2 samples, following discharge excitation. The $E(0_g^+)$, $D(0_u^+)$, $D'(2_g)$ and $F(0_u^+)$ states of I_2 have all been observed using this technique, and the salient details of their potential energy curves elucidated [19-23,3]. The dispersed fluorescence spectra contain contributions from many rovibronic states, thus requiring a highly detailed analysis in order to obtain accurate information on the emitting states. To overcome this, Tellinghuisen and co-workers employ high resolution photography of the dispersed emission,

coupled with the use of isotopically pure samples. The apparatus required is relatively simple and by varying the experimental conditions, information can be obtained on a number of ion-pair states. To date the $G(1_g)$ and $g(0_g^-)$ states of I_2 have only been observed using discharge techniques[9,12]. Discharge excitation is now being utilised to characterise the ion-pair states of a wide range of other halogen and interhalogen diatomics.

The advent of lasers and the optical-optical double resonance technique in particular (sec. 1.7), has greatly aided the study of halogen ion-pair states. Six new ion-pair states of I_2 have been observed for the first time using OODR and the known potential curves for many of the other states have been greatly extended. Figure 1.2 shows the potential curves for the known ion-pair states of I_2. The first reported OODR experiment on I_2 was carried out by Rosseau and Williams, using a continuous wave (CW) UV dye laser coupled with a Krypton-ion laser[24]. The dye laser was tuned over a range of I_2 B $\leftarrow$ X rovibronic transitions, whilst the fixed frequency ion laser pumped the excited molecules to the $E(0_g^+)$ state. The E $\leftarrow$ B fluorescence excitation spectrum was obtained by using a monochromator, with the transmission wavelength set to 425nm, to allow detection of E $\rightarrow$ B fluorescence by a PM tube located at the exit slit. Dispersed fluorescence spectra were also collected. This basic set-up has subsequently been employed by many workers for OODR studies of ion-pair states, the most common departure being the use of high peak power, pulsed lasers rather than CW lasers.

A useful extension to this set-up was made by Brand,Hoy and

co-workers, who first applied polarization-labelling techniques in order to study the ion-pair states of ICl [25,26]. Judicious control of the polarization of the pump and probe lasers enables a clear distinction to be drawn between parallel and perpendicular electronic transitions, greatly aiding spectroscopic assignments.

The first extensive OODR study of the lowest ion-pair cluster of I_2 resulted in a rather confused picture of these states. King et al. accessed five separate states around 41000cm^{-1} , via vibrational levels of the $B(0_u^+)$ state lying close to the dissociation limit[7]. Taking into account the g ← u parity selection rule for single photon transitions and the observed rotational structure in the excitation spectra, King et al. identified four 0_g^+ states and a 1_g state; apparently contradicting Mulliken's idea of clustering. This confusion was clarified by Perrot et al., who accredited the intermediate levels as being perturbed by nearby 1_u and 1_g states and assigned the five states as $E(0_g^+)$, $\beta(1_g)$, $D'(2_g)$, $\gamma(1_u)$ and $\delta(2_u)$[27]. Several detailed OODR studies have now been carried out to determine the principal spectroscopic constants and RKR curves for a range of halogen ion-pair states (see Table 1.1) .

Recently, non-linear optical techniques for generating tunable VUV radiation have been employed to excite high vibrational levels of ion-pair states directly from the ground state. Bartels and co-workers have studied I_2 $D(0_u^+,v'=112-200)$, by utilising H_2 Raman shifting of pulsed, tunable dye laser radiation to produce coherent output radiation with wavelength range 181-202nm[28]. Lispon and Hoy have employed VUV radiation, generated by four-wave-mixing in

Xe, to study $Br_2(F0_u^+)$ [29,30]. In both experiments, the target molecules were seeded in an inert carrier gas and formed part of a supersonic expansion.

Now that accurate spectroscopic constants are available for a large number of ion-pair states (not only for I_2, but also Br_2,Cl_2,IBr,ICl etc.) a shift of emphasis in studies of these states is being observed. Rather than concentrating on mapping out potential curves and rovibronic energy levels for these states, detailed analyses of the photophysical properties of ion-pair states are now being carried out by interpreting data on line positions, intensities and fluorescence lifetimes. The aim is to build up a unifying picture of the electronic structure of ion-pair states. A particularly elegant study has been reported recently by Perrot and co-workers[31]. Using the "separated-ion" model (section 1.4), the electronic transition dipole moments for the E → B and β → A transitions in I_2 have been calculated from both fluorescence lifetime and line intensity measurements, as a function of vibrational quantum number.

1.4 Molecular Electronic Wavefunctions

There are two prevailing theories relating to the construction of molecular wavefunctions for the electronic states of I_2. In the Molecular Orbital (MO) model, the wavefunctions of these states are constructed by the linear combination of the atomic orbitals (LCAO) of the iodine atom[2]. The Separated-Atom or Separated-Ion description postulates that the molecular electronic wavefunctions

can be represented as symmetrized products of the wavefunctions for the two isolated atoms (valence states) or ions (ion-pair states) [32].

In his paper "Iodine Revisited", Mulliken collated all the available information on the valence and ion-pair states of I_2 (up to 1970) [2]. Mulliken then analysed the salient spectroscopic properties of these states using the LCAO approach. Under this scheme, the molecular orbitals of I_2 derived from the valence atomic orbitals are:

$$\sigma_g^m \ \pi_u^n \ \pi_g^{*p} \ \sigma_u^{*q}$$

where m, n, p and q indicate the orbital occupancy. This is abbreviated to mnpq throughout this thesis when describing MO electronic configurations (for I_2, m+n+p+q = 10). There are 10 ways to arrange the valence electrons in the LCAO molecular orbitals, giving rise to a total of 43 molecular states in Hund's case (c) angular momentum coupling scheme. These states can be correlated with the 23 valence states which arise from J,J coupling of the separated atoms $I(^3P_{3/2,1/2})$ and the 20 ion-pair states arising from the separated ions $I^+(^3P,^1D,^1S)$ and $I^-(^1S)$. The full adiabatic scheme for the correlation of the J,J states with MO configurations is shown in Fig 1.3. The ordering of the case (c) states is that given by Mulliken[2].

1.4.1 The Valence States

An increasing amount of experimental evidence now indicates that at short internuclear separations, the LCAO description is the most appropriate for the valence states of I_2. The separated-atom

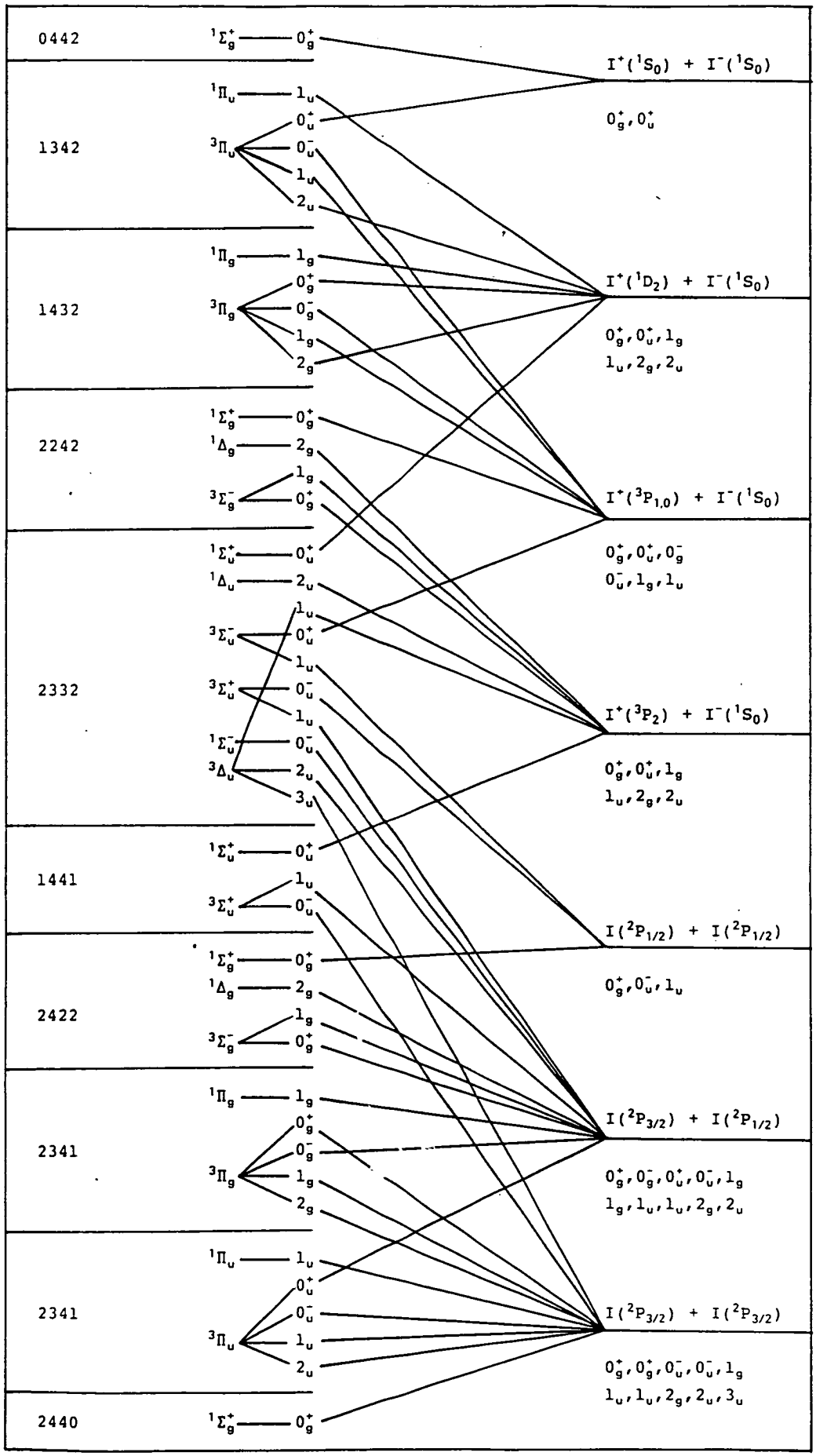

FIGURE 1.3

Adiabatic correlation diagram for the electronic states of I_2.

description has been proposed to be applicable at moderate to long separations (r>4.5Å) [33].

The main features in the visible absorption spectrum of $I_2(X0_g^+, r_e$ = 2.66Å) can be assigned using the LCAO scheme[2]. At this internuclear separation the discrete electronic states involved cannot be assigned to a unique MO occupancy, however, but rather must be considered as having contributions from two or more configurations. The $X(0_g^+)$ ground state of I_2 is a good example. The dominant MO configuration for this state is 2440, which gives rise to a single state, $^1\Sigma_g^+$, in Hund's case (a) angular momentum coupling scheme (Σ,Λ good quantum numbers). A strong absorption from the 2440 X state to the 2431 $B^3\Pi(0_g^+)$ state is observed between 15000 and 20000cm^{-1}. If both these states were described only in terms of single MO configurations, then this would formally be a forbidden $^3\Pi \leftarrow {}^1\Sigma$ transition. However, Mulliken has shown that, around $r_e(X)$, there is significant mixing of the 2431 configuration with 2440 (ca.15%), giving the ground state partial $^3\Pi(0_g^+)$ character[2]. As a result of this configuration mixing, the B ← X transition becomes strongly allowed. The current convention therefore is to adopt the case (c) (Ω $^{+/-}_{g/u}$) label as a subscript to the case (a) description arising from the dominant MO configuration. For clarity of presentation in this thesis, the valence states of I_2 are generally only given the appropriate case (c) labels.

Following a determination of the hyperfine parameters for the X and B states from a high resolution study of the B ← X fluorescence excitation spectrum, Bacis et al. have concluded that for r>4.5Å, the

electronic wavefunctions for the valence states are best approximated using the separated-atom description[33].

1.4.2 The Ion-Pair States

For separations close to r_e of the X state (ca. 2.66Å) , the principal features of the UV absorption and fluorescence excitation spectra can be explained using the LCAO approach[2,17,18]. However, these transitions only involve the inner turning points of highly vibrationally excited ion-pair states. The ion-pair states of I_2 have r_e values of ca. 3.6Å and there is now a considerable body of experimental evidence which suggests that the separated-ion description is the most appropriate at these internuclear distances.

The separated-ion theory has been used to interpret results from a range of experiments on the ion-pair states of Br_2,ICl and IBr, as well as I_2. Brand et al. have analysed rotational perturbations between the lowest vibrational levels of the $E(0^+)$, $\beta(1)$ and $D'(2)$ states of ICl. The interaction matrix elements W_{mn} (where m and n denote the values of Ω for the interacting states) for these perturbations have been estimated from OODR measurements and compared with those values calculated using the "pure-precession" model of Van Vleck. This model assumes that the ion-pair state wavefunctions can be derived from the separated ions and that only states having common $\mathbf{J}_a$ may interact, where for separated ions $A^+(J_A,M_J)$ and $B^-(J_B,M_J)$:

$$\mathbf{J}_a = J_A + J_B$$

eg. for the first ion-pair cluster of ICl, $\mathbf{J}_a=2$. The magnitude of W_{mn}

depends upon J_a. The close agreement between the experimentally observed and calculated values of W_{mn} indicates that around r_e, the separated-ion description gives a good approximation to the molecular electronic wavefunctions of ICl(E,β and D').

The analysis has been successfully applied to similiar perturbations in IBr, Br_2 and I_2 [35-37]. Indeed, the separated-ion picture works so well that Ishiwata et al. have used the pure-precession model to predict the energy separation between the 1_g and 0_g^- (J_a=1) states of Br_2, following an analysis of Ω-splitting in the 1_g state[38].

Bouvier et al. have carried out a high resolution spectroscopic determination of the hyperfine structure of the $E(0_g^+)$ and $f(0_g^+)$ states of I_2. The hyperfine parameters for these states have also been calculated using the pure-precession model. The close agreement between the calculated values and those determined experimentally is further confirmation of the validity of the separated-ion description of I_2 ion-pair states[39].

1.5 Intensities of ion-pair → valence state transitions

In the light of the increasing amount of data on electronic transitions between ion-pair and valence states ,it is now of some interest to develop a clear picture of the factors governing the intensities of these transitions.

Absorption from the ground states of the halogen molecules directly to the inner turning points of highly vibrationally excited

ion-pair states are best analysed by considering the MO configurations for the states involved (see 1.4). This has been dealt with by Mulliken and the following results are a brief summary of his findings[2]:

(1) Transitions between states which involve single electron changes in the MO occupancy are expected to be strongly allowed, assuming the appropriate angular momentum selection rules are obeyed. Transitions requiring two electron shifts are expected to be weak.

(2) A transition may gain intensity as result of spin-orbit mixing with another state having the same total electronic angular momentum and symmetry.

Most of the work presented in this thesis involves transitions to or from ion-pair states at internuclear distances where the separated-ion description is the most valid. In this case, it has been generally observed that $\Delta\Omega=0$ transitions are more intense than those with $\Delta\Omega=1$. This is referred to as the "$\Delta\Omega=0$ propensity rule" throughout this thesis. This empirical rule can be explained in a straightforward, if somewhat heuristic, fashion[40]. Assuming the separated-ion description holds, ion-pair → valence transitions will involve transfer from a filled p orbital on $I^-(^1S_0)$ to a vacant or half-vacant p orbital on I^+. For $\Delta\Omega=0$ transitions, the electron transfer will occur such that the transition dipole moment vector lies parallel to the internuclear axis, z, (eg.$p_z \rightarrow p_z$, $p_y \rightarrow p_y$), but will be perpendicular when $\Delta\Omega=1$ (eg. $p_z \rightarrow p_y$, $p_y \rightarrow p_x$). The relative strength of a given transition will depend upon the degree of overlap between

the orbitals involved. Those transitions involving transfer in and out of p_z orbitals will carry the greatest oscillator strength, with $p_z \rightarrow p_z$ ($\Delta\Omega=0$) transfer giving the best overlap. As a result, parallel ($\Delta\Omega=0$) transitions will generally be more intense than perpendicular transitions ($\Delta\Omega=1$).

1.6 Simulation of Dispersed Fluorescence

The rate of spontaneous emission of photons as a result of a transition between two rovibronic states is given by:

$$A(\nu) = (64\pi^4\nu^3/3h)\, S_J \left[\int \psi_v^{*'}\, \mu_{21}(r)\, \psi_v''\, d\tau\right]^2 \quad (1.3)$$

where,
$A(\nu)$ = Einstein coefficient for spontaneous emission
ν = transition frequency
S_J = Rotational Honl–London intensity factor
(incorporating degeneracy of states)

$\int \psi_v^{*'}\, \mu_{21}(r)\, \psi_v''\, d\tau$ is the integrated overlap between the vibronic wavefunctions of the two states.

$\mu_{21}(r)$ is the electronic transition dipole moment function:

$$\mu_{21}(r) = \int \psi_e^{*'}\, \mu\, \psi_e''\, d\tau \quad (1.4)$$

and describes the overlap of the two electronic wavefunctions ψ_e' and ψ_e''.

The computer programme "SPECFUSE" employed to evaluate (1.3), by solving the radial nuclear Schrödinger equation, was written by Lawley and Wheeler [41], and altered by Austin to allow more efficient calculation of continuum wavefunctions using the

Numerov-Cooley method [42]. It is not intended to give an account of the mathematics of the simulation procedure in this thesis, as this has been dealt with in some detail by the above authors.

In order to carry out the spectral simulations, the upper and lower state potential energy curves, in the form of evenly spaced grid points, must be given as input, along with an approximation to the electronic transition dipole moment function, $\mu_{21}(r)$. If one of the potential curves is not known then a reasonable guess is initially entered and by iteratively comparing the experimental and simulated spectra, whilst adjusting the unknown state, the form of the potential energy curve can be determined. Spectral simulations are still of value when both potentials have been previously ascertained, as the electronic transition dipole moment function can be determined from the experimental intensity envelope. $\mu_{21}(r)$ contains information on the electronic wavefunctions for both states and hence is of some interest in the light of current speculation on the nature of halogen diatomic ion-pair and valence state electronic wavefunctions (see section 1.4).

Following evaluation of $A(\nu)$, the resulting spectrum is then convoluted to allow for detection following transmission through a scanning monochromator with a fixed wavelength slit. The photomultiplier tubes employed operated on the photo-electric effect, giving a response which is proportional to the energy of the incident photon. The above two factors combine to introduce a further ν^3 term to the experimental spectrum. The observed experimental spectrum is thus given by:

$$S_{exp}(\nu) = F(\nu)\ \nu^3\ A(\nu) \qquad (1.5)$$

and is in units of energy per unit wavelength interval per second. $F(\nu)$ combines the following three factors:

(i)The variation of the angular dispersion of the monochromator grating with ν. This is purely a geometrical factor, depending only upon the configuration of the monochromator.

(ii)The variation of the reflectivity of the grating with ν. This will be different for individual gratings.

(iii)The variation of the photomultiplier response with ν.

$F(\nu)$ can be obtained from comparison of the observed intensities from a calibrated radiation source with those absolute intensities provided by the manufacturer. $F(\nu)$ had been previously determined for the monochromator/PM tube combination employed in the work presented here (Jobin-Yvon HRS 2/Hammamatsu R928).

Ideally, both experimental and simulated spectra should be in units of $\nu^2.A(\nu)$, i.e. neither should include dependence upon $F(\nu)$ or the type of photomultiplier employed. However, as many of the spectra recorded for this thesis were not digitised,it was not possible to directly deconvolute for $\nu.F(\nu)$. To allow direct comparision of the simulated and experimental spectra, $F(\nu)$ has been applied to the simulations and thus, spectra throughout this thesis are in units of energy per unit wavelength interval per second.

$$S_{sim}(\nu) = F(\nu)\ \nu^3\ A(\nu) \qquad (1.6)$$

1.7 The OODR technique

Diatomic halogen ion-pair states have equilibrium internuclear separations which are characteristically greater than that of their ground states. In accordance with the Franck-Condon principle, these differences in r_e mean that only the higher vibrational levels (v'>100) of the ion-pair states can be accessed in single photon excitation from the ground state. However, an alternative excitation route can be employed to enable excitation of the lowest lying vibrational levels of halogen ion-pair states. The Optical-Optical Double Resonance technique involves two sequential excitation steps.In the first, the molecule is excited from its ground state to a higher valence state. This state then establishes its own Franck-Condon region and facilitates excitation to a wider range of ion-pair rovibronic levels (see Figure 1.4) . In the case of I_2, the $B(0_u^+)$ state is generally employed, having r_e=3.0Å which is intermediate between that of the ground state, 2.66Å, and the ion-pair states (typically 3.6Å).

OODR excitation also offers other advantages over single photon excitation. The parity selection rule for homonuclear diatomic molecules stipulates that only g ↔ u electronic transitions are allowed. Thus, from the $X(0_g^+)$ ground state of I_2, transitions to half of the ion-pair states are forbidden. OODR involves two sequential, resonant steps, the second of which may be a multiphoton step. For a second step involving n photons, this leads to overall symmetry selection rules of:

g → u → g (n odd)
g → u → u (n even)

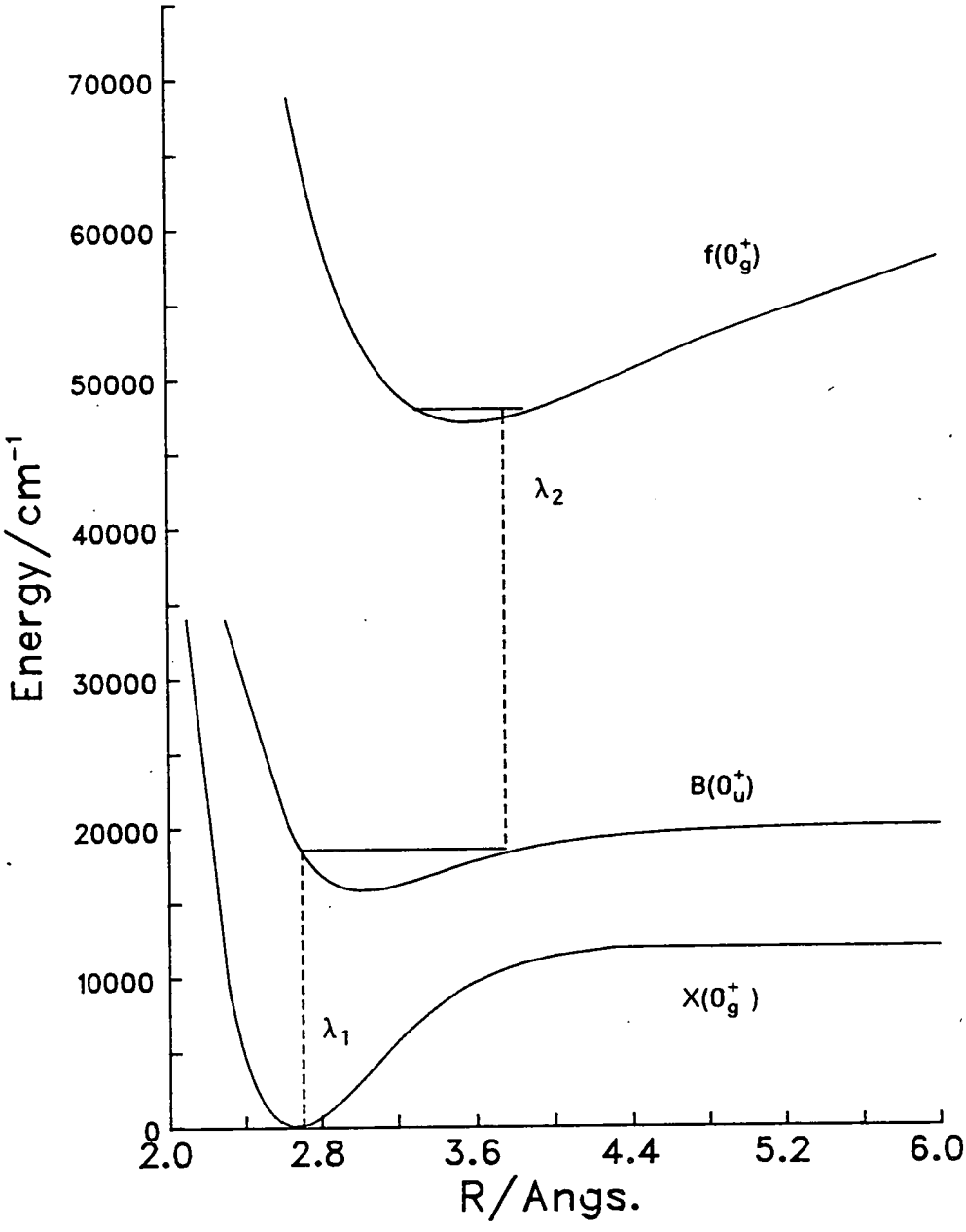

FIGURE 1.4

OODR excitation of $I_2(f0_g^+)$.

A high degree of rotational selectivity in the final state can also be achieved by use of OODR. If a single rotational transition is pumped in the first step, then only those transitions permitted by the appropriate rotational selection rules will occur in the second step. For a $\Delta\Omega=0$ ($\Delta J=\pm1$) transition, only single P and R rotational transitions will accompany each vibronic transition, leading to a great simplification of the fluorescence excitation spectrum (see Figure 3.2) and allowing excitation of single rovibronic ion-pair levels.

One further advantage of OODR is that it is possible to efficiently excite states with energies greater than 50000cm^{-1}. Generation of single laser pulses with this energy generally requires the use of sophisticated non-linear optical techniques such as Raman-shifting or four-wave-mixing, with the result that the VUV laser beam has low intensity.The absorption cross-sections for non-resonant multi-photon excitation processes are generally orders of magnitude smaller than the corresponding OODR cross-sections.

The combination of the above factors has resulted in OODR becoming the most commonly employed technique in the study of halogen diatomic ion-pair states.

1.8 References

1. L Mathieson and A.L.G. Rees, J. Chem. Phys. **25**, 753 (1956)
2. R. Mulliken, J. Chem. Phys. **55**, 288 (1971)
3. J. Tellinghuisen, J. Mol. Spec. **94**, 231 (1982)
4. J.P. Perrot, M. Broyer, J. Chevaleyre and B. Femelat, J. Mol. Spec. **98**, 161 (1982)

5. T. Ishiwata and I Tanaka, Laser Chem. **7**, 79 (1987)
6. J.C.D. Brand and A.R. Hoy, J. Mol. Spec. **95**, 350 (1982)
7. G.W. King, I.M. Littlewood and J.R. Robins, Chem. Phys. **56**, 145 (1981)
8. J.P. Perrot, A.J. Bouvier, A. Bouvier, B Femelat and J. Chevaleyre, J. Mol. Spec. **114**, 60 (1985)
9. K.S. Viswanathan and J. Tellinghuisen, J. Mol. Spec. **101**, 285 (1983)
10. A.R. Hoy and J.C.D. Brand, Chem. Phys. **109**, 109 (1986)
11. T. Ishiwata, T. Kusayanagi, T.Hara and I. Tanaka, J. Mol. Spec. **119**, 337 (1986)
12. K.S. Viswanathan, A. Sur, and J. Tellinghuisen, J. Mol. Spec. **86**, 393 (1981)
13. T. Ishiwata, A. Tokunaga, T. Shinzawa and I. Tanaka, J. Mol. Spec. **117**, 89 (1986)
14. A.R. Hoy and A.W. Taylor, J. Mol. Spec. **126**, 484 (1987)
15. J.C.D. Brand and A.R. Hoy, J. Mol. Spec. **97**, 379 (1983) and references therein.
16. J.C. McLennan, Proc. Roy. Soc. **A88**, 289 (1913)
17. A. Hiraya, K. Shobatake, R.J. Donovan and A. Hopkirk, J. Chem. Phys. **88**, 52 (1988)
18. R.J. Donovan, M.A. MacDonald, K.P. Lawley, A.J. Yencha and A. Hopkirk, Chem. Phys. Lett. **138**, 571 (1987)
19. K. Wieland, J.B. Tellinghuisen and A. Nobs, J. Mol. Spec. **41**, 69 (1972)
20. J. Tellinghuisen, Chem. Phys. Lett. **29**, 359 (1974)
21. J. Tellinghuisen, M.R. McKeever and A. Sur, J. Mol. Spec. **82**, 225 (1980)

22. J. Tellinghuisen, Chem. Phys. Lett. **99**, 373 (1983)
23. J. Tellinghuisen, Can. J. Phys. **62**, 1933 (1984)
24. D.L. Rosseau and P.F. Williams, Phys. Rev. Lett **33**, 1368 (1974)
25. J.C.D. Brand, A.K.Kalukar and A.B. Yamashita, Opt. Comm. **39**, 235 (1981)
26. J.C.D. Brand, K.J. Cross and N.P. Ernsting, Chem. Phys. **59**, 405 (1981)
27. J. Chevaleyre, J.P. Perrot, J.M. Chastan, S. Valignat and M. Broyer, Chem. Phys. **67**, 59 (1982)
28. M. Bartels, R.J. Donovan, A.J. Holmes, P.R.R. Langridge-Smith, M.A. MacDonald and T. Ridley, (to be submitted for publication 1989)
29. R.H. Lipson, A.R. Hoy and M.J. Flood, Chem. Phys. Lett. **149**, 155 (1988)
30. R.H. Lipson and A.R. Hoy, (Submitted to J. Mol. Spec. 1988)
31. J.P. Perrot, B. Femelat, J. L. Subtil, M. Broyer and J. Chevaleyre, Mol. Phys. **61**, 85 (1987)
32. K. Lawley, Chem. Phys. **127**, 363 (1988)
33. R. Bacis, M. Broyer, S. Churassy, J. Vergès and J. Vigue, J. Chem Phys. **73**, 2641 (1980)
34. D. Bussieres and A.R. Hoy, Can. J. Phys. **62**, 1941 (1984)
35. J.C.D. Brand, A.R. Hoy and A.C. Risbud, J. Mol. Spec. **113**, 47 (1985)
36. T. Ishiwata, T. Hara, K. Obi and I. Tanaka, J. Chem. Phys. **87**, 2513 (1987)
37. J.P. Perrot, B. Femelat, M. Broyer and J. Chevaleyre, Mol. Phys. **61**, 97 (1987)
38. T. Ishiwata, K. Obi and I. Tanaka, J. Mol. Spec. **127**, 353 (1988)

39. A.J. Bouvier, R. Bacis, A. Bouvier, M. Broyer, S. Churassy and J.P. Perrot, Opt. Comm. **51**, 403 (1984)

40. K.P. Lawley, Private Communication

41. K.P. Lawley and R. Wheeler, J. Chem. Soc. Farad. Trans. II **77**, 1133 (1981)

42. D.I. Austin, Ph.D. Thesis (University of Edinburgh, 1987)

Chapter 2
EXPERIMENTAL

2.1 Summary

This chapter describes the experimental techniques employed in obtaining the results presented in Chapters 3, 4 and 5. Additional experimental details are included, where appropriate, in these chapters. Two colour optical-optical double resonance (see Chapter 1) was used to excite the ion-pair states of I_2, employing the $B(0_u^+)$ state as an intermediate. The experimental configuration is shown in Figure 2.1 .The pulsed output from a high power excimer laser (Lambda Physik EMG 201 MSC), operating on the 308nm XeCl (B → X) lasing transition was used to simultaneously pump two dye lasers. The first dye laser (Lambda Physik FL3002E) was used to selectively excite single rovibronic levels of the $B(0_u^+)$ state of I_2. The second laser was employed to pump molecules excited by the first laser from the B state to a range of ion pair states.

Samples of I_2 and I_2/rare gas mixtures were contained in a simple, cylindrical, glass cell fitted with spectrosil quartz windows, attached with fluorocarbon wax. The cell was arranged so that the beams from the two lasers travelled collinearly through the cell, but in opposite directions. The pulsed output from the two dye lasers arrived at the cell in close coincidence (delay = 3ns), giving close to maximum efficiency for OODR excitation[1]. Fluorescence was collected at right angles and imaged onto the entrance slit of a monochromator (Jobin-Yvon HRS2; f/7, 0.6m) Dispersed fluorescence at the exit slit was monitored by a photomultiplier (Hammamatsu R928 or R166, solar blind), the d.c. output from which was fed into a Stanford Research Systems SR250 gated intergrator, interfaced to an IBM PC-XT microcomputer. Digitised data were

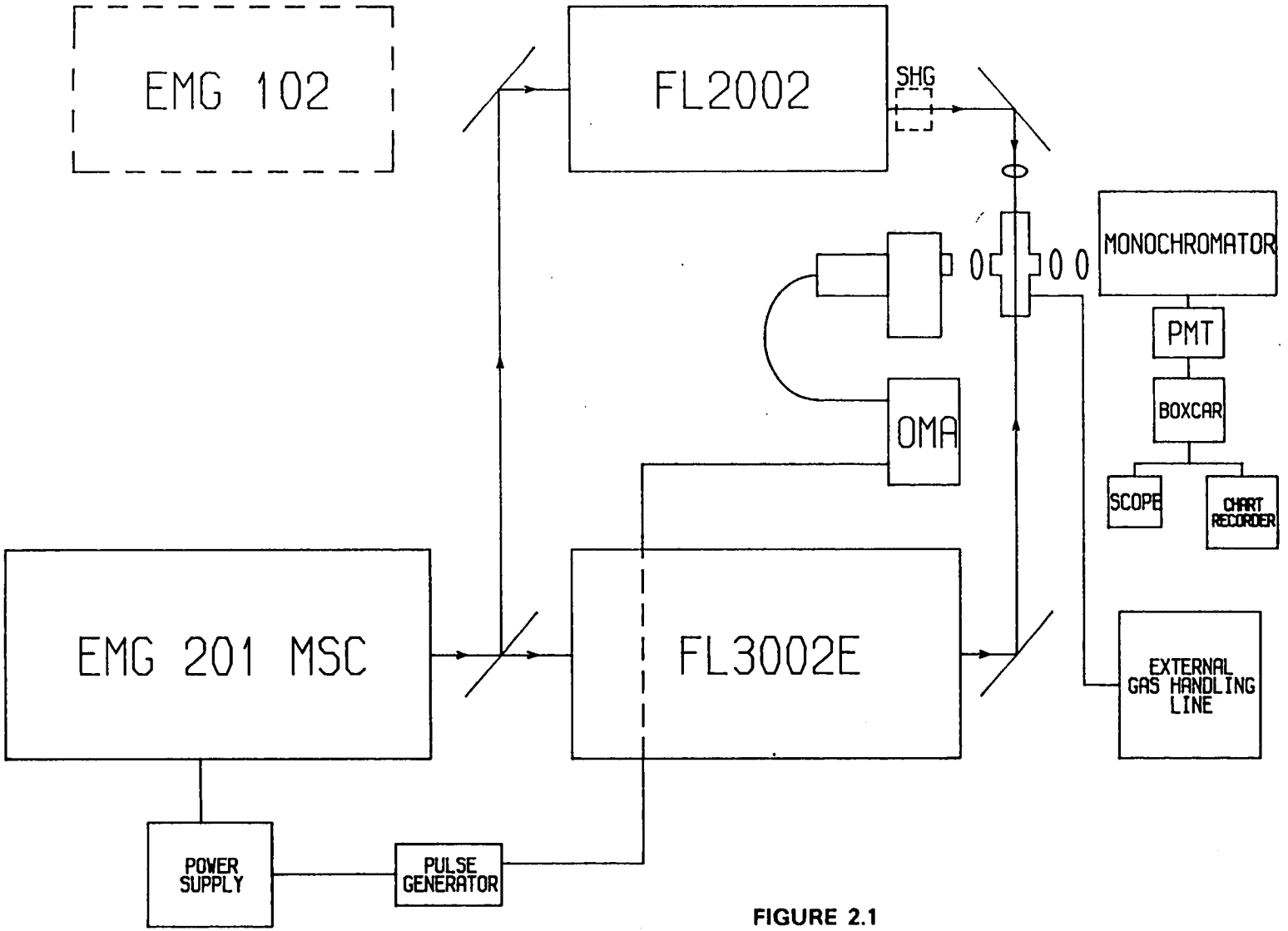

FIGURE 2.1

Schematic diagram of the experimental apparatus.

stored to disk and the analog output from the boxcar was relayed directly to a chart recorder (Kipp and Zonen BD8). An alternative light collection system comprising of a Jarrell-Ash polychromator and EG & G Optical Multichannel Analyser (OMA III) was also used to directly record wavelength resolved emission spectra.

2.2 Excimer-pumped dye laser system

The consistent performance of the high power, continuously tunable, laser system was crucial in allowing the work presented in this thesis to be carried out. The excimer laser typically delivered pulses of 15 ns duration, with an energy of ca. 400mJ/pulse at a repetition rate of 3-5 Hz. A neon-based gas mixture, as specified by the manufacturer[2], was used to fill the laser cavity. The output UV radiation from the excimer laser, a 1cm x 2cm rectangle, was then used to pump two dye lasers.

The FL3002E dye laser was pumped using UV radiation transmitted through a 50% beamsplitter. This dye laser was typically operated close to the maximum of the gain profile of Rhodamine 6G laser dye. All dyes used were directly as supplied by Lambda Physik. The output pulses from the FL3002E were approximately 10 ns long, with an energy of 15-20 mJ, at a repetition rate of 3-5 Hz. A single rovibronic level in the intermediate state was excited, whenever possible. In order to facilitate this, an air-spaced Fabry-Perot type etalon was used to reduce the output laser bandwidth from $0.2cm^{-1}$ to $0.04cm^{-1}$. In order to wavelength scan the output from this laser whilst obtaining radiation of a narrow bandwidth, it was neccessary

to simultaneously change the grating incidence angle and the tilt of the intra-cavity etalon. This was done using a pre-programmed computer control system which forms an integral part of the FL3002E dye laser.

Radiation reflected at the beamsplitter was used to pump the FL2002 dye laser, following reflection at a coated mirror at ca. 1.5m displacement from the beamsplitter. This led to significant divergence of the UV beam, with the result that the output fundamental from the FL2002 dye laser had an energy of ca. 5-10mJ/pulse, somewhat lower than that of the FL3002E.

The technique of second harmonic generation (SHG) was used to produce a coherent beam of frequency-doubled radiation from the second dye laser. The wavelength range of commercially available laser dyes only extends to ca. 338nm (for 308nm exciting radiation) and non-linear optical techniques must be employed to obtain continuously tunable radiation to the blue of this region. SHG employs a non-isotropic crystal as the non-linear medium. The crystals used were KDP (potassium dihydrogen phosphate) and KPB (potassium pentaborate), as supplied by Lambda Physik (KDP:FL30,31; KPB: FL32) Efficient SHG requires the input radiation to be polarized. The output fundamental from the dye laser is vertically polarized in the ratio 5:1[3]. This was found to be sufficient for effective SHG, without the aid of additional beam polarizers. A UG5 filter was used with the KDP crystals to separate the frequency-doubled radiation from the transmitted fundamental beam. When utilising the KPB crystal, the fundamental and second harmonic were separated using

a Pellin-Broca prism (in tandem with a compensating prism to reduce beam walk induced by angle tuning). Use of a SHG crystal reduced the output energy of the laser by ca. 90% and 99% for KDP and KPB respectively. In order to scan the grating of the FL2002 whilst frequency-doubling, it was neccessary to synchronously step the grating and crystal positions by computer (see 2.6) .

2.3 Monochromator

A Jobin-Yvon HRS2 monochromator (0.6m, f/7), fitted with a holographic grating (1500 grooves/mm), was employed to disperse fluorescence collected from the I_2 cell. Two quartz lenses were placed between the cell and the monochromator entrance slit. The first (f=4cm) was placed 5cm from the excitation region, in order to increase the collection efficiency of the system. A second lens (f=15cm), located a further 20cm away, was employed to condense the light onto the entrance slit to the monochromator such that it filled the first monochromator mirror. The relative transmission efficiency of the monochromator , in combination with a Hammamatsu R928 photomultiplier, as a function of wavelength had been previously determined. Fig 2.2 shows the combined monochromator/photomultiplier response curve.

2.4 Boxcar Gated Integrator

Fluorescence was detected at the exit slit of the monochromator using a side-on photomultiplier tube (Hammamatsu; R928 or R166). A stabilised voltage power supply (Brandenburg 4728, 0-2.0kV) was used to provide a photomultiplier anode to cathode voltage drop of

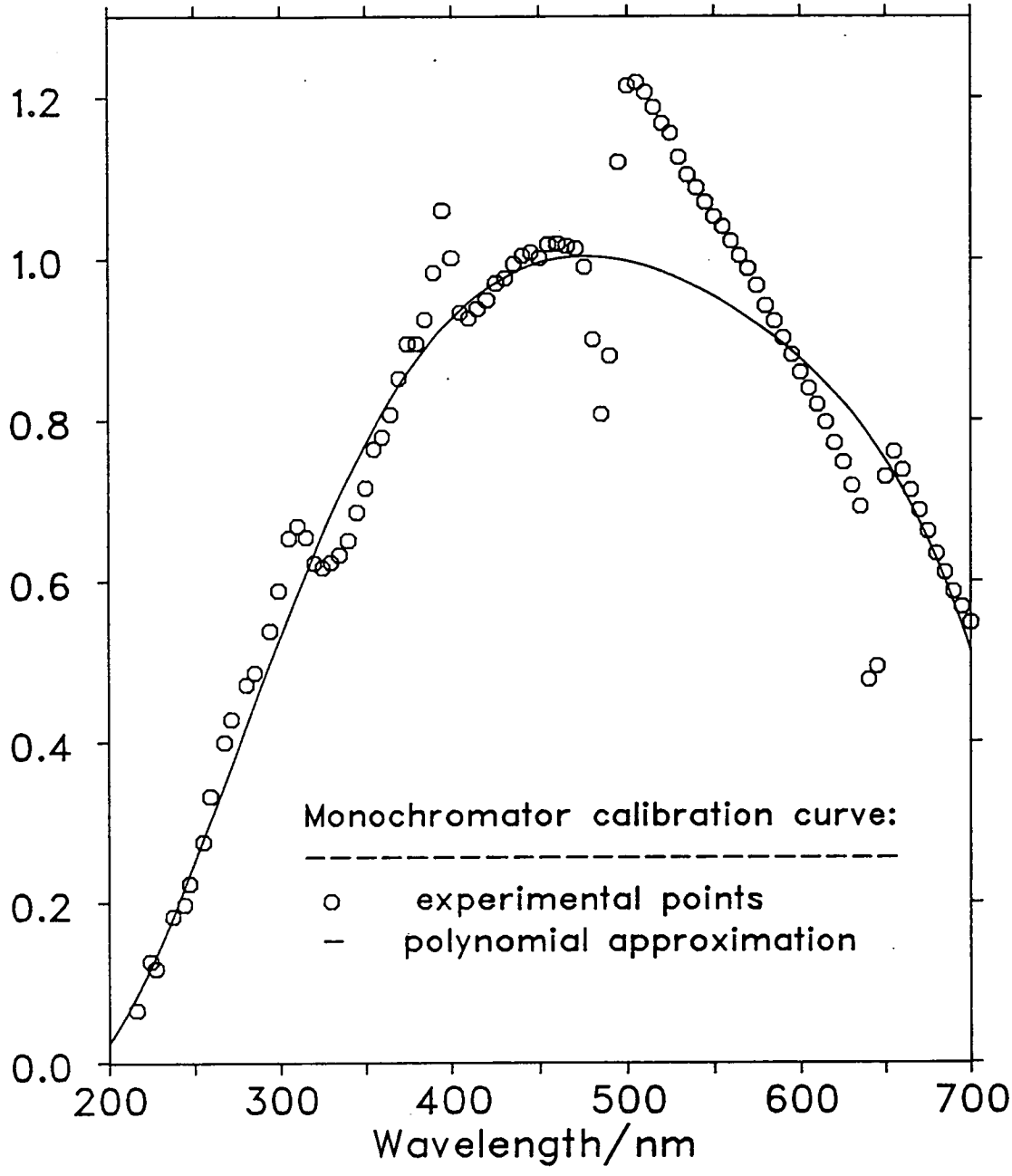
1.2
1.0
0.8
0.6
0.4
0.2
0.0
200
300
400
500
600
700
Wavelength/nm
Monochromator calibration curve:
experimental points
polynomial approximation

FIGURE 2.2

1.1kV . The signal from the photomultiplier was then relayed to a boxcar gated integrator via a 1MΩ resistor. The SR250 Gated Integrator and Boxcar Averager (Stanford Research Systems) consists of a gate generator, a fast gated integrator and an exponential averaging facility. At an experimental repetition rate of 5Hz, fluorescence is only emitted for approximately a few hundred nanoseconds in a one second period (typical halogen ion-pair state radiative lifetimes are ca. 30ns). It is thus neccessary to gate the sampling of the photomultiplier signal in order to reduce background noise to an acceptable level.

The SR250 was triggered by the excimer laser and sampled the photomultiplier signal after a fixed time delay. The gate delay and width were set by displaying the photomultiplier output signal and boxcar gate simultaneously on a four channel oscilliscope (Tektronix 2445; 150 MHz) and adjusting the SR250 to ensure optimum sampling. The incoming signal was integrated over the opening time of the gate by the fast gated integrator. The output from the integrator was then normalized by the gate width. This gave a voltage which was proportional to the average of the input fluorescence signal during the sampling time. Moving exponential averaging of this normalised signal was then carried out over a pre-selected number of laser shots in order to further discriminate the fluorescence signal from the background noise. The number of shots averaged in this way was determined by the scan rates of the laser and monochromator. Care was taken to ensure that loss of resolution due to excess smoothing did not occur. The analog output from the boxcar was sent to a chart recorder and to a computer

interface (Stanford Research Systems SR245) to be digitised and this information relayed to an IBM PC-XT microcomputer.

2.5 Optical Multichannel Analyser

Fluorescence emission from the sample cell was also dispersed using a 0.25m Jarrell-Ash polychromator and imaged onto a photosensitive diode array (reticon). This consisted of 1024 diodes (25μm by 25mm in size) which formed part of an optical multichannel analyser system (EG & G PARC; OMAIII), comprising the detector head, a detector controller and a system processor (EG & G PARC; 1420, 1463, 1460). The function of the detector controller was to digitise the analog signal from the detector head and relay it to the Central Processing Unit (CPU). The CPU allowed data handling routines to be run and also provided an asynchronous communications port (RS232C) to allow attachment of devices such as plotters. The OMA system also contained a Direct Memory Access unit (DMA) which could be programmed to perform sophisticated data acquisition routines. The polychromator had three interchangeable gratings (600, 300 and 150 grooves/mm). Use of the polychromator/OMA combination gave spectra of lower resolution than those obtained by scanning the 0.6m monochromator. However, the entire emission spectrum was accumulated very rapidly using the OMA system, generally in 100 - 1000 laser shots. This was particularly useful in kinetic studies where many spectra at different sample pressures had to be collected and also eliminated problems associated with the drifting of laser frequencies with time.

2.6 Computer controlled scanning and data collection

Data collection and storage was controlled by a software package (Stanford Research Systems; SR265, version 2.21) implemented on an IBM PC-XT microcomputer. Additional Fortran routines were written and incorporated into the programme to allow synchronous scanning of the FL2002 dye laser (and the frequency-doubling crystal if required) whilst collecting fluorescence excitation data. Remote scanning of the grating and crystals was achieved by sending commands from the computer to a control unit (Lambda Physik FL512A) which in turn activated the laser stepper motors. The number of data collection bins was pre-selected for a desired wavelength range and the wavelength step between samples was calculated. The grating motor gave steps of length:

$$\Delta\lambda = 0.0084\text{nm/grating order}$$

The data collection interface was triggered from the boxcar, which was initially triggered by the firing of the excimer laser. The scan rate was therefore controlled by varying the experimental repetition rate. The optimum crystal position for second harmonic generation, at a given wavelength was calculated as follows:

$$\alpha(\lambda) = \Sigma\ a_m.\lambda^m$$

where the coefficents, a_m, were obtained from a calibration programme, separately run on a Sinclair Spectrum microcomputer. The number of steps, n, of the crystal motor required to tune the crystal from wavelength λ_1 to λ_2 is given by the integer part of the expression:

$$n = 200.(\alpha(\lambda_1) - \alpha(\lambda_2))$$

For a fixed wavelength step, n is not constant and hence was calculated at each part of the scan. Once triggered, the interface digitised the incoming analog signal from the boxcar and relayed its value to the microcomputer. Further trigger signals were then ignored by the interface until the laser and crystal had been stepped to the next position. At the end of each scan, the experimental spectrum was scaled and stored to disk in binary form for subsequent conversion to character files and downloading to the local mainframe computer, EMAS (Edinburgh Multi-Access System). This was generally carried out with the aid of the KERMIT software package. The stepping of the Jobin-Yvon HRS2 monochromator could not be externally controlled. Dispersed fluorescence data were collected by manually activating the monochromator stepping motor and the data collection programme simultaneously.

2.7 References

1. M.D. Danyluk and G.W. King, Chem. Phys. **22**, 59 (1977)
2. "Lambda Physik FL3001/2 Instruction Manual" (Göttingen, March, 1986)
3. "Lambda Physik EMG 201-204 MSC Instruction Manual" (Göttingen, April,1985)

Chapter 3
AN INVESTIGATION INTO THE SPECTROSCOPY OF $I_2(f0_g^+)$

3.1 Introduction

An extensive exploration of the fluorescence spectroscopy of the $f(0_g^+)$ ion-pair state of I_2 is presented in this chapter , along with computer simulations of the experimental spectra. The aims of studying the $f(0_g^+)$ state were as follows:

(i) Achieve OODR excitation of the $f(0_g^+)$ state over a wide range of rotational and vibrational states.

(ii) Obtain dispersed fluorescence following excitation of single rotational levels of $f(0_g^+)$.

(iii) Carry out an analysis of this fluorescence using simulation techniques in order to characterise the transition dipole moment function, $\mu_{21}(r)$, for fluorescence from the $f(0_g^+)$ ion-pair state to the $B(0_u^+)$ valence state.

The use of the f state of I_2 to study the dynamics of XeI^* formation, using dispersed fluorescence, is described in Chapter 5. In order to carry out this study, a full understanding of the fluorescence spectroscopy of the f state, as described below, was essential.

3.2 Fluorescence Excitation Spectra

A portion of the fluorescence excitation spectrum of the $B(0_u^+)$ state of I_2, displaying the $B(v'=15) \leftarrow X(v''=1)$ bandhead, is shown in Figure 3.1. This spectrum was collected by tuning the FL3002E dye laser from 581nm to 582nm, whilst detecting $B \rightarrow X$ fluorescence emission from the cell at 622.5nm . Accurate wavelength calibration

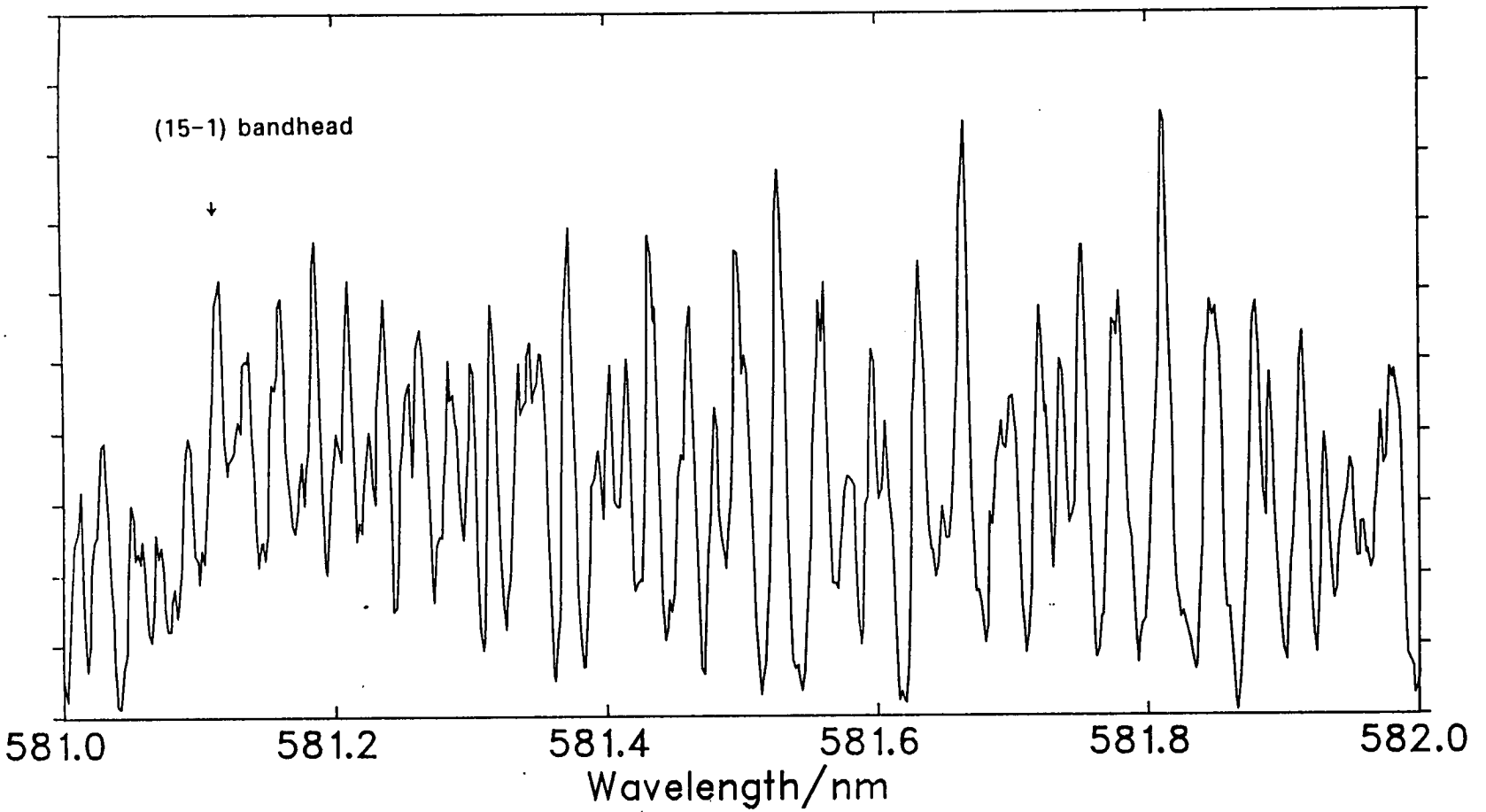

FIGURE 3.1

I_2 B ← X fluorescence excitation spectrum

(collection wavelength = 622.5nm).

of this spectrum was achieved by comparison with the published atlas of the visible absorption spectrum of I_2[1]. In order to aid the initial assignment of features in this spectrum, the dye laser was operated with an intracavity etalon, giving a laser band width of $0.04cm^{-1}$. This greatly aided the matching of individual rotational features of the absorption spectrum (resolution $0.015cm^{-1}$) and the fluorescence excitation spectrum. Individual rotational bands were assigned using the published molecular constants for the $X(0_g^+)$ and $B(0_u^+)$ states (the latter being derived from the absorption data) [2]. The B ← X spectrum is extremely congested as a result of the close rotational spacing in I_2 and the large number of vibrational and rotational states of $I_2(X0_g^+)$ populated at room temperature. At 298K, ca. 36% of the I_2 molecules are in vibrationally excited states with 29% being in v"=1. Thus, the fluorescence excitation spectrum is complicated by significant contributions from hot bands.

The complex nature of the B ← X fluorescence excitation spectrum can be contrasted with the simplicity of the optical–optical double resonance fluorescence excitation spectrum of the $f(0_g^+)$ state, as excited from the $B(0_u^+)$ state, shown in Fig 3.2 . This spectrum was obtained by pumping a single rovibronic level of the B state and tuning the frequency doubled output from the FL2002 dye laser from 292 to 295nm, whilst collecting fluorescence at 340nm. The spectrum consists of a regular progression of doublets. This structure can be explained in terms of the selection rules for electronic transitions of I_2, using Hund's case(c) angular momentum coupling scheme. The transition $f(0_g^+)$ ← $B(0_u^+)$ has $\Delta\Omega=0$,where Ω = total electronic spin and orbital angular momentum. The quantum

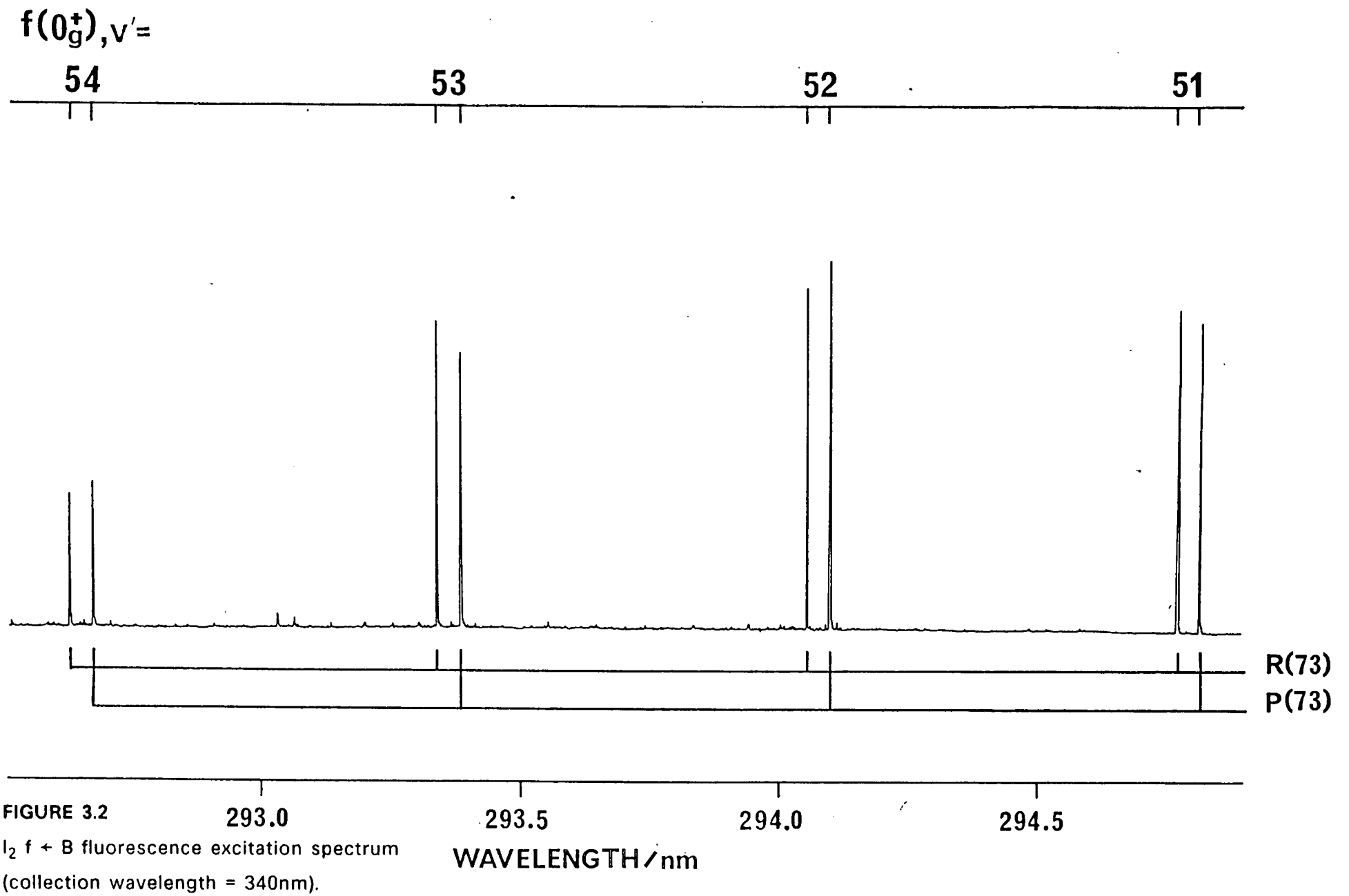

FIGURE 3.2

I_2 f ← B fluorescence excitation spectrum (collection wavelength = 340nm).

state selection rules governing changes in vibrational and rotational energy for such a transition are [3]:

$$\Delta v = n \quad , \Delta J = \pm 1$$

Thus, each pair of lines in the fluorescence excitation spectrum arises from P and R branch rotational transitions from a single rovbronic level in the $B(0_u^+)$ state, to a discrete vibrational level in the $f(0_g^+)$ state. This spectrum clearly indicates that only a single, rovibronic level in the B state is being excited by the first laser and is a clear demonstration of the power of the OODR technique in simplifying spectra, as described in Chapter 1.

Varying Franck-Condon factors give rise to the observed change in fluorescence intensity as the laser is scanned through the vibrational manifold of I_2. The overall excitation process has been assigned as

$$f(0_g^+) \overset{2}{\leftarrow} B(0_u^+) \overset{1}{\leftarrow} X(0_g^+)$$

1.(19-2)R(72)

2.(n-19) P,R(73) :n= 51 to 54

Individual bands were assigned by calculating transition energies using the molecular constants of Perrot et al. for the $f(0_g^+)$ state[4]. The wavelength at which fluorescence was collected (340nm) corresponds to the red extremum of the f → B fluorescence system (see Figs 3.6-3.9) .

3.3 Dispersed Fluorescence

Wavelength dispersed fluorescence emission spectra have been recorded for a wide range of vibrational levels of $I_2(f0_g^+)$, up to v'=88. For low-lying vibrational levels, up to v'=11, discrete fluorescence systems are observed at 340, 290, 280 and 265 nm. The bands at 340, 290 and 280 nm originate from the $f(0_g^+)$ state, whilst the 265nm fluorescence arises from collisional population of the $F(0_u^+)$ state[5]. Fig 3.3 displays vibrationally resolved spectra around 340nm, obtained following excitation of $I_2(f0_g^+$, v'= 0, 1, 3 and 5) . This bound-bound fluorescence is readily assigned as

$$f(0_g^+, v'= n) \rightarrow B(0_u^+, v''= m)$$

Fig 3.4 shows dispersed fluorescence from $I_2(f0_g^+$, v'=0) over the range 250 to 300nm. The bound-bound system at 280nm can be assigned to:

$$f(0_g^+, v'= 0) \rightarrow A(^3\Pi_{1u}, v''= m)$$

The oscillatory continuum emission at 290nm has been assigned to the transition[6]:

$$f(0_g^+, v'= 0) \rightarrow {}^1\Pi_{1u} \text{ (repulsive)}$$

The lower repulsive state correlates with ground state iodine atoms ($^2P_{3/2}$ + $^2P_{3/2}$) and has been partially characterised by Tellinghuisen[7].

The relative intensities of these three systems are consistent with the general observation for halogen ion-pair→valence systems that perpendicular transitions, $\Delta\Omega = \pm 1$, are much weaker than parallel transitions, $\Delta\Omega = 0$ [8]. The 340nm system (f→B, $\Delta\Omega = 0$) is

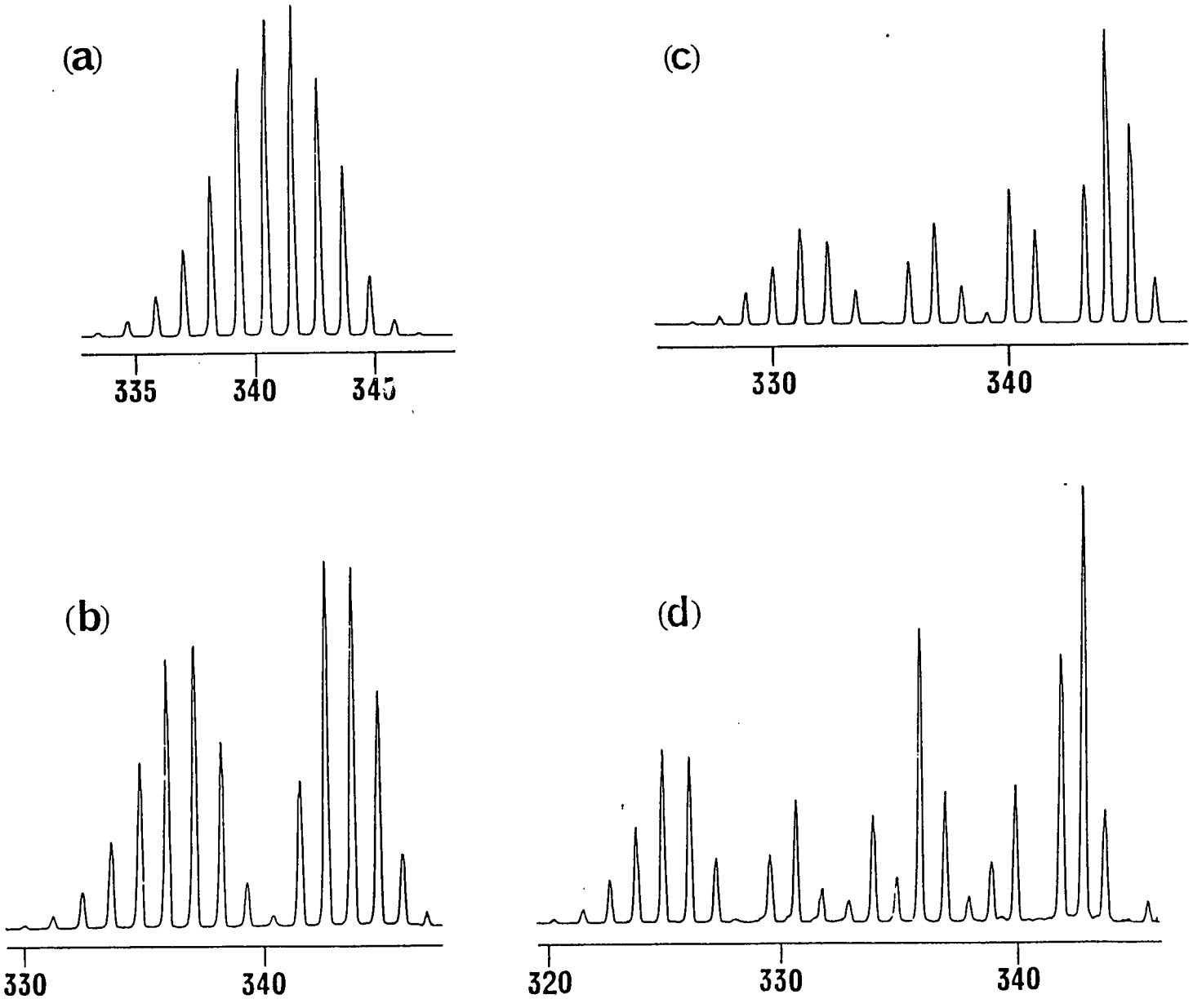

FIGURE 3.3

Dispersed fluorescence spectra:

$I_2(f0_g^+) \rightarrow B(0_u^+)$

(a) v′=0

(b) v′=1

(c) v′=3

(d) v′=5

FIGURE 3.4

Dispersed fluorescence collected following OODR excitation of $I_2(f0_g^+, v'=0, J'=70)$.

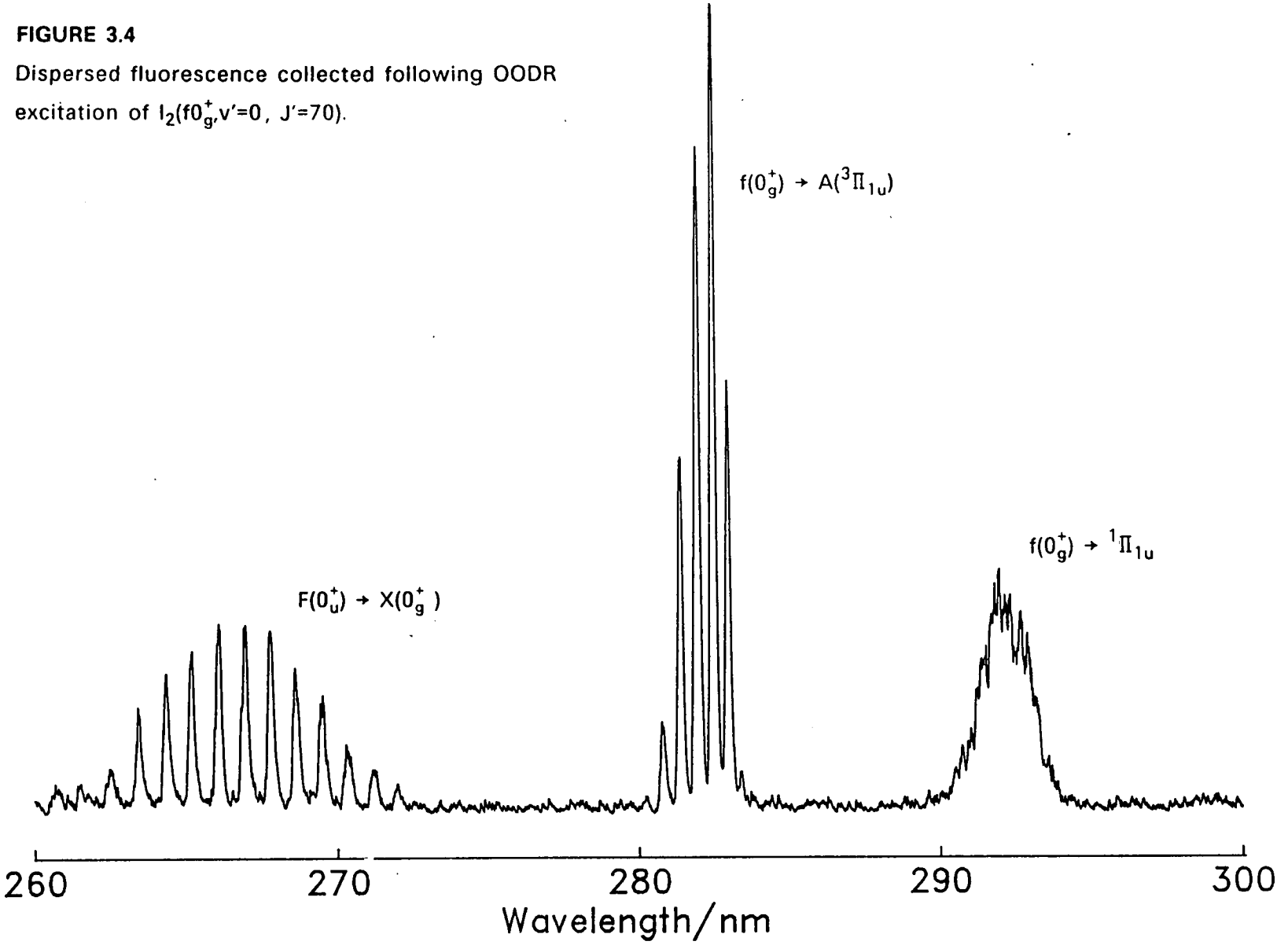

approximately 30 times more intense than the 290 and 280nm bands. The intensity of the 265nm band system relative to the other 3 bands is observed to vary as a function of the pressure of I_2 in the cell. Taking this into consideration, this fluorescence has been assigned to radiative decay of the $F(0_u^+)$ ion-pair state of I_2, populated by collisional transfer from the $f(0_g^+)$ state[6].This has been verified by calculating $F(0_u^+) \rightarrow X(0_g^+)$ band positions, using the available molecular constants [2,9]. A further discussion of this phenomenon is given in section 3.6 . Upon excitation to $I_2(f0_g^+, v' > 11)$ the 280 and 290nm systems are observed to overlap and at $v'>30$ both these systems are obscured by the intense $f \rightarrow B$ fluorescence, which extends increasingly to the blue upon excitation of successively higher vibrational levels.

Following excitation of $f(0_g^+, v' = 25)$ and above , an increasing proportion of fluorescence emission is observed to terminate in the continuum of the B state. The intensity of this bound-free emission displays a complex wavelength dependence. This arises from two discrete interference effects and can be explained in terms of the Franck-Condon principle [10]. In classical terms, the Condon principle states that:

> "electronic rearrangements occur so rapidly with respect to nuclear motion that, during such rearrangements, the positions of the nucleii remain fixed".

This was interpreted to mean that electronic transitions would principally occur at positions where the nucleii spent the greatest time i.e. the classical turning points. However, this neglects the

conservation of nuclear kinetic energy which is implicit in the above statement. The quantum-mechanical Franck-Condon principle, as interpreted by Mulliken[10], gives a more satisfactory description:

> "transitions which correspond to the conservation of nuclear position and kinetic energy are the most probable."

Thus, electronic transitions are equally likely to occur at positions where the nucleii have maximum kinetic energy, rather than from the turning points of the vibrational motion alone, provided that kinetic energy is conserved during the transition. Removal of the caveat "most probable", which allows for non Born-Oppenheimer events, results in the "stationary phase approximation", which restricts calculation of the overlap integral to the regions of the upper and lower state where the vibrational wavefunctions have the same local wavelength.

By taking into consideration the importance of kinetic energy conservation, Mulliken was able to describe the physical processes behind the two observed classes of bound-free emission spectra, namely "reflection" and " internal diffraction" dispersed fluorescence spectra. The region of the lower state sampled by transitions which conserve kinetic energy from a given upper vibronic state is described by the Mulliken difference potential. This is obtained by subtracting the upper potential energy curve from the lower and adding the appropriate vibrational energy for the upper state[10,11]:

$$U(R) = V''(R) + (E_{v'} - V'(R)) \qquad (3.1)$$

Simply taking the difference of the two potentials gives the range of

transition energies which may be observed.

Dispersed continuum emission from halogen ion-pair states generally falls into one of two catergories, depending upon the nature of the lower state. If the lower state is repulsive, then the difference potential will be monotonic. In this case, the intensity pattern of the bound-free emission is determined by the square of the overlap of the upper and lower state vibronic wavefunctions, as a function of internuclear distance. As continuum wavefunctions tend to have almost constant frequency and amplitude, the dispersed emission spectrum adopts the characteristics of the upper state vibrational wavefunctions. Historically, this has been termed as "reflection" of the upper state wavefunction. The number of nodes and peaks in the dispersed emission spectrum matches that of the square of upper state wavefunction and the most intense features correspond to transitions from the classical turning points where the upper state has maximum amplitude (neglecting, for the moment the role of the transition dipole moment function). The term "single frequency oscillatory continuum emission" is now commonly used to describe this phenomenon. The 290nm emission system of $I_2(f0_g^+)$ is a good example of such a system (see Fig 3.4).

For transitions between ion-pair states and bound valence states, the difference potential generally exhibits a maximum. In this case, a second interference effect is observed. Transitions from two nuclear configurations may contribute to emission at a given energy. Depending upon the relative phase of the upper state vibrational wavefunction at the two contributing points, constructive or

destructive interference may be observed. This results in a modulation of the higher frequency structure arising from overlap of the upper and lower vibrational wavefunctions. Prior to Mulliken's explanation of this effect, it had been recognised that the structure in these systems did arise from an interference effect and the term "internal diffraction" was applied to such spectra[10]. The more descriptive term "double frequency oscillatory continuum emission" is now used. The energy of emission to the maximum of the difference potential is independent of the vibrational energy in the upper state. Thus, the wavelength position of the red extremum in such systems remains constant, as the degree of vibrational excitation in the upper state is increased (see Figs 3.6 to 3.9). As this singularity in the difference potential is approached, the number of transitions contributing to a given energy region sharply increases and classically would go to infinity at the maximum. This region is termed the "rainbow", by analogy with observations of a singular trajectory in scattering experiments.

Thus, in double frequency oscillatory continuum spectra, there are three regions in which intensity accumulates. Two arising from the classical turning points and a third corresponding to the rainbow. As indicated on Fig 3.5, transitions from the outer turning point of the upper state will generally terminate close to the lower state continuum, resulting in a build-up of intensity at the margin of the bound-bound and bound-free emission.

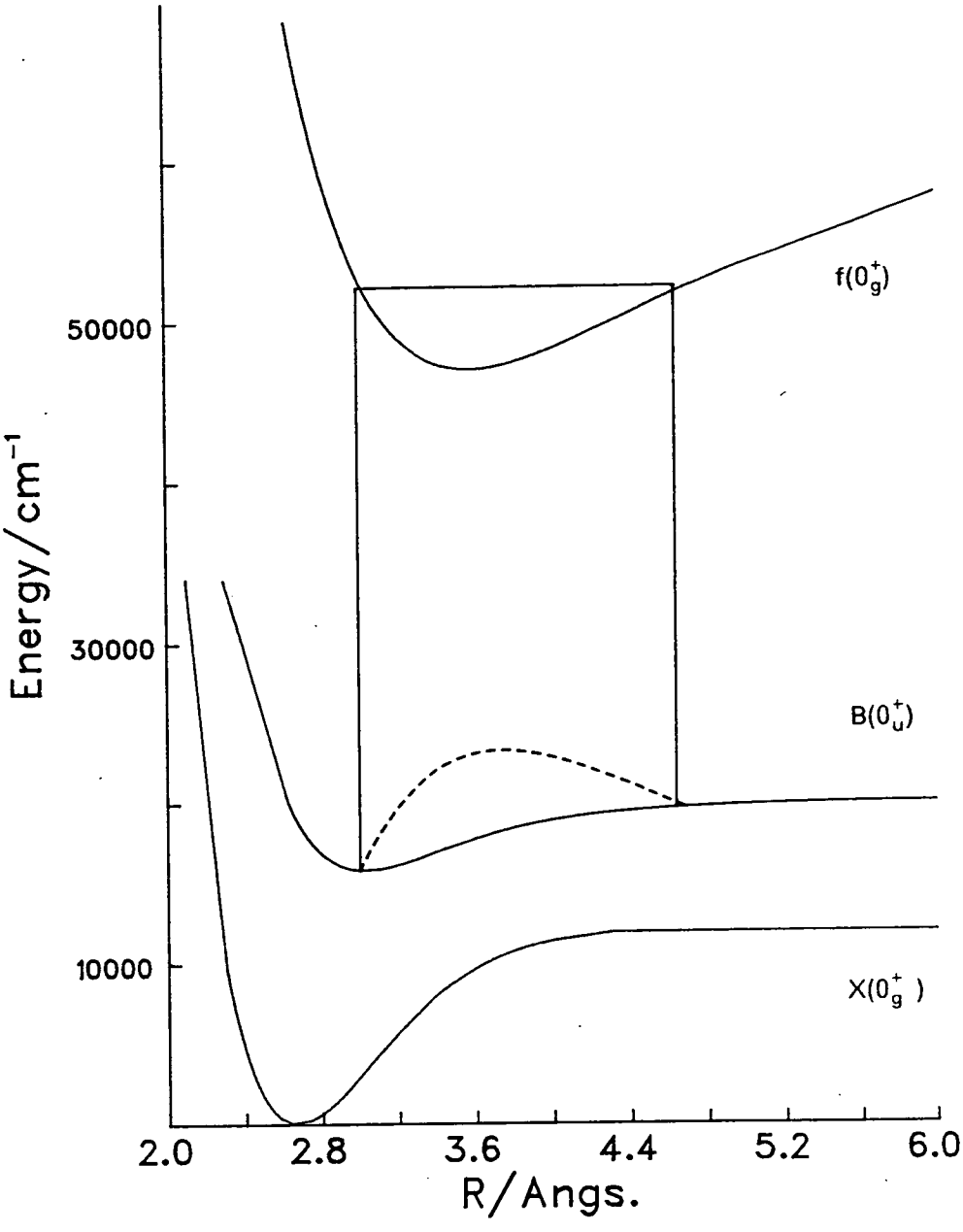

FIGURE 3.5

Mulliken difference potential for the transition:

$f(0_g^+, v'=57) \rightarrow B(0_u^+)$

3.4 Simulations

Simulations of dispersed fluorescence from $f(0_g^+)$ to the $B(0_u^+)$ state have been carried out for a range of f state vibrational levels (figs 3.6–3.9). The RKR curve for the $f(0_g^+)$ state, as tabulated by Perrot et al. up to v'=75, was fitted to a spline function in order to obtain a smooth potential V'(r), with a spacing of 0.001Å over the range 2.9Å to 5.0Å. In order to simulate fluorescence from v'=88, the curve was then extrapolated by fixing the turning points for v'=88 at 2.935Å and 5.150Å respectively, for G_v = 7717.8cm^{-1}. The B state curve was similiarly constructed using the RKR points of Luc up to v'=62[2], within 0.5% of the dissociation limit, at 2.6Å. The repulsive limb was initially modelled using the knot points of Brand and Hoy out to 2.5Å[12]. Small shifts in the repulsive wall were neccessary in order to reproduce the f→B bound-free fluorescence. The knot points employed to describe the repulsive limb between 2.62 and 2.43Å are listed in Table 3.1, along with the values of Brand and Hoy.

Fig 3.6 shows a simulation of dispersed fluorescence from $f(0_g^+$, v'= 13) to the B state. All the transitions terminate on discrete vibronic levels within the B state and the intensity envelope in this case is chiefly determined by the overlap of the f and B state vibrational wavefunctions.

The remaining simulations model both bound-bound emission and double frequency oscillatory continuum fluorescence. Fitting of these simulations with the experimental spectra gives precise information on the repulsive limb of the lower state. The upper state is well known from precise OODR measurements of rovibronic level

Table 3.1

Knot points for the $B(0_u^+)$ potential curve in the continuum region. The values of Brand et. al. are in brackets [12].

r(Å)	V(r) (cm^{-1})	
2.43	12000.0	
2.50	8845.30	
2.55	6884.30	(7084.35)
2.60	5229.55	(5229.55)
2.62	4646.90	(4646.13)

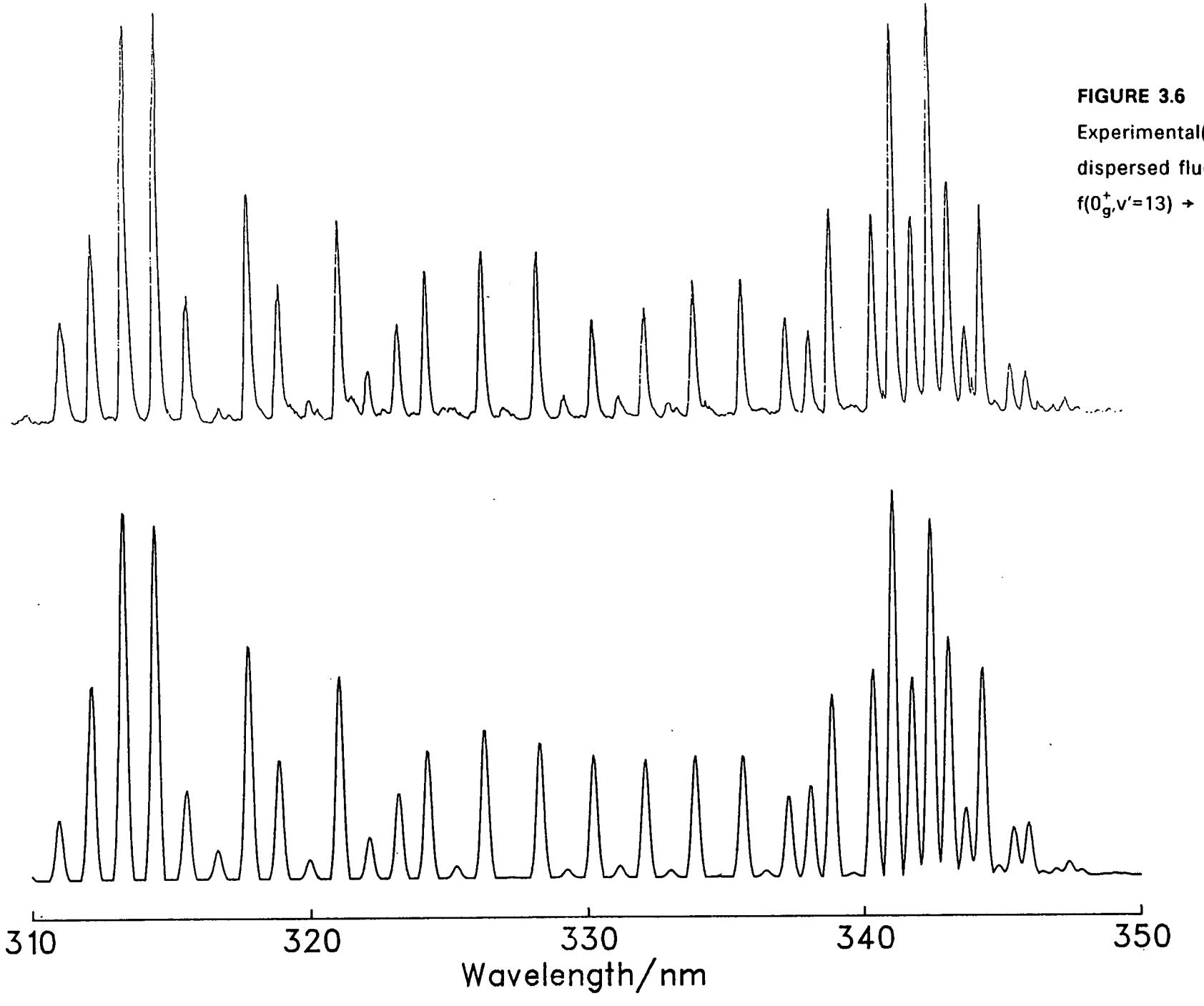

FIGURE 3.6

Experimental(upper) and simulated dispersed fluorescence spectra: $f(0_g^+, v'=13) \rightarrow B(0_u^+)$

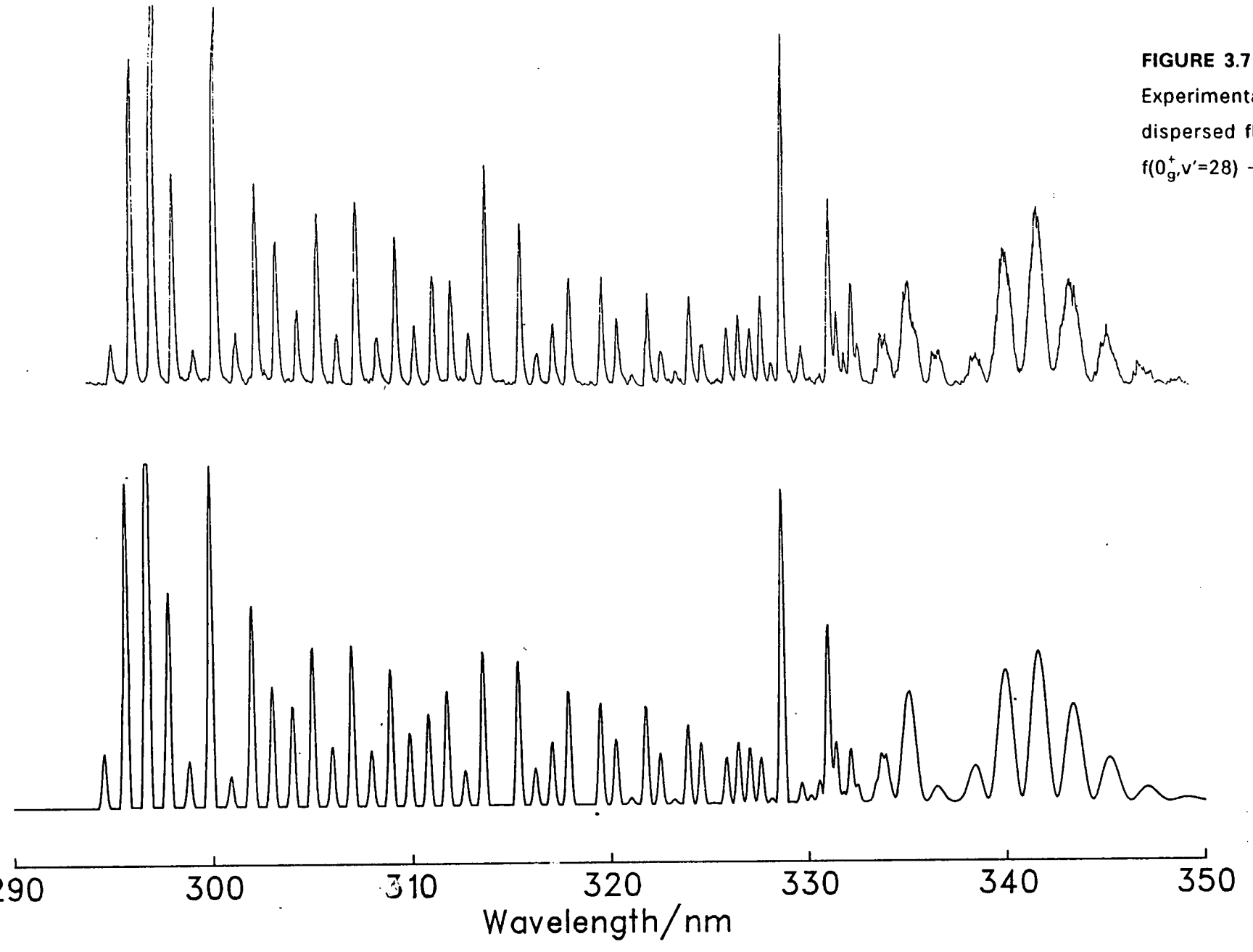

FIGURE 3.7

Experimental(upper) and simulated dispersed fluorescence spectra: $f(0_g^+, v'=28) \rightarrow B(0_u^+)$

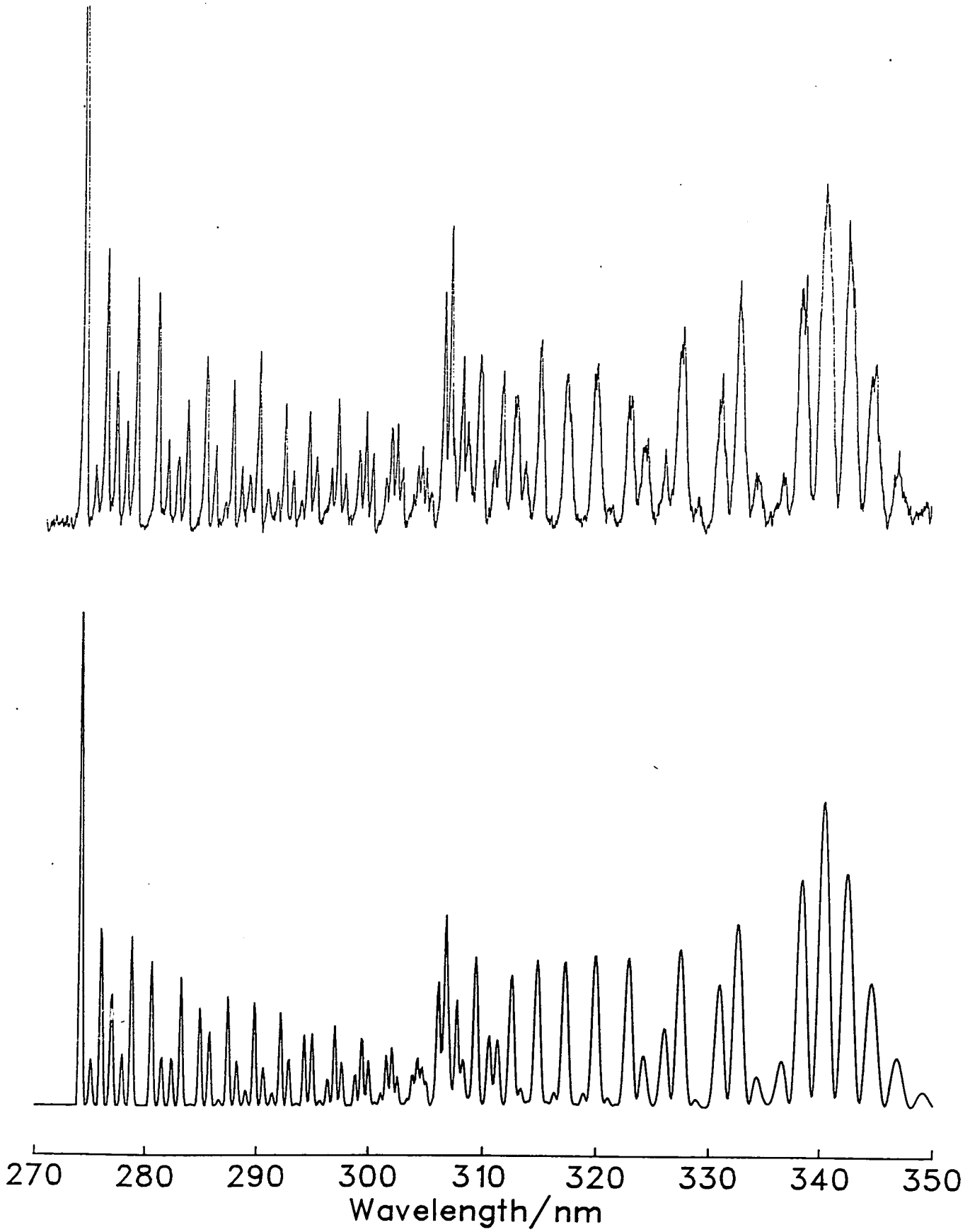

FIGURE 3.8

Experimental(upper) and simulated dispersed fluorescence spectra: $f(0_g^+, v'=57) \rightarrow B(0_u^+)$

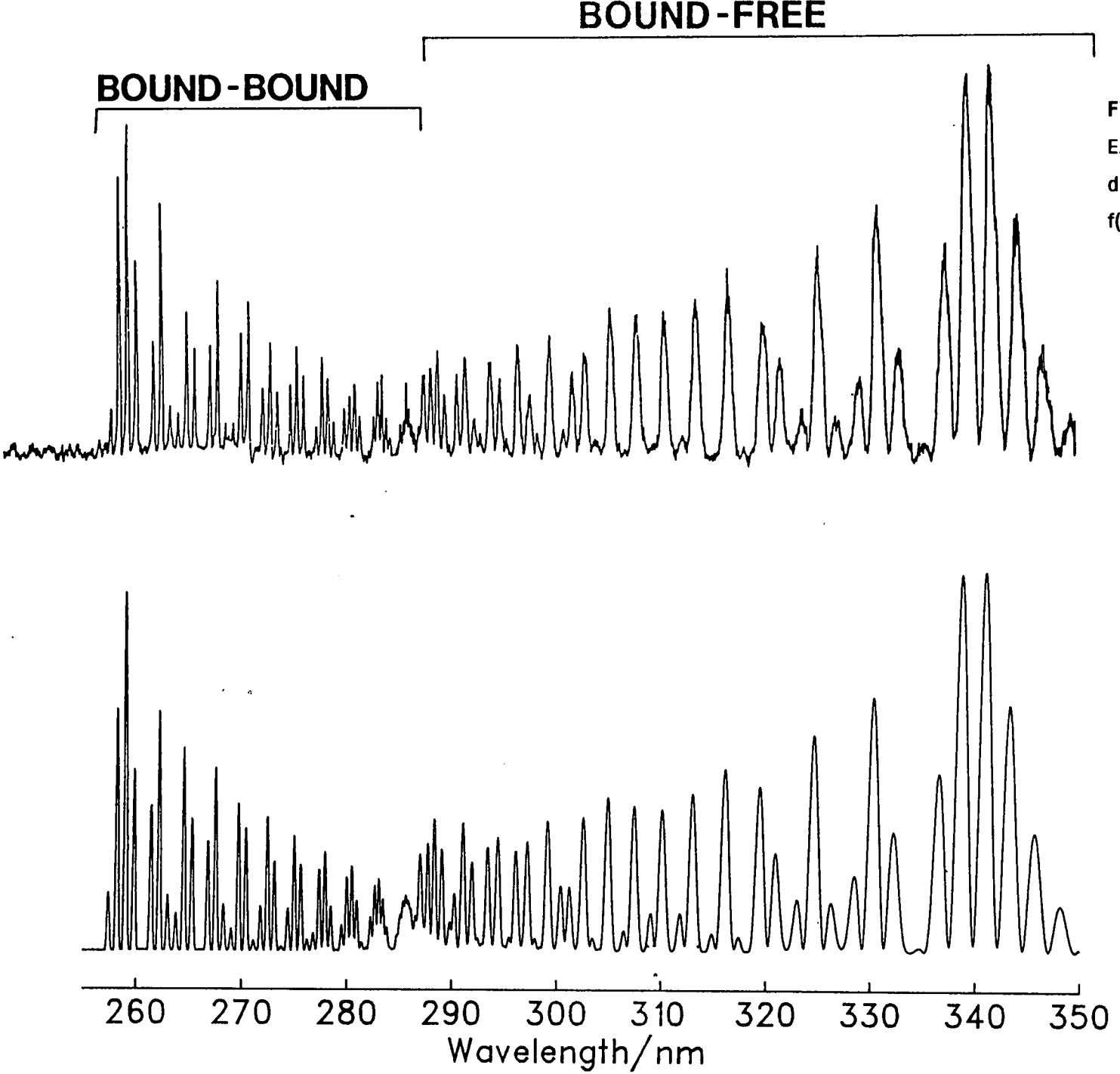

FIGURE 3.9

Experimental(upper) and simulated dispersed fluorescence spectra: $f(0_g^+,v'=88) \rightarrow B(0_u^+)$

positions[4]. The validity of the RKR curve derived from these measurements is confirmed by the close match of simulations of the bound-bound emission with the observed fluorescence spectra. The intensity pattern associated with this bound-bound fluorescence is extremely sensitive to small shifts in the inner wall of the upper state , a clearly discernible effect being brought about by a shift of ±0.002Å. Matching of the double frequency continuum emission allows determination of the B state potential above the dissociation limit, the f state being fixed by the OODR measurements.

3.5 The Transition Dipole Moment Function

3.5.1 Determination of $\mu_{21}(r)$

In simulating the f → B system, a correction has been made for the transition dipole moment function, $\mu_{21}(r)$. This was determined by adjusting a set of points in the region 2.9 to 5.3Å to accurately reproduce the overall intensity pattern from v'=88, the most extensive experimental spectrum. It is important to note that in carrying out a determination of $\mu_{21}(r)$, the experimental monochromator/photomultiplier response must be accurately known as a function of wavelength (sec. 2.4) . It is also critical to account for any possible drift of the dye laser wavelengths as the spectra are collected. High resolution spectra such as those displayed in Figs 3.6 -3.9 may take up to an hour to collect and any drift from either of the resonant frequencies whilst dispersed fluorescence is being recorded, may result in anomalous intensity decreases. In order to eliminate this source of error, fluorescence from v'=88 was recorded

several times, scanning the monochromator in both directions.

The form of $\mu_{21}(r)$ can be ascertained by comparing the experimental spectrum with a simulation carried out with a constant transition dipole moment (Figure 3.10). The ratio of intensities in the bound region gives information on the nature of $\mu_{21}(r)$ at low r, whilst the relative intensity of the bound–free changeover region reveals how much attentuation is required at the outer turning poing of the upper state. The peak to valley ratio, or degree of "filling in", between peaks is governed by interference between the two limbs of the difference potential and is a useful test of $\mu_{21}(r)$. Fig 3.11 shows the form of $\mu_{21}(r)$ adopted for the simulation of f → B fluorescence.

3.5.2 Interpretation

The transition dipole moment function, $\mu_{21}(r)$, can be expressed as follows:

$$\mu_{21}(r) = \int \psi_e^{*'} \mu \psi_e'' \, d\tau_e \quad (3.2)$$

The relative magnitude of $\mu_{21}(r)$ as a function of internuclear distance is thus governed by the overlap of the upper and lower state electronic wavefunctions. The observed fall–off in $\mu_{21}(r)$ to large r is well known for a range of halogen ion–pair → valence fluorescence systems and was originally predicted by Mulliken in 1939[13]. Around r_e, molecular ion–pair states are best described by considering the combination of the separate ions (see Chapter 1). An ion–pair → valence transition will thus involve transfer of an electron from one end of the molecule to the other. As the internuclear distance increases, this electronic rearrangement becomes

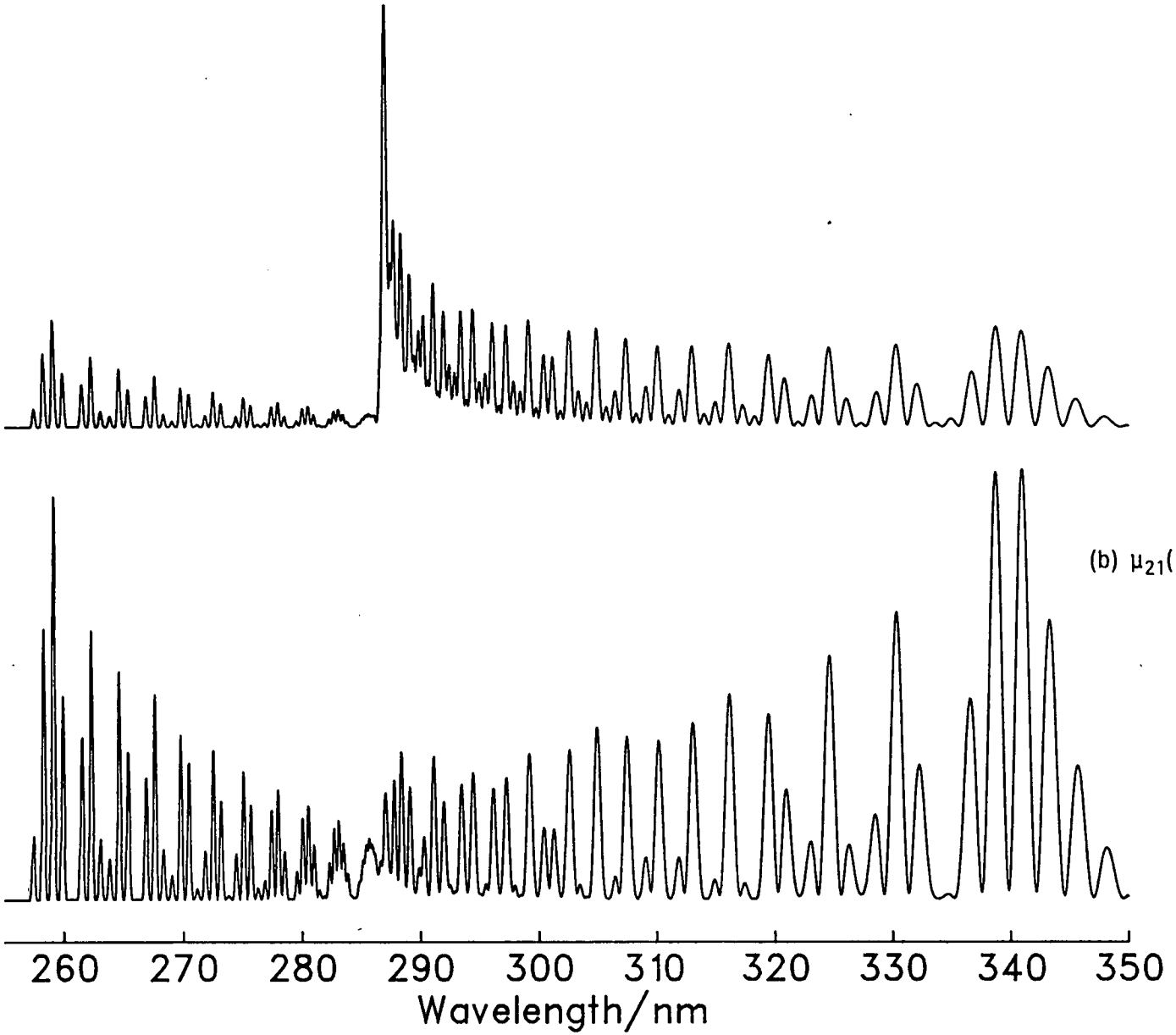

FIGURE 3.10

Simulations of $I_2(f0_g^+, v'=88) \rightarrow B(0_u^+)$

(a) $\mu_{21}(r)$ = constant

(b) $\mu_{21}(r) = -1.925 + 15.15r - 3.674r^2 + 0.2845r^3$

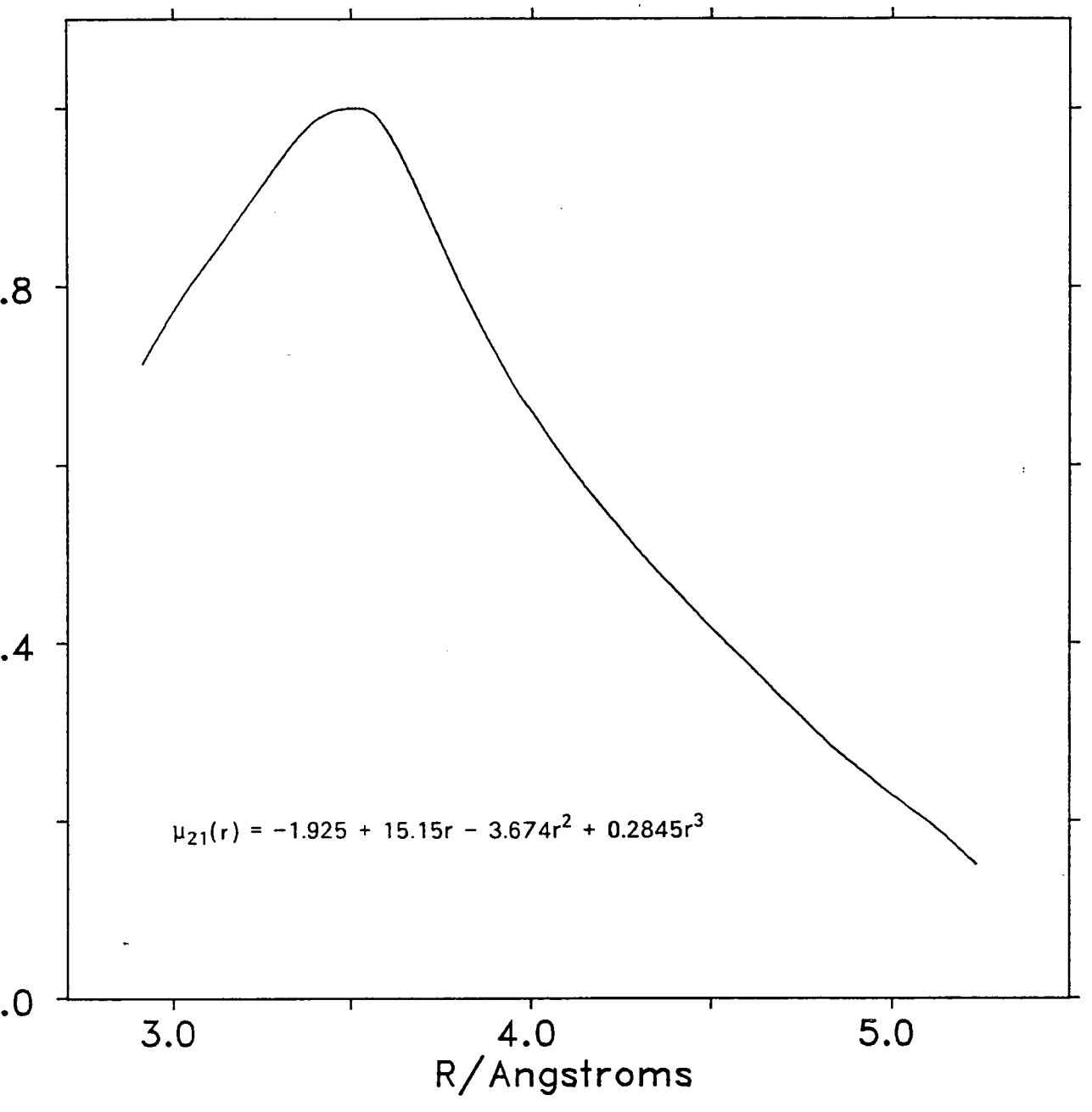

FIGURE 3.11

$\mu_{21}(r)$, derived from simulation of f(v'=88) → B.

increasingly difficult and is forbidden in the separated-ion limit. This is reflected in the decreasing overlap between the f and B state electronic wavefunctions as r increases and thus, $\mu_{21}(r)$ is observed to decrease. Mulliken adopted model ion-pair and valence wavefunctions for this charge-transfer process and directly calculated $\mu_{21}(r)$ from the overlap of the electronic wavefunctions[13]. He predicted that $\mu_{21}(r)$ must monotonically decrease on going to larger separations. For any given value of r, the sum of the oscillator strengths for the available decay channels is constant. Hence, as ion-pair → valence transitions become increasingly unlikely at large r, it is expected that most of the oscillator strength will reside in ion-pair → ion-pair transitions. This has been exploited recently by Hoy and Taylor, who have reported excitation of the $f'(0_g^+)$ state of I_2 in the third ion-pair cluster, by employing a near infra-red transition from $F(0_u^+)$[14].

$\mu_{21}(r)$ is also observed to decrease on going to smaller separations. In the region of the inner limb of the potential curve, the electrons in the ion-pair molecule become increasingly delocalised, and the molecular orbital description becomes more appropriate. In this case, the dominant M.O. configuration for the f state is expected to be 2242 (in Mullikens notation, see Chapter 1), becoming more important as r is decreased. Fluorescence to the 2431 B state involves a two electron change from the 2242 configuration and thus f → B fluorescence becomes increasingly forbidden at small r.

3.6 Collisional relaxation of $I_2(f0_g^+)$ by I_2

Collision-induced transfer from $I_2(f0_g^+)$ into other ion-pair states is observed to occur even in the absence of buffer gases, as a result of quenching by $I_2(X0_g^+)$. Although there are many available states for inter ion-pair state transfer, the $F(0_u^+)$ state is most efficiently populated. Lawley has recently postulated two possible mechanisms for this highly efficient g→u transfer [15]. The dominant contribution to the transfer process arises from formation of a close-coupled collision complex $I_2^*-I_2$, giving rise to orbiting controlled cross-sections of ca.150Å^2 for g↔u transfer at room temperature. In addition, an enhancement of ca. 15% has been predicted for the case when the collisionally coupled states are near-resonant ($\Delta E < 5cm^{-1}$). This long-range coupling arises from interaction of the transition dipole moment of the homonuclear ion-pair state molecule with the permanent quadrupole moment of the ground state.

The $f(0_g^+) \rightarrow F(0_u^+)$ transfer process has been studied previously by Butler et al. at I_2 pressures of ca.30mtorr[16]. The object of the work reported here was to extend the above study, in order to gain information on the mechanism of f→F collisional transfer.

3.6.1 Results

The following transfer processes were studied at I_2 pressures of 100 and 230mtorr:

$$f(0_g^+,\ v=0-4,\ J=70) \rightarrow F(0_u^+,\ v=n)$$

Dispersed fluorescence spectra collected at an I_2 pressure of 230m

torr are displayed in fig 3.12. Three distinct spectroscopic systems are observed. The 280 and 290nm systems are readily assigned as $f(0_g^+) \rightarrow A(^3\Pi_{1u})$ and $f(0_g^+) \rightarrow {}^1\Pi_{1u}$ (section 3.2). The intensity of the 265nm system is dependent upon the I_2 pressure and can be assigned to $F(0_u^+) \rightarrow X(0_g^+)$, using the known molecular constants for the F and X states [2,9]. $F(0_u^+)$ vibrational state population distributions have been determined by direct spectral simulations. The experimental and simulated spectra for pI_2=230mtorr are shown in Figs 3.13 to 3.16. The results are summarised in Table 3.2, along with the distributions obtained following excitation of $f(0_g^+$,v'=1 and 3) at 100mtorr. In order to accurately determine the monochromator slit width, the resolution of the f→A fluorescence was estimated from simulations of this system by assuming that a single rovibronic level of the f state had been excited and that each peak in the f → A bound-bound spectrum contained only P,Q and R rotational transitions. On this basis, it is estimated that the F→X spectra only contain contributions from a very narrow range of J, implying that the transfer process is rotationally specific.

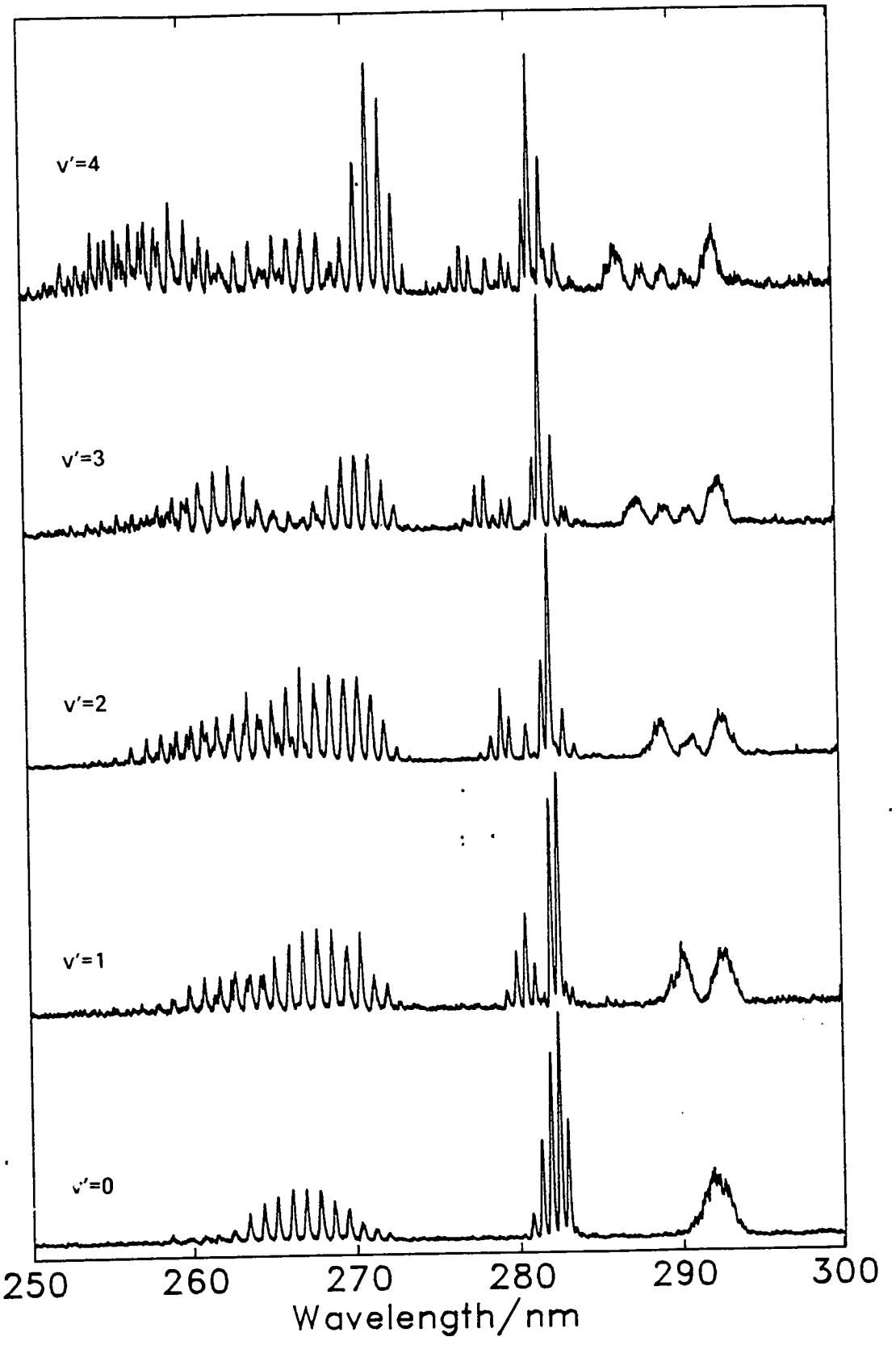

FIGURE 3.12

Dispersed fluorescence spectra collected following excitation of $I_2(f0_g^+, v'= 0-4, J'=70)$

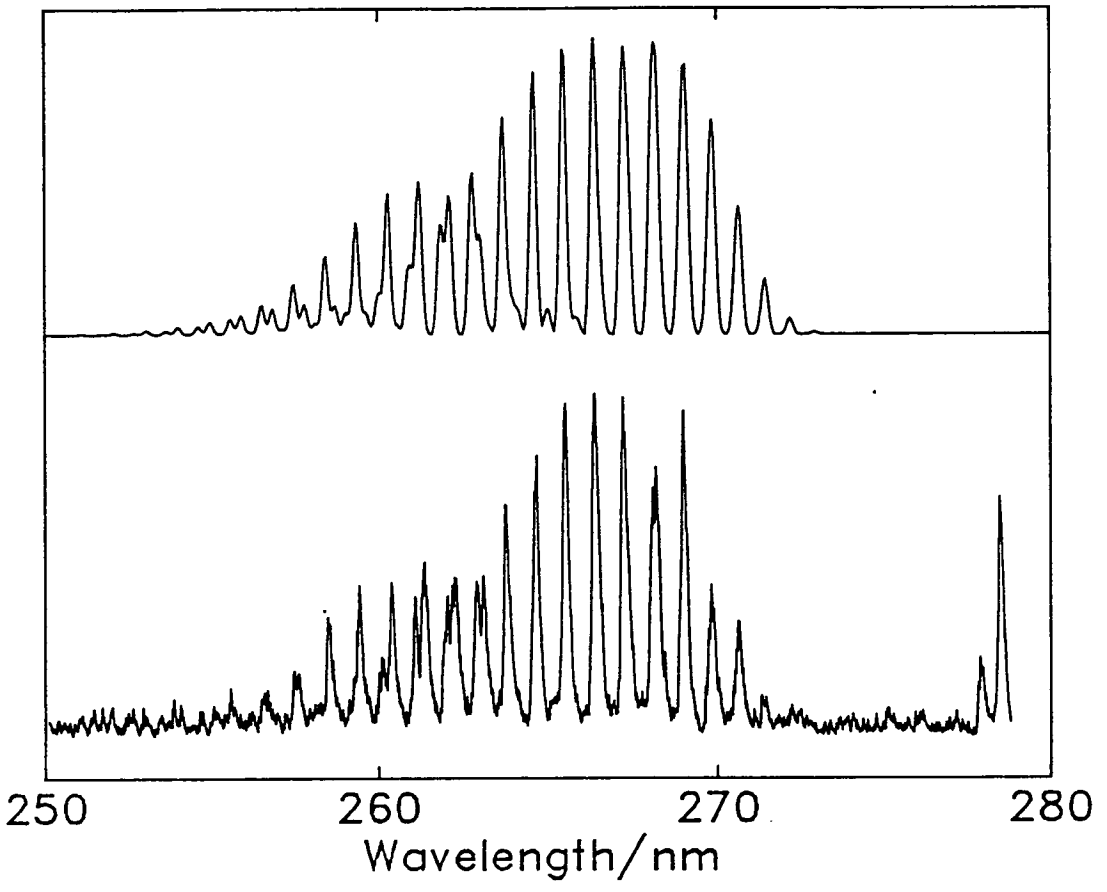

FIGURE 3.13

Experimental(lower) and simulated dispersed fluorescence from $I_2(F0_u^+)$, following excitation of: $I_2(f0_g^+, v'=1, J'=70)$.

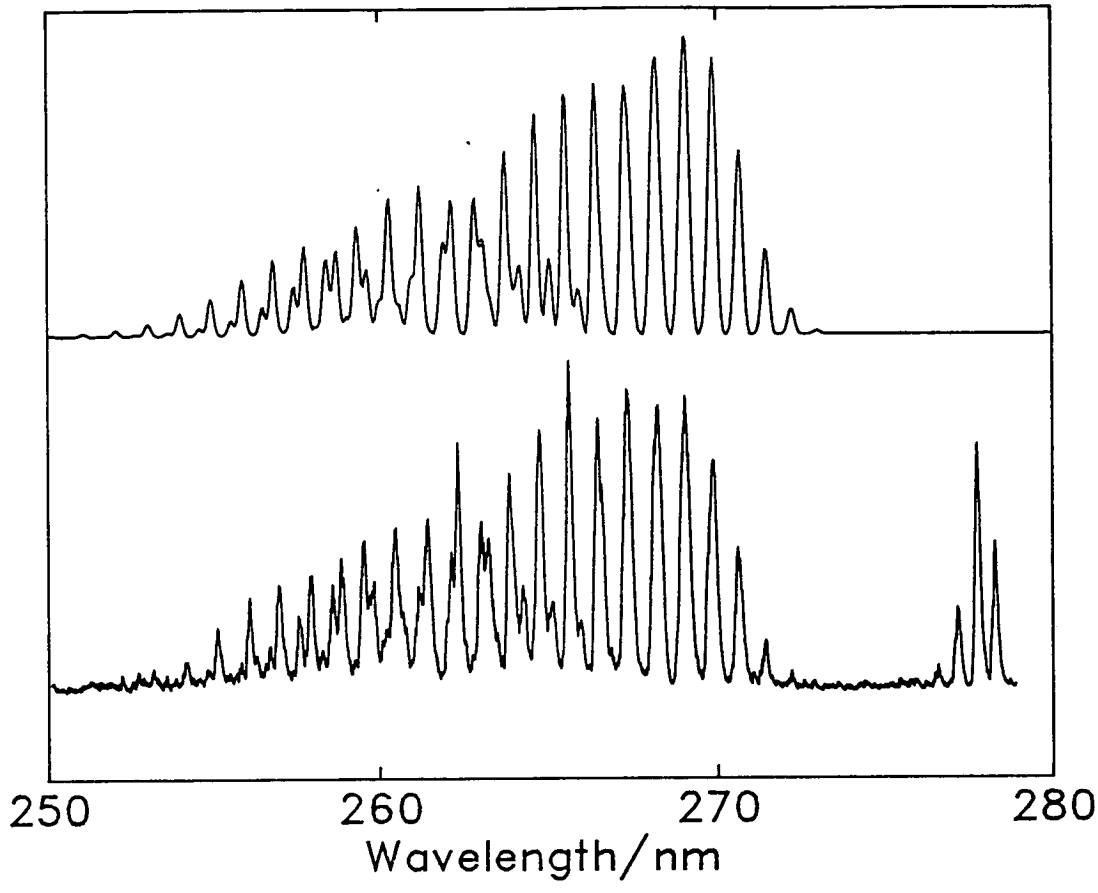

FIGURE 3.14

Experimental(lower) and simulated dispersed fluorescence from $I_2(F0_u^+)$, following excitation of: $I_2(f0_g^+, v'=2, J'=70)$.

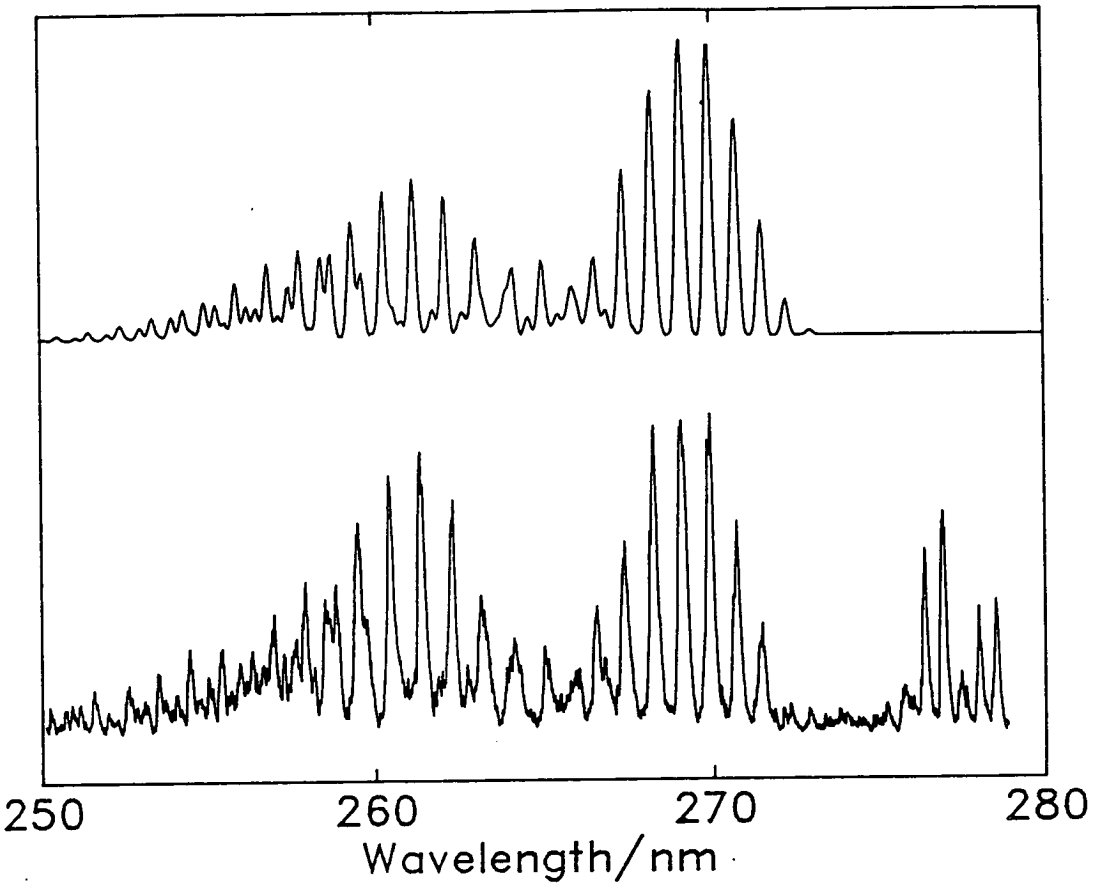

FIGURE 3.15

Experimental(lower) and simulated dispersed fluorescence from $I_2(F0_u^+)$, following excitation of: $I_2(f0_g^+, v'=3, J'=70)$.

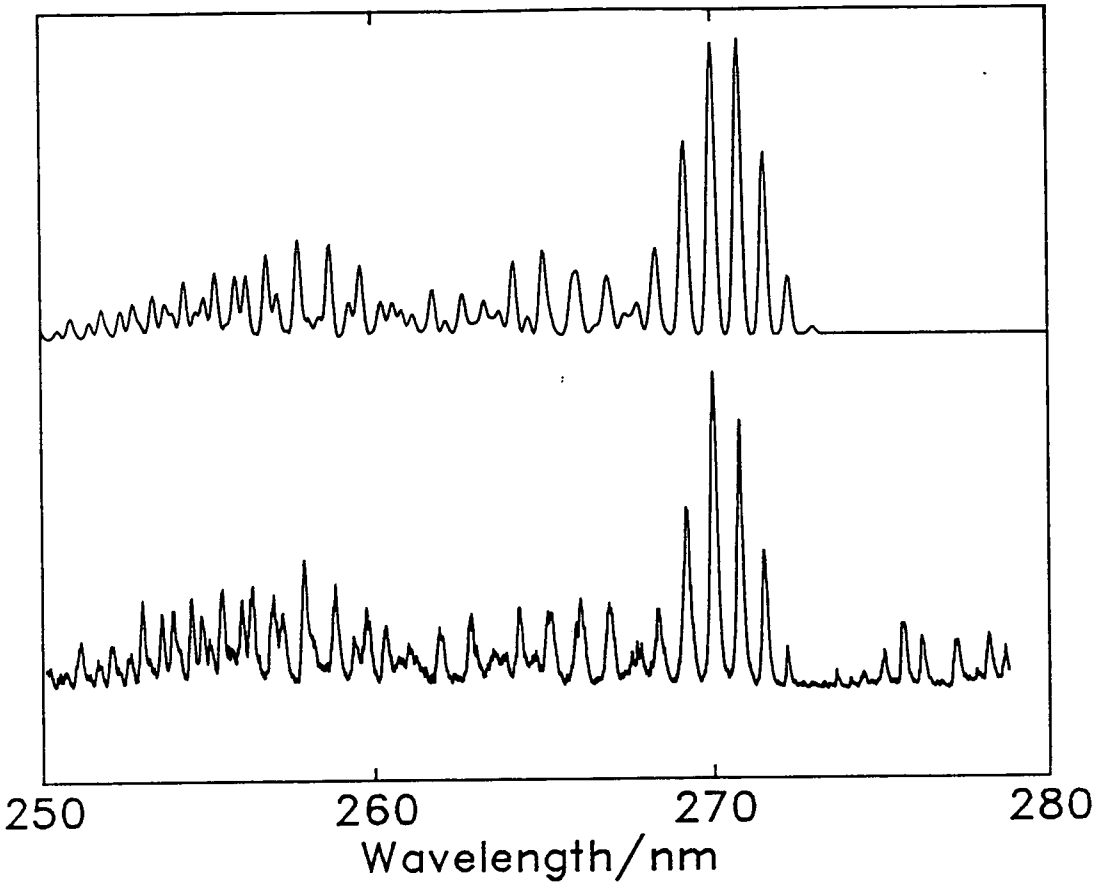

FIGURE 3.16

Experimental(lower) and simulated dispersed fluorescence from $I_2(f0_u^+)$, following excitation of: $I_2(f0_g^+, v'=4, J'=70)$.

Table 3.2

Estimated $F(0_u^+)$ state vibrational population distributions, observed following collisional quenching of $f(0_g^+)$.

		$F(0_u^+)$,v				
$f(0_g^+)$,v	$p(I_2)$mtorr	0	1	2	3	4
0	230	1.0	–	–	–	–
1	230	0.55	0.40	0.05	–	–
	100	0.25	0.75	–	–	–
2	230	0.40	0.34	0.26	–	–
3	230	0.04	0.42	0.29	0.25	–
	100	0.05	0.75	0.2	–	–
4	230	–	0.06	0.42	0.31	0.21

3.6.2 Discussion

The simulations of F → X fluorescence clearly indicate that, at 230mtorr, fluorescence occurs from several vibrational levels of the $F(0_u^+)$ state. However, no vibrational relaxation has been detected in the f → A or f → $^1\Pi_{1u}$ systems. f→F collisional transfer has been studied previously by Butler et al., who reported that, at pressures of 30mtorr, g → u transfer is vibrationally specific. It therefore appears that at 230mtorr, vibrational relaxation within the $F(0_u^+)$ state is taking place. This leads to the conclusion that the $F(0_u^+)$ state must have a significantly longer radiative lifetime that the $f(0_g^+)$ state, as no vibrational relaxation within this state is observed.

Butler et al. have proposed that transfer out of $f(0_g^+$, v'=0 and 1) into the F state is achieved by collisions with vibrationally excited $X(0_g^+$, v" = 1) ground state molecules, which form 29% of the I_2 population at room temperature. The excess vibrational energy in the quenching partner is ca. 214cm^{-1} , equivalent to the difference in energy between the $f(0_g^+)$ and $F(0_u^+)$ states. This leads to specific transfer from f(v=n) to F(v=n) for v=0 and 1. Transfer from f(v=2) and above to $F(0_u^+)$ does not require any energy input and specific transfer from f(v=n) to F(v=n−2) is observed. This is confirmed by measurements of the population distributions for f(v=1,3) → F, as a function of I_2 pressure, which indicate that F(v=1) becomes dominant as the I_2 pressure is decreased (Table 3.2).

From the simulations described above, it can be concluded that the g → u transfer process is rotationally specific. This favours the long-range resonant mechanism described by Lawley, although the

smallest energy mismatch between the coupled states is ca. $25cm^{-1}$, somewhat larger that the critical value of $<5cm^{-1}$ predicted by Lawley for the long-range coupling process. However, vibrational relaxation within the $F(0_u^+)$ state itself appears to be rotationally specific and this will almost certainly require a close-coupled interaction. It thus appears that for J=70, rotational relaxation is not a facile process. If this is the case then it is possible that g → u transfer is orbiting controlled, but rotational scrambling does not occur within the collision complex.

This is clearly a fertile area for further study and in particular the measurement of quenching cross-sections and product state distributions as a function of J should give further insight into the transfer mechanism.

3.7 References

1. S. Gerstenkorn and P. Luc, "Atlas du spectre d'absorption de la molécule d'iode", (CNRS, Paris, 1978)
2. P. Luc, J. Mol. Spec. **80**, 41 (1980)
3. J.M. Hollas, "High Resolution Spectroscopy", (Butterworths, 1984)
4. J.P. Perrot, A.J. Bouvier, A. Bouvier, B. Femelat and J. Chevaleyre, J. Mol. Spec. **114**, 60 (1985)
5. H.P. Grieneisen and R.E. Francke, Chem. Phys. Lett. **88**, 585 (1982)
6. U. Heeman, H. Knöckel and E. Tiemann, Chem. Phys. Lett. **90**, 17 (1982)

7. J. Tellinghuisen, J. Chem. Phys. **82**, 4012 (1985)
8. R.S. Mulliken, J. Chem. Phys. **55**, 288 (1971)
9. A.R. Hoy and J.C.D. Brand, Chem. Phys. **109**, 109 (1986)
10. R.S. Mulliken, J. Chem. Phys. **55**, 309 (1971)
11. J.B. Tellinghuisen, J. Mol. Spec. **103**, 455 (1984)
12. J.C.D. Brand, A.R. Hoy, A.K. Kalkar and A.B. Yamashita, J. Mol. Spec. **95**, 350 (1982)
13. R.S. Mulliken, J. Chem. Phys. **7**, 20 (1939)
14. A.R. Hoy and A.W. Taylor, J. Mol. Spec. **126**, 484 (1987)
15. K. Lawley, Chem. Phys. **127**, 363 (1988)
16. A. Butler, P. Cartwright and P.R.R. Langridge-Smith, Unpublished results.

Chapter 4
SPECTROSCOPY OF THE FIRST ION-PAIR CLUSTER OF I_2

4.1 Introduction

An analysis of dispersed fluorescence spectra from the $E(0_g^+)$, $\beta(1_g)$ and $\gamma(1_u)$ ion-pair states of I_2 is presented in this chapter. To date, the available information on fluorescence transitions from the first ion-pair manifold of I_2 is rather incomplete. As a result of this, many of the bands observed following quenching of electronically excited I_2 remain unassigned.

The object of the work described in this chapter was to populate as many of states of the first ion-pair cluster of I_2 as are accessible from the $X(0_g^+)$ ground state in two-colour, 1+1 OODR excitation. By dispersing fluorescence emission, it was hoped to establish the principal radiative decay routes for these states.

4.2 Dispersed Fluorescence from $E(0_g^+)$

The $E(0_g^+)$ state of I_2 has been excited in a 1 + 1 optical-optical double resonance experiment. The I_2 molecules were pumped to the $B(0_u^+)$ state and the second laser then used to excite selected rovibronic levels of the $E(0_g^+)$ ion-pair state.

$$E(0_g^+) \overset{2}{\leftarrow} B(0_u^+) \overset{1}{\leftarrow} X(0_g^+)$$

1. (17-1) P(70)

2. (n-17) P,R(69)

This gives rise to P and R branches upon scanning the second dye laser over each vibrational band.

Dispersing emission from the $E(0_g^+)$ state reveals three separate

fluorescence systems. The strongest of these involves the well known transition to the $B(0_u^+)$ state at 430nm[1→4]. Fig 4.1 shows fluorescence from $E(0_g^+,v'=0)$ to bound levels of the B state. This spectrum is fully rotationally resolved and the P and R branches observed confirm that this transition has $\Delta\Omega=0$. The assignment of $B(0_u^+)$ as the lower state has been confirmed using the known spectroscopic constants for the E and B states and by simulating the experimental spectrum using RKR potential curves constructed from the molecular constants[3,5].

Two new fluorescence systems are observed to the blue of the E → B emission, at 336 and 346nm (see Fig 4.2). These systems are approximately 12 times less intense than the E → B band and are assigned to $\Delta\Omega=1$ transitions. The 336nm bound-bound transition is thought to terminate on the $A(^3\Pi_{1u})$ state, whilst the 346nm continuum involves the $^1\Pi_{1u}$ valence state. Both these states correlate diabatically with ground state atomic dissociation products. These transitions are analogous with the 280 and 290nm systems originating from the $f(0_g^+)$ state which have been assigned as f → $A(^3\Pi_{1u})$ and f → $^1\Pi_{1u}$ respectively[6]. The above assignments have been confirmed using the published constants for the $A(^3\Pi_{1u})$ state[7] and the $^1\Pi_{1u}$ repulsive potential, derived from simulations of the f → $^1\Pi_{1u}$ system [19].

The E → $^1\Pi_{1u}$ system shows the characteristic "reflection" structure associated with a transition to a repulsive lower state, where the difference potential does not possess a maximum. In this case, the number of valleys in the dispersed fluorescence spectrum

FIGURE 4.1

Rotationally resolved dispersed fluorescence:

$E(0_g^+, v'=0, J'=70) \rightarrow B(0_u^+)$ *laser line

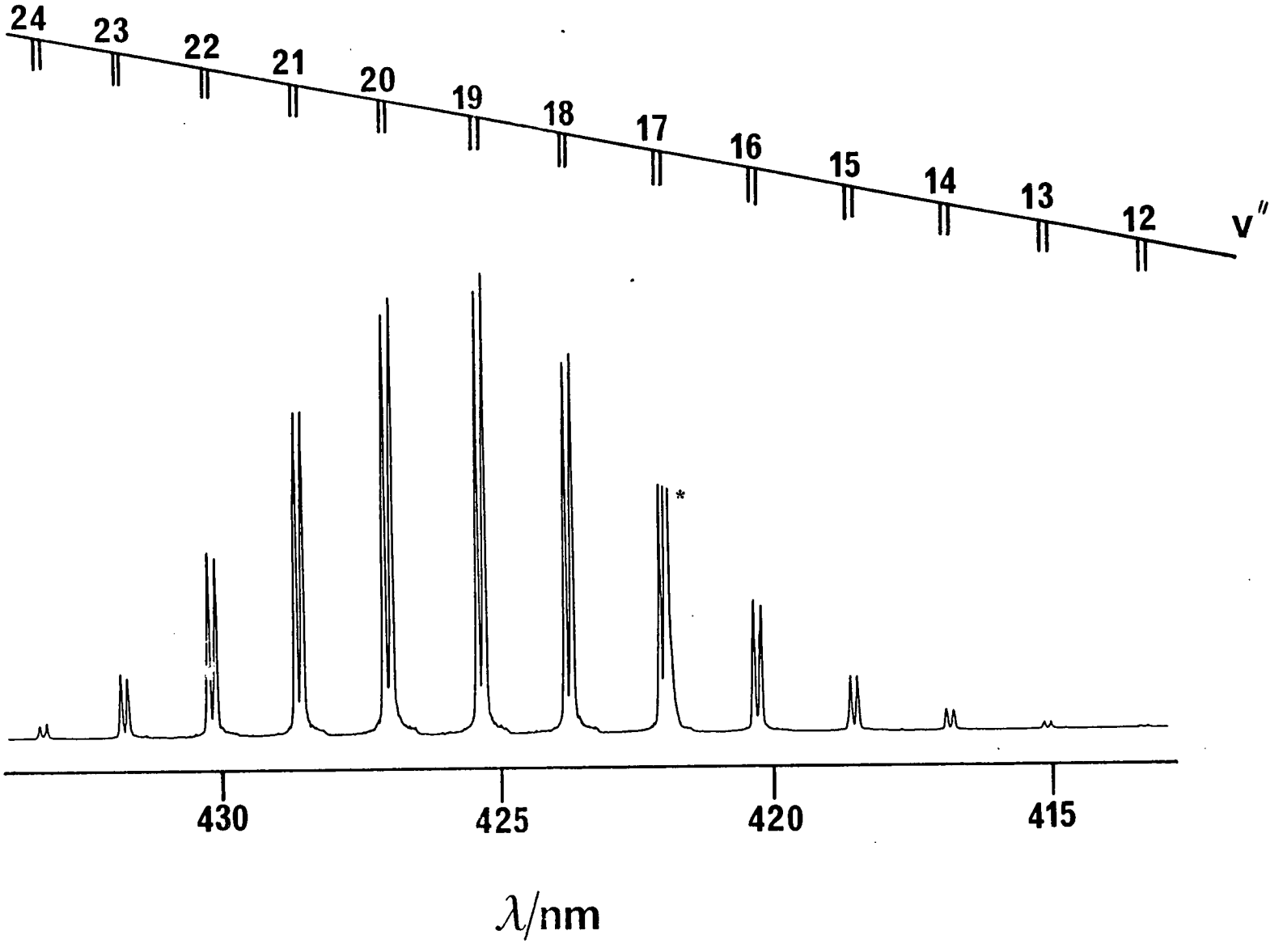

is expected to equal the number of nodes in the upper state vibrational wavefunction. This can be directly verified from Figure 4.2

4.3 Dispersed fluorescence from $\beta(1_g)$

The $\beta(1_g)$ ion-pair state of I_2 has been characterised by Perrot et al. in an optical-optical double resonance fluorescence excitation study[9]. Although the potential energy curve for this state is now well determined for $v' < 45$, there is very little information to date on the position and nature of fluorescence from the β state[4]. Using the OODR technique, the $\beta(1_g, v'=0$ and $1, J'=70)$ states have been successfully populated. Vibrationally and rotationally resolved dispersed emission originating from these states has been recorded. The following double resonance scheme was utilised:

$$\beta(1_g) \overset{2}{\leftarrow} B(0_u^+) \overset{1}{\downarrow} X(0_g^+)$$

1. (17-1) P(70)
2. (n-17) P,Q,R(69)

The second step involves a change in the total electronic angular momentum, Ω , of +1, giving rise to P, Q and R branches in excitation. Fig 4.3 shows the dispersed fluorescence emission spectra obtained following excitation of $\beta(1_g, v'=0$ and $1, J'=70)$. Three distinct emission systems are observed.

The spectrum is dominated by the strong band centred on 341nm. This can be assigned to $\beta(1_g) \rightarrow A(^3\Pi_{1u})$ using the known molecular constants for these states to calculate the band positions and simulate the dispersed fluorescence spectra[7,9]. Fig 4.4 displays

FIGURE 4.2

Dispersed fluorescence from $E(0_g^+)$

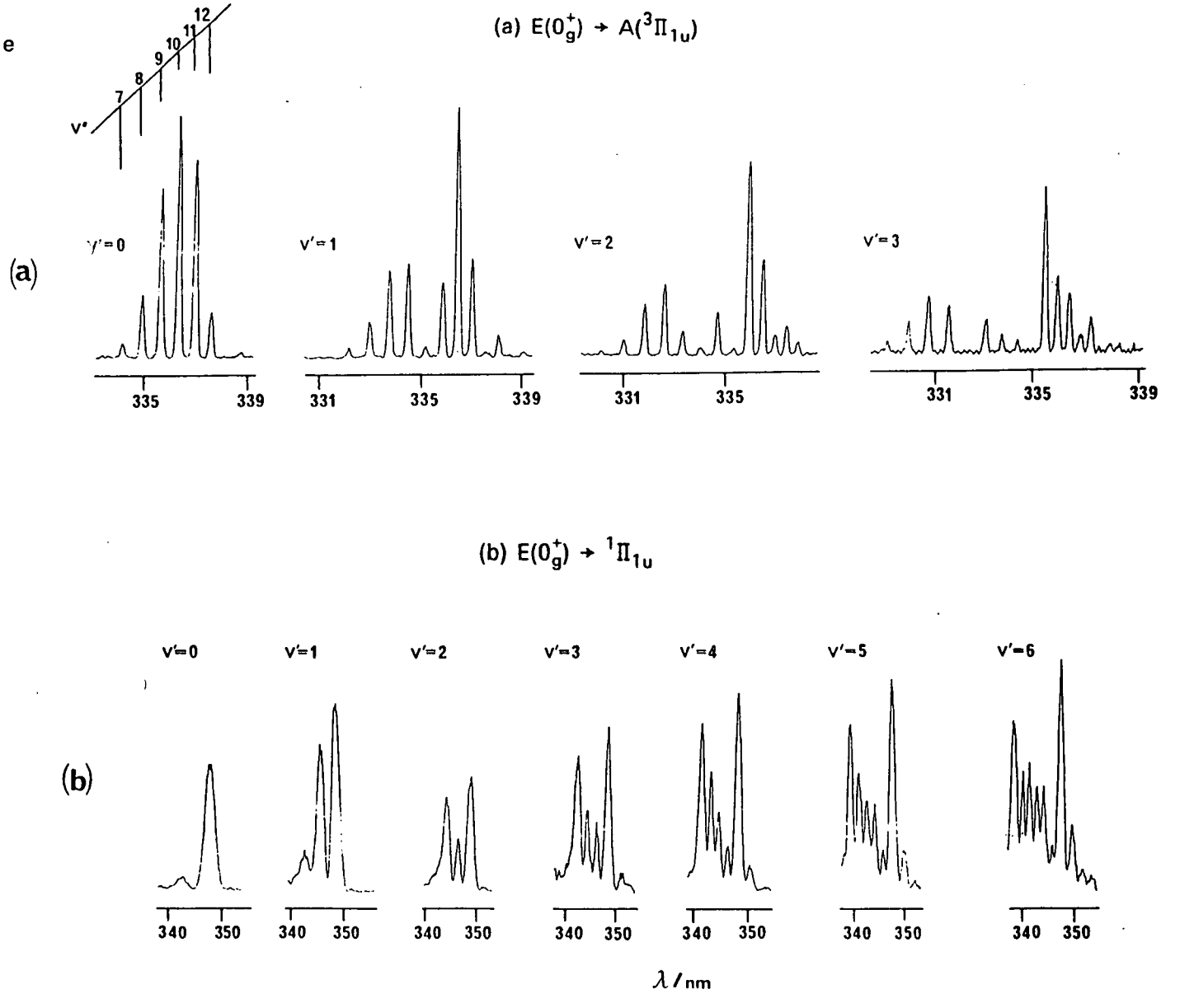

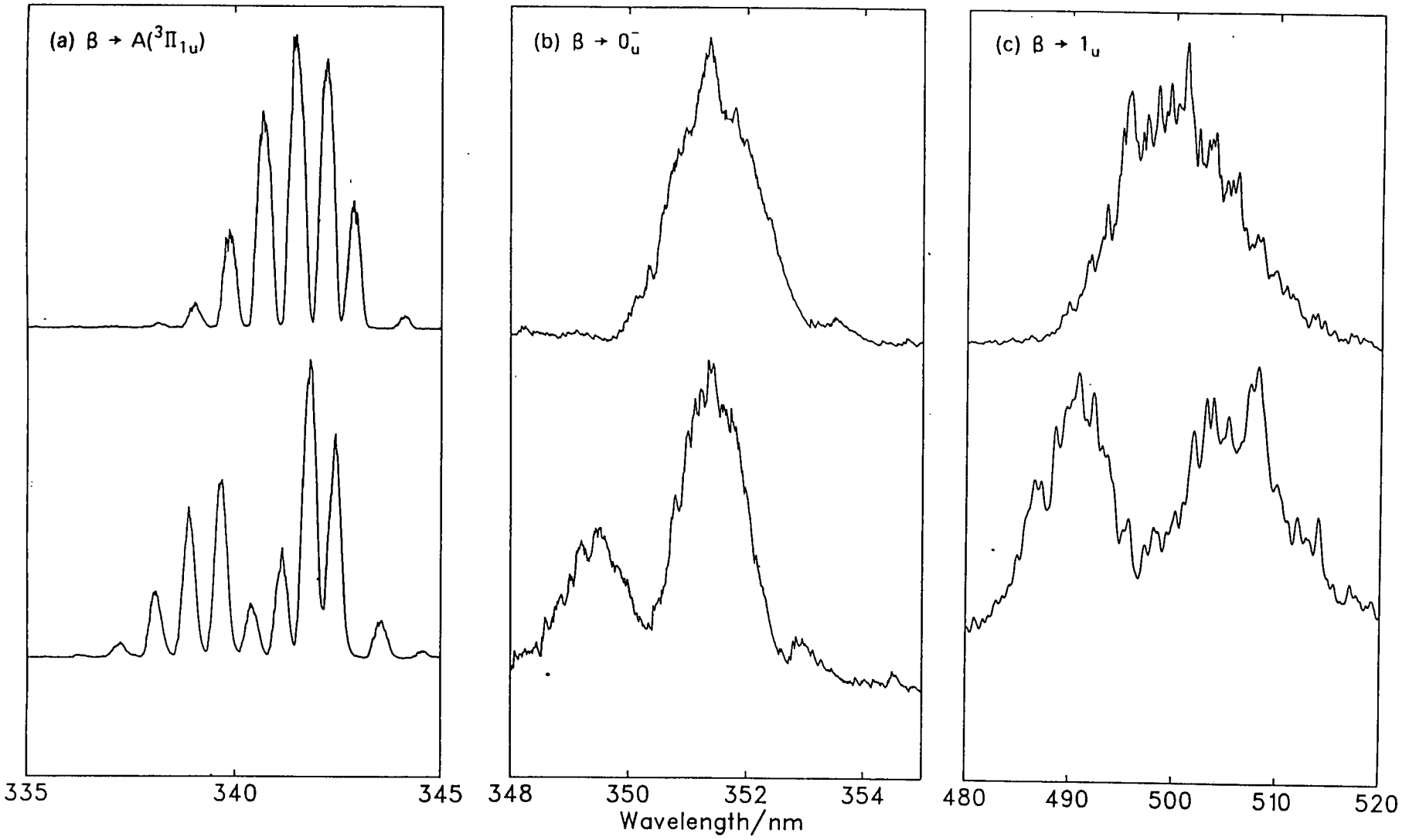

FIGURE 4.3

Dispersed fluorescence from β(1_g,v'= 0 and 1):
(v'=0:upper)

FIGURE 4.4

Rotationally resolved dispersed fluorescence:
from $\beta(1_g, v'=0, J'=70) \rightarrow A(^3\Pi_{1u})$

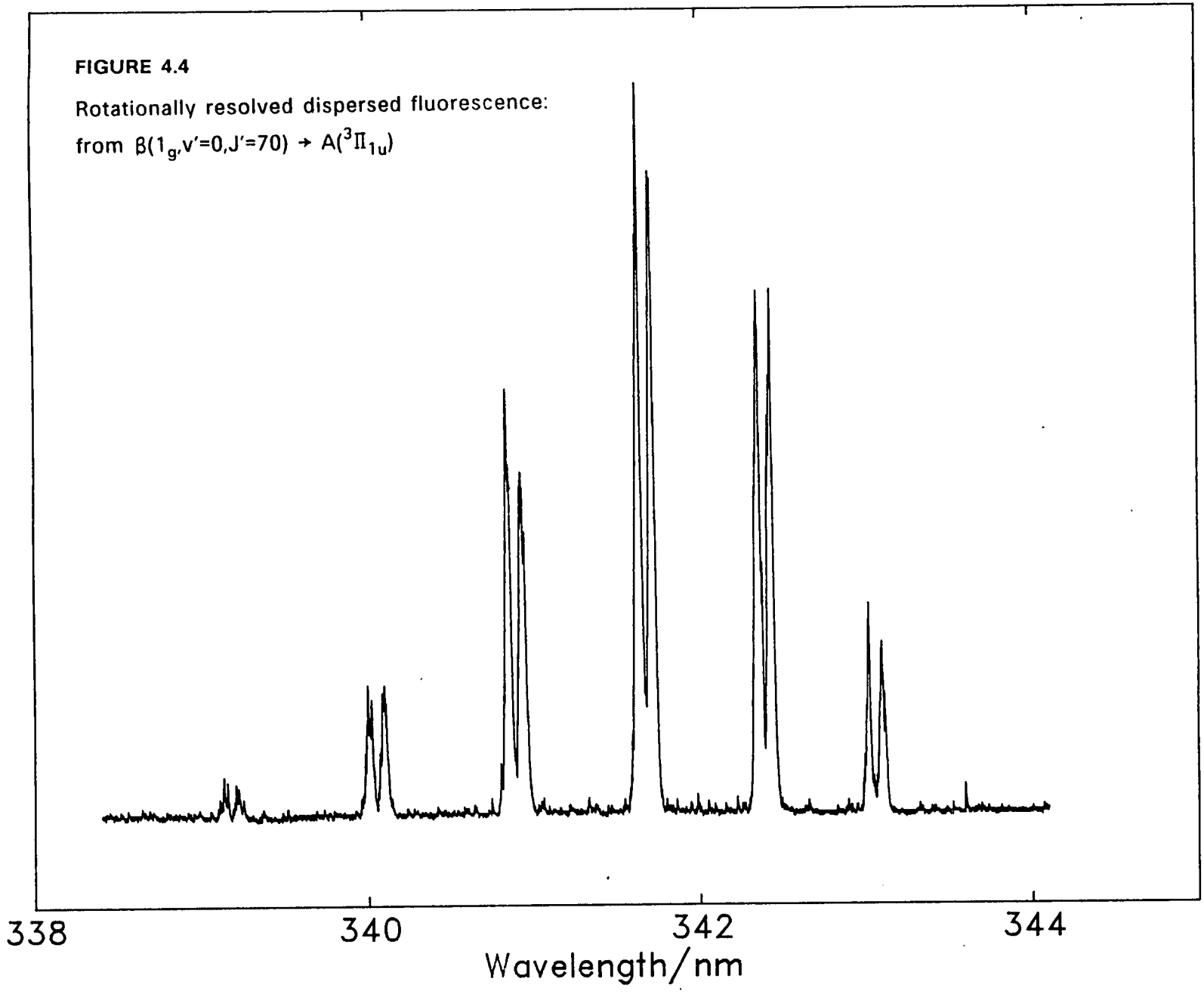

a high resolution scan over the $\beta(1_g) \rightarrow A$ system, clearly showing P and R branch rotational structure for each band, confirming the assignment of $\Delta\Omega=0$ for this transition.

A weak system is observed to the red of 351nm. This band consists of a single structureless peak when $\beta(1_g,v'=0)$ is excited, changing to two peaks following excitation of $\beta(1_g,v'=1)$ (see Fig 4.3). This reflection of the nodal properties of the β state vibrational wavefunction is confirmation that the $\beta(1_g)$ state is responsible for this emission. On energetic grounds it can be deduced that the terminus of this transition is a shallow bound state correlating with two ground state ($I^2P_{3/2}$) atoms. The lower state is assigned as the 0_u^- state which has been observed and characterised in emission from the $g(0_g^-)$ ion-pair state[10] (see 4.3.1 for details of simulations).

A broad system is observed close to 500nm. Again, the intensity envelope of this band, following excitation of the $v'=0$ and $v'=1$ levels, is a clear indication that it arises from fluorescent decay of the $\beta(1_g)$ state. This system is assigned as $\beta(1_g) \rightarrow 1_u$, where the lower state correlates with $I^2P_{3/2}$ and $^2P_{1/2}$.

4.3.1 Simulations

Simulations of the above three spectroscopic systems have been carried out using the RKR curve of Perrot et al. for the $\beta(1_g)$ state[9] (Figs 4.5 - 4.7).

The $\beta \rightarrow A$ system was simulated using the RKR curve of Viswanathan et al. for the $A(^3\Pi_{1u})$ state[7]. In order to correctly

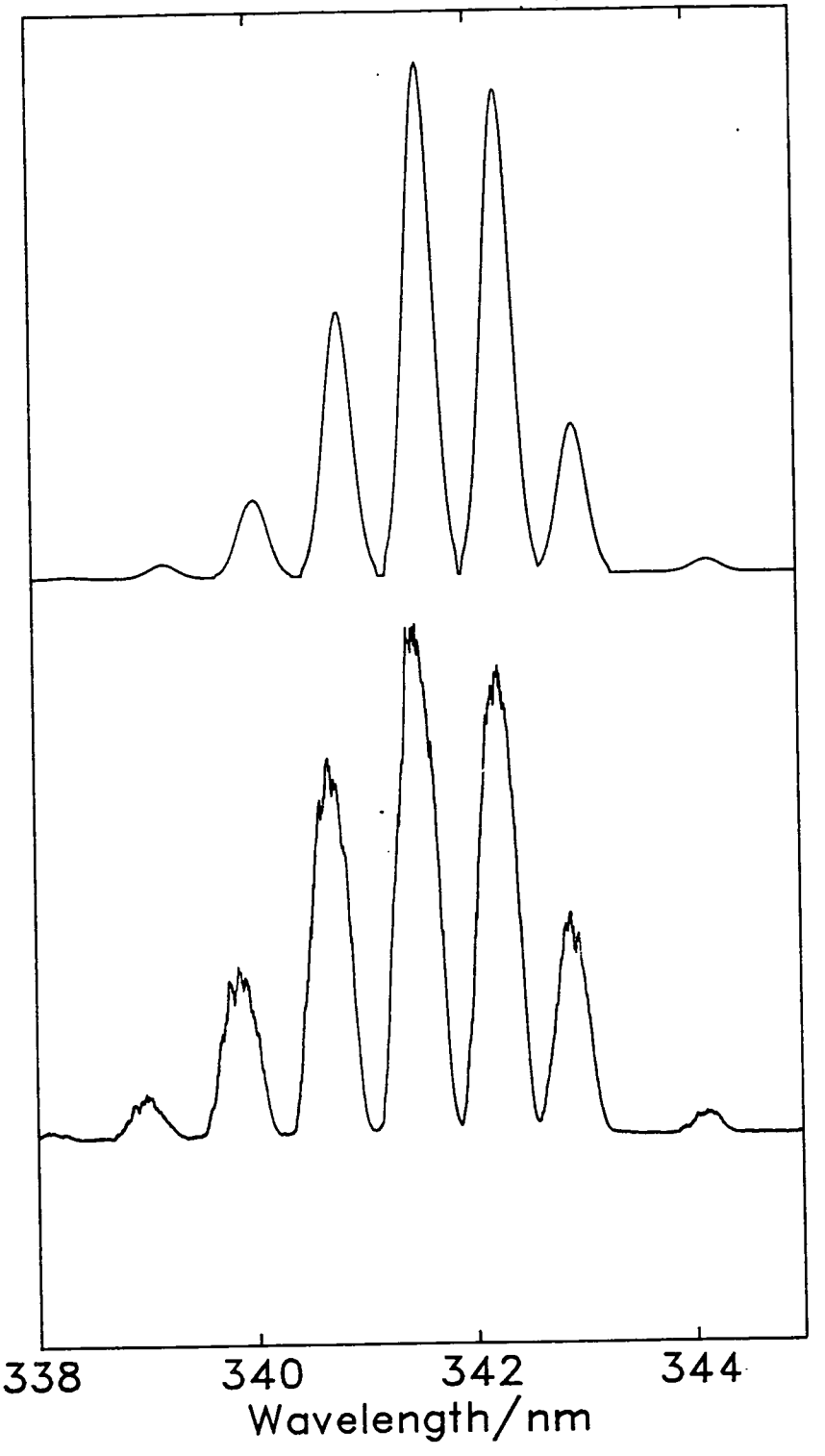

FIGURE 4.5

Experimental(lower) and simulated dispersed fluorescence:

$B(1_g, v'=0) \rightarrow A(^3\Pi_{1u})$

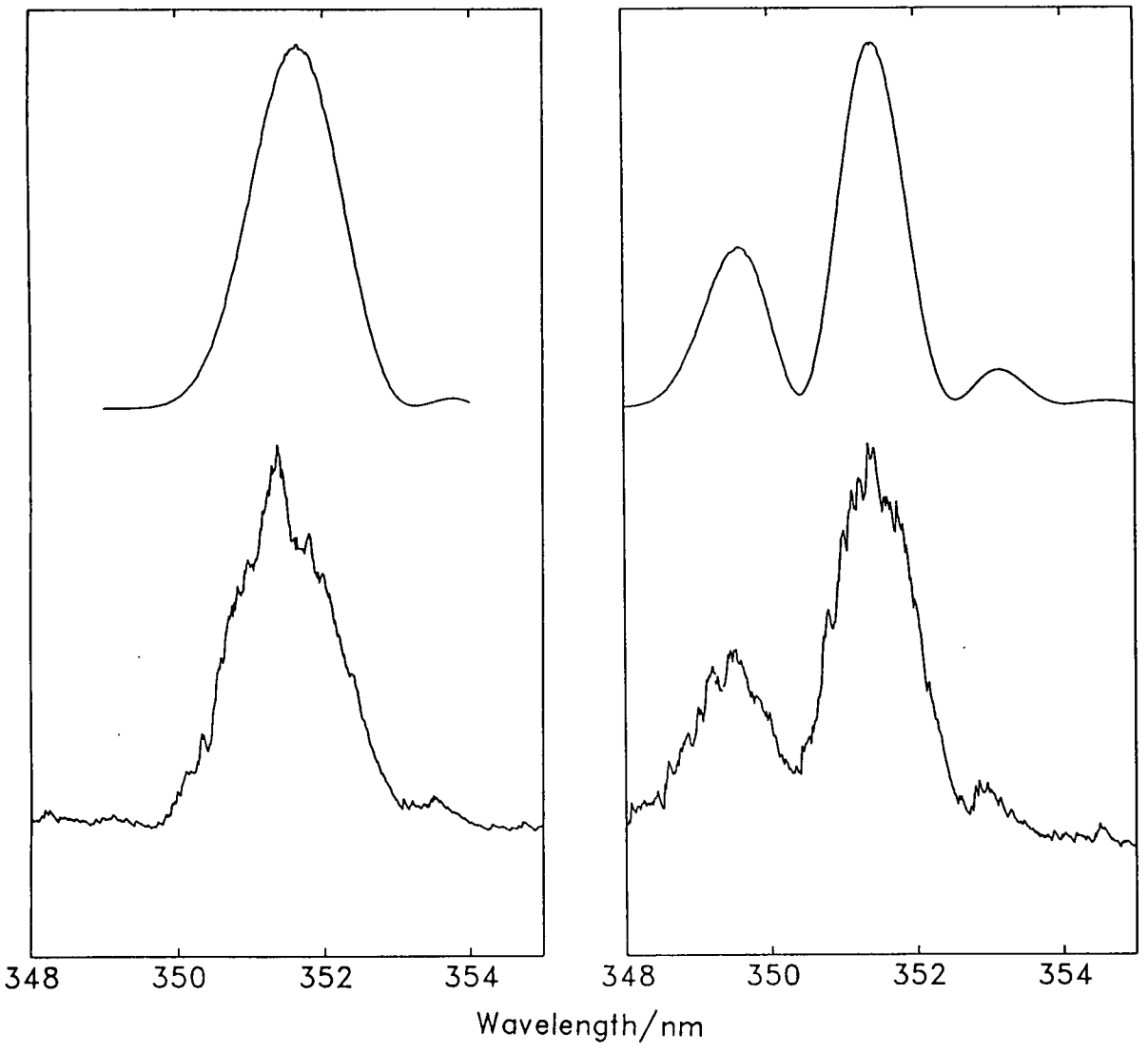

FIGURE 4.6

Experimental(lower) and simulated dispersed fluorescence:

$\beta(1_g, v'=0 \text{ and } 1) \rightarrow 0_u^-$

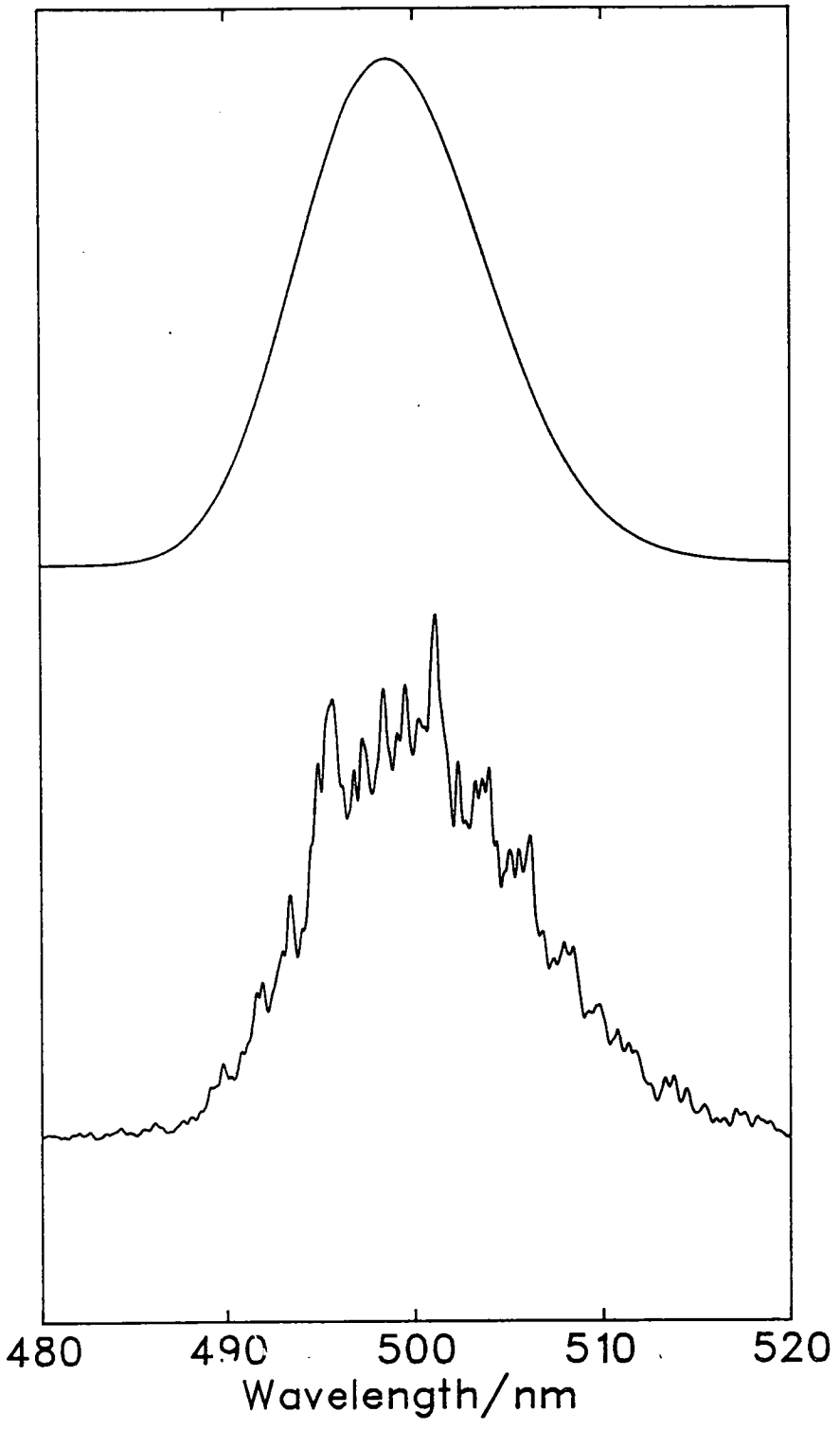

FIGURE 4.7

Experimental(lower) and simulated dispersed fluorescence:

$\beta(1_g, v'=0) \rightarrow 1_u$

reproduce the intensity envelope, the A state RKR curve was translated by +0.02Å. This is consistent with the margin of error introduced in the A state curve as a result of the poorly defined rotational parameters for this state.

Simulations of the 351nm system are shown in Fig 4.6. The potential curve for the lower state was constructed using the Morse parameters of Viswanathan and Tellinghuisen for the 0_u^- state, characterised in emission from the $g(0_g^-)$ state[10]. In order to match the positions of the peaks, it was neccessary to add $50cm^{-1}$ to the energy of the repulsive limb from v=3.2 - 3.7Å. This small shift is not unexpected as Viswanathan and Tellinghuisen were only able to specify the approximate vertical energy for this state. Emission to the $^1\Pi_{1u}$ state is also expected in this wavelength region. Simulations using the known curves for these two states indicate that emission to the $^1\Pi_{1u}$ state should occur ca. 3nm to the red of the $\beta \rightarrow 0_u^-$ system. As a result of the differing slopes of the $^1\Pi_{1u}$ and 0_u^- states, the peaks in the $\beta \rightarrow {}^1\Pi_{1u}$ system are also expected to have approximately twice the width of the corresponding $\beta \rightarrow 0_u^-$ peaks. However, as no such fluorescence is observed, it appears that the $\beta \rightarrow {}^1\Pi_{1u}$ transition is either forbidden or extremely weak. This apparent contradiction of the $\Delta\Omega=0$ propensity rule should provide an ideal example for testing the calculation of electronic transition strengths, using the separated-ion model.

Simulation of the 500nm system was carried out using Tellinghuisen's potential for the $^1\Pi_{1u}$ state [19], vertically translated to the second dissociation limit for I_2. A close match was achieved

by increasing V(r) by 340cm^{-1} in the region of r_e for the β state (3.6Å). A more detailed determination of the nature of the potential curve for the 1_u state would require analysis of dispersed fluorescence spectra from higher vibrational levels.

4.3.2 Quenching by Argon

Dispersed fluorescence emission spectra from I_2/Ar mixtures have been recorded for a range of Ar partial pressures (13, 25, 60, and 112 torr), following excitation of I_2 $\beta(1_g,v'=0)$. Fig. 4.8 shows the spectrum obtained at a pressure of 25 torr.

In presence of Ar, new bands are observed at 325, 368 and 461nm. Higher resolution dispersion of the 325nm band shows that this is predominantly emission from $D(0_u^+,v'=0)$ to $X(0_g^+)$. The system at 368nm can be assigned as $D(0_u^+) \rightarrow a'(0_g^+)$ (the $a'(0_g^+)$ state correlates with ground state $I^2P_{3/2}$ atoms). This transition has been previously observed following ArF laser excitation of high lying D state levels[11]. Using the potential curve of Lawley et al. for the a' state[11] and that of Ishiwata et al. for the D state[12], it is straightforward to show that fluorescence from $D(0_u^+,v'=0)$ to $a'(0_g^+)$ has peak intensity close to 368nm . The 461nm band is also assigned as a parallel transition from the $D(0_u^+)$ state, namely $D(0_u^+,v'=0) \rightarrow 0_g^+$. The lower state is expected to have a shallow bound potential energy curve lying close to the B state dissociation limit.

As the partial pressure of Ar is successively increased, the profile of the 341nm emission is observed to change. At low pressures (p < 25torr) ,$\beta(1_g) \rightarrow A(^3\Pi_{1u})$ is dominant, with $D'(2_g) \rightarrow A'(2_u)$ taking over

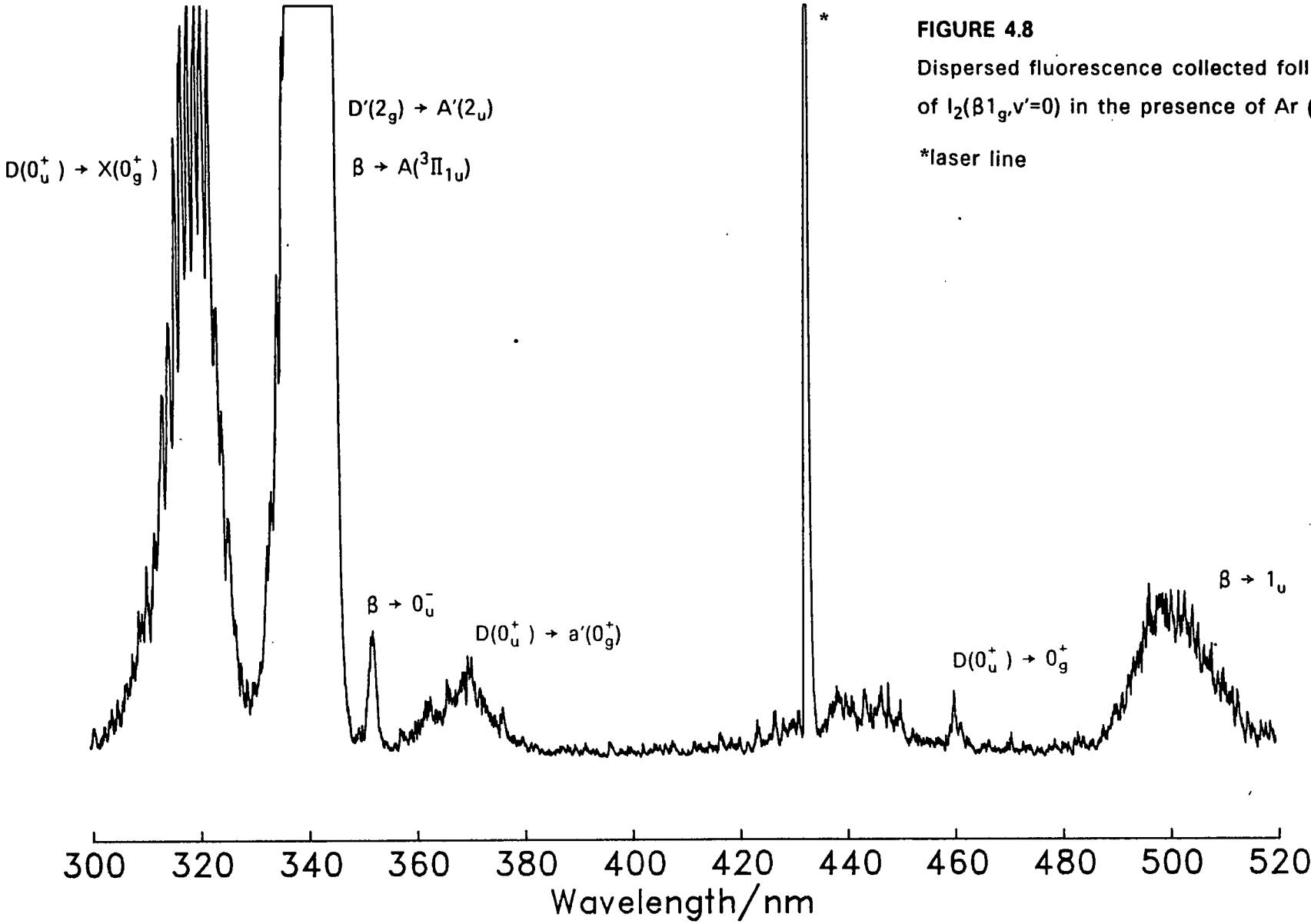

FIGURE 4.8

Dispersed fluorescence collected following excitation of $I_2(\beta 1_g, v'=0)$ in the presence of Ar (25 torr)

*laser line

at higher pressures. It appears that the distrubution amongst the vibrational states of $D'(2_g)$ is non-Boltzmann, even at an argon pressure of 112 torr.

There is a marked variation in the width and position of the 500nm system with pressure. It appears that a new system is growing in, centred on 505nm, as the pressure of Ar is increased. This band also becomes more intense with respect to the 351nm band as the quenching gas pressure is increased. It appears therefore that two ion-pair → valence transitions contribute to the emission around 500nm. It is already well known that for argon pressures greater than 200 torr, the 500nm system tracks in intensity with the $D'(2_g) \rightarrow A'(2_u)$ bands[13]. The second component of the 500nm band is therefore assigned to $D'(2_g) \rightarrow {}^3\Delta_{2u}$, as previously suggested by Hemmati and Collins [14]. As the pressure of Ar is increased the I_2 molecules will be more efficiently transferred from the $\beta(1_g)$ state to the lower $D'(2_g)$ state, resulting in the relative increase in intensity of the 500nm system with respect to that at 351nm. Tellinghuisen has already proposed that both the β and D' states contribute to fluorescence in the 342nm region[8], which is confirmed by the above observations. It is proposed that the broad system observed by Guy et al. and other workers at 505nm contains contributions from both these states.

4.4 Dispersed Fluorescence from $I_2(\gamma 1_u)$

The γ state of I_2 was first observed by King et al. in a double resonance fluorescence excitation experiment, by detecting broad-band fluorescence emission[15,16]. Chevaleyre et al. later identified this state as the 1_u ion-pair state correlating with $I^+(^3P_2)$ and $I^-(^1S_0)$ [17]. King et al. interpreted the excitation mechanism to involve the $B(0_u^+)$ state as the intermediate state and assigned gerade symmetry to the γ state. However, it is now thought that excitation of the $\gamma(1_u)$ state is facilitated by mixing of $B(0_u^+)$ with a nearby shallow bound 1_g state[17], resulting in the following excitation scheme:

$$\gamma(1_u) \leftarrow 1_g/B(0_u^+) \leftarrow X(0_g^+)$$

This hypothesis has been given credence by the observation of P and R branches in the fluorescence excitation spectrum obtained by scanning the second dye laser wavelength[16].

In order to identify the main fluorescent decay channels for the $I_2(\gamma 1_u)$ state, the following excitation scheme was used:

$$\gamma(1_u) \overset{2}{\nleftarrow} 1_g/B(0_u^+) \overset{1}{\downarrow} X(0_g^+)$$

1. (59–0) P(23)
2. (23–59)

The B ← X step reproduces the excitation route described by King et al[16]. The precise assignment of the second step is uncertain, as there is no information on the exact rovibronic level of the 1_g state involved.

Dispersed fluorescence from $\gamma(1_u, v'=23)$ is shown in Figures 4.9

and 4.10 . Two extensive oscillatory continua are observed and, in accordance with the $\Delta\Omega=0$ propensity rule, the lower states are assigned as having 1_g character.

4.4.1 The 350nm System: $\gamma(1_u) \rightarrow a(1_g)$

The system extending from 350 to 318nm can be assigned to $\gamma(1_u,v'=23) \rightarrow a(1_g)$. The shallow bound lower state has been characterised below the dissociation limit by Churassy et al. [18]. Tellinghuisen has derived the repulsive limb of the $a(1_g)$ state by matching the RKR curve of Churassy et al. with the potential curve of Dalby for the state which gives rise to electric-field-induced predissociation of the $B(0_u^+)$ state[19,20]. In order to produce a continuous curve, Tellinghuisen has adapted an avoided-crossing representation to smooth the connection of these potentials.

Simulations of the $\gamma \rightarrow a$ system were carried out using Tellinghuisen's potential for the a state and a Morse potential for the γ state based upon the vibrational constants of King et al. [16]. These simulations reproduce the bound-bound region satisfactorily, confirming the above spectroscopic assignment. However, the bound-free portion (in particular the wavelength of the red extremum) cannot be precisely simulated using Tellinghuisen's curve.

4.4.2 The 475nm System

The band system sxtending to the blue from 475nm is assigned as $\gamma(1_u,v'=23) \rightarrow (1_g; {}^2P_{3/2} + {}^2P_{1/2})$. The lower state is expected to be predominantly repulsive and the observed fluorescence transitions

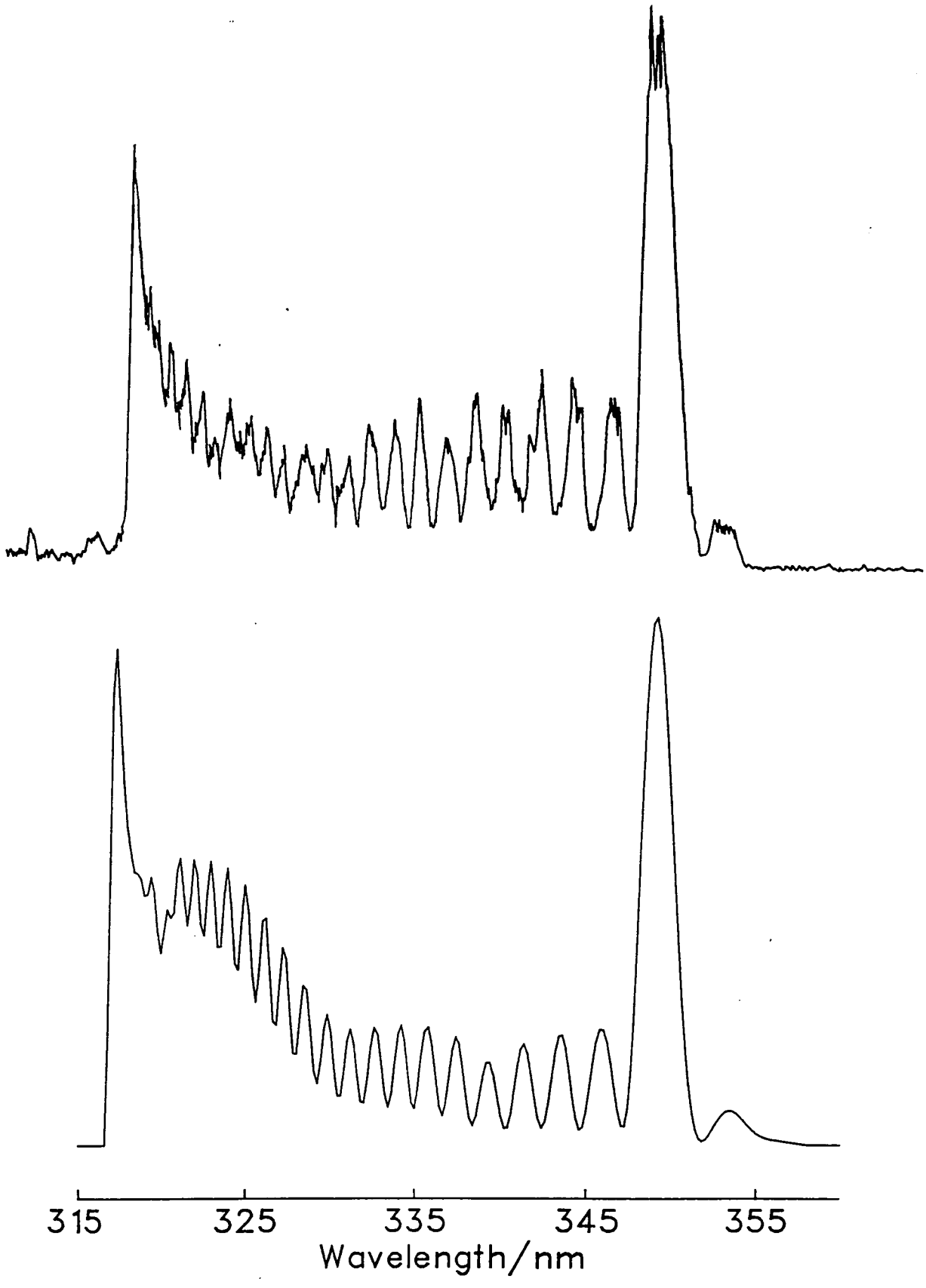

FIGURE 4.9

Experimental(upper) and simulated dispersed fluorescence:

$I_2(\gamma 1_u, v'=23) \rightarrow a(1_g)$

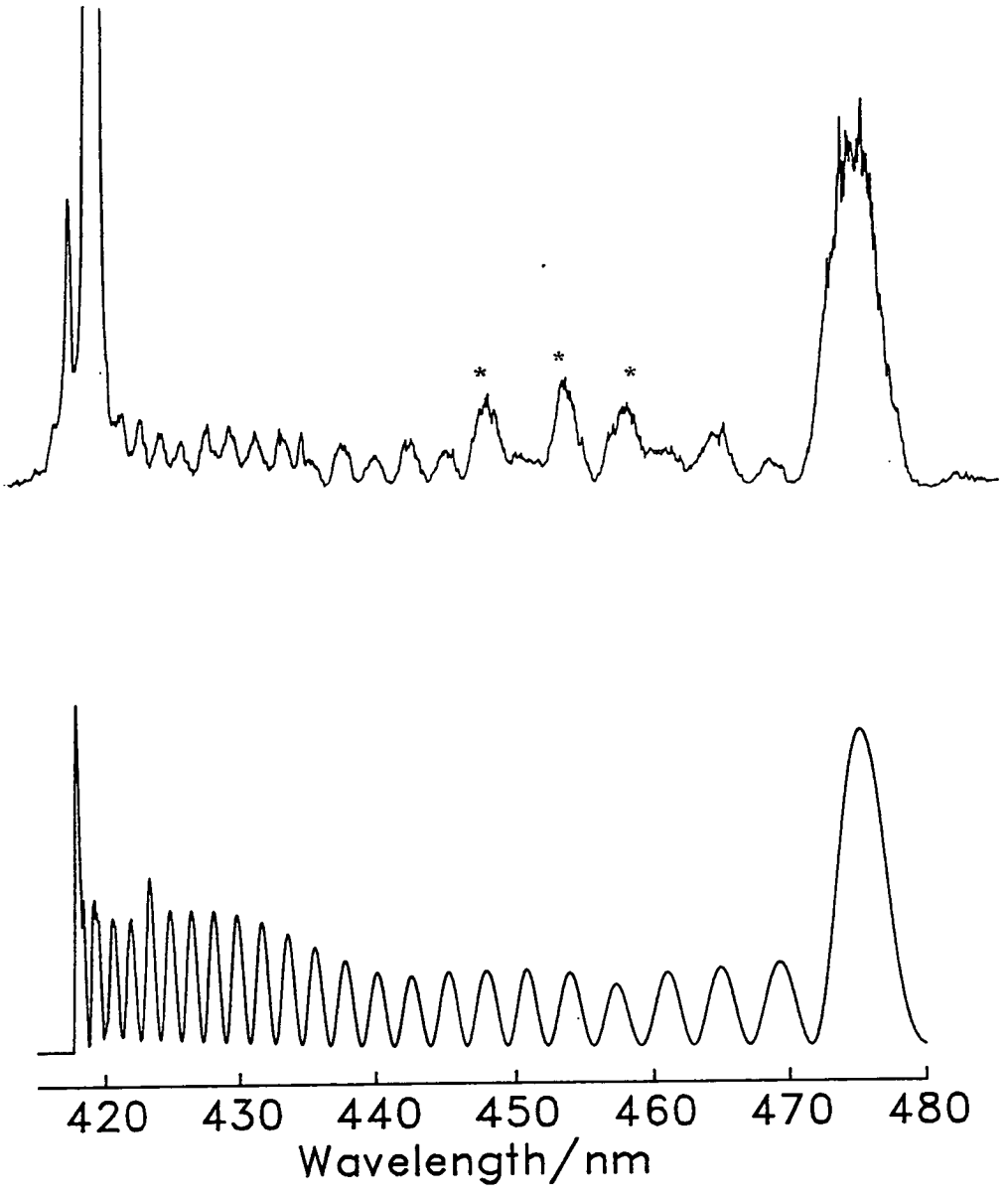

FIGURE 4.10

Experimental(upper) and simulated dispersed fluorescence:

$I_2(\gamma 1_u, v'=23) \rightarrow 1_g(3/2,1/2)$

terminate mostly in the continuum of the lower state. The dispersed fluorescence profile is rather similiar to that of the 350nm system. The simulation shown in Fig 4.10 employs a lower state potential with the same form as the $a(1_g)$ state (the whole curve being vertically translated to the second dissociation limit of I_2). In the absence of further dispersed fluorescence spectra the precise form of the bound well of the lower state cannot be precisely determined. However, the close matching of the simulated and experimental spectra indicates that the lower state is at least as deeply bound as the $a(1_g)$ state (ca. $300cm^{-1}$,[18]) and has a repulsive wall of similiar gradient.

The three features marked with asterisks in fig 4.10 are not reproduced in the simulation. These appear to terminate on another discrete lower state. There are two 1_g states correlating with $I\ ^2P_{3/2}$ and $^2P_{1/2}$ and thus two long wavelength systems are expected from the γ state on the basis of the $\Delta\Omega=0$ propensity rule. An exploratory simulation of these bands has shown that the three peaks marked with asterisks almost certainly arise from interference effects, indicating that the bound well for the lower state must be more extensively sampled than is the case for the 475nm system, with r_e translated by $-0.2Å$. The difference potential associated with the 475nm system is essentially monotonic, whilst that corresponding to the 460nm bands exhibits a maximum. To the blue of 460nm, the experimental spectrum will be a combination of these two systems.

It is interesting to note that as a consequence of the u→g parity selection rule and the inherent weakness of $\Delta\Omega=1$ transitions, the

fluorescence emission spectrum of the γ state is dominated by bound-free transitions. There are no deeply bound gerade states of I_2, correlating with either ground state or spin-orbit excited atoms which have Ω=1.

4.5 Reinterpretation of the emission spectrum of I_2 in Argon

The dispersed fluorescence emission spectrum of electronically excited I_2 in argon was first observed by Oldenberg in 1924, following absorption of ultraviolet atomic radiation[28]. A number of discrete spectroscopic systems were observed in the visible and UV regions and subsequently several attempts have been made to assign the features in the 200-500nm range, culminating in the comprehensive paper of Guy et al, in 1980[13]. This paper deals with the emission spectrum of I_2 in Ar, as excited by a Tesla discharge coil at temperatures of 360 and 810K with buffer gas pressures ranging from 200 to 750torr. Most of the prominent features were successfully assigned, but complete interpretation of the spectrum was hampered by a lack of information on the nature of fluorescence emission from certain ion-pair states of I_2 in the first manifold. A fuller analysis of this spectrum can now be carried cut as a result of the work described in sections 4.2 - 4.4.

Table 4.1 lists the main features observed by Guy et al., along with their assignments. In accordance with the propensity rule for ion-pair→valence transitions (see Chapter 1), all the strongest bands have been assigned as having $\Delta\Omega$=0. This table also lists proposed extensions to the original assignments, in light of the results

Table 4.1

Assignment of the emission spectrum of I_2 in Ar.

Wavelength(nm)	Assignment
505	$\beta(1_g) \rightarrow 1_u(ab)$ *
	$D'(2_g) \rightarrow {}^3\Delta_{2u}(ab)$
475	$\gamma(1_u) \rightarrow 1_g(ab)$ *
467	$\delta(2_u) \rightarrow 2_g(ab)$ *
461	$D(0_u^+) \rightarrow 0_g^+(ab)$ * $\gamma(1_u) \rightarrow 1_g(ab)$ *
430	$E(0_g^+) \rightarrow B(0_u^+)(ab)$
388	?
368	$D(0_u^+) \rightarrow a'(0_g^+)(ab)$ *
342	$D'(2_g) \rightarrow A'(2_u)(aa)$
	$\beta(1_g) \rightarrow A({}^3\Pi_{1u})(aa)$
326	$D(0_u^+) \rightarrow X(0_g^+)(aa)$
288	$g(0_g^-) \rightarrow 0_u^-(aa)$
277	$G(1_g) \rightarrow A({}^3\Pi_{1u})(aa)$
270	$F(0_u^+) \rightarrow X(0_g^+)(aa)$
238	$F'(0_u^+) \rightarrow X(0_g^+)(aa)$

ab: dissociation to $I(^2P_{1/2}) + I(^2P_{3/2})$
aa: dissociation to $I(^2P_{3/2}) + I(^2P_{3/2})$

*: proposed assignments

reported above.

Three unassigned peaks were observed at 461, 467 and 475nm[13]. This fluorescence was thought to originate from the lowest vibrational levels of three different ion-pair states located in the first ion-pair cluster of I_2, but no positive identification of the emitting states could be made. From the band profiles it was concluded that the lower states must possess shallow bound repulsive curves correlating diabatically with $I^2P_{3/2}$ and $^2P_{1/2}$.

Using the potentials derived from simulation of the $\gamma(1_u,v'=23) \rightarrow 1_g$ system (sec. 4.4.2), it can be shown that emission from the lowest vibrational levels of the γ state will give rise to a broad peak close to 475nm. It is therefore proposed that the 475nm peak in the quenched emission spectrum arises from the $\gamma(1_u) \rightarrow 1_g$ transition.

Emission at 461nm has been observed following collisional transfer into $D(0_u^+,v'=0)$ from the β state (sec 4.3.2) and assigned to the transition $D(0_u^+,v'=0) \rightarrow 0_g^+$. This band is similiar in nature to the 461nm band observed by Guy et al., with both upper and lower states fulfilling the criteria described above. Fluorescence from the $\gamma(1_u)$ state has also been observed around 460nm (section 4.2.2) . Therefore, it is proposed that the 461nm band reported by Guy et al. is assigned to $D(0_u^+) \rightarrow 0_g^+(^2P_{3/2} + {}^2P_{1/2})$, possibly with an additional contribution from $\gamma(1_u) \rightarrow 1_g$.

No emission peaking at 467nm has been observed directly in the experiments described in this chapter. However, an assignment of this band can be made, based on the assumption of Guy et al. that

three different ion-pair states of I_2 in the first cluster are responsible for the 461, 467 and 475nm bands[13]. Quenching of the $\beta(1_g)$ state (sec. 4.3.2) allows the main band systems originating from the $D'(2_g)$, $\beta(1_g)$ and $D(0_u^+)$ states to be identified. No emission is observed at 467nm from any of these states. The study of the spectroscopy of $E(0_g^+)$ also rules out this state, as no emission is observed in this region. There is no shallow bound 0_u^+ state correlating with the second dissociation limit of I_2 and hence no parallel transitions from the E state are expected to lie to the red of the E → B system at 430nm. $\gamma(1_u)$ can also be ruled out following assignment of the 475 and 460nm bands to this state. It is therefore proposed that the 467nm band must originate from the $\delta(2_u)$ state, which is expected to have a parallel transition $\delta(2_u) \rightarrow 2_g$ in this wavelength region.

The experiments reported above have not yielded an assignment for the 388nm band reported by Guy et al., indicating that the upper state must lie in a higher ion-pair cluster. The feature at 368nm can be attributed to the transition $D(0_u^+) \rightarrow a'(0_g^+)$, as described in sec. 4.3.2. The intense fluorescence observed by Guy et al. around 342nm, primarily $D'(2_g) \rightarrow A'(2_u)$, will almost certainly contain a contribution from the $\beta(1_g) \rightarrow A(^3\Pi_{1u})$ system; as postulated by Tellinghuisen in his detailed analysis of this band[8]. The emission observed by Guy et al. below 300nm, which was only tentatively assigned can now be accurately identified following recently reported work on the $G(1_g)$, $f(0_g^+)$ and $F'(0_u^+)$ ion-pair states[7,6,29]. These assignments are included in Table 4.1 for completeness.

4.6 The 505nm excimer band of I_2

There has been recent interest in the possibility of developing new, tunable, halogen lasers which operate in the visible and near-UV regions of the spectrum. Killeen and Eden have proposed that transitions between ion-pair and valence states of the halogens could provide the basis for a new family of excimer lasers and have demonstrated gain on the 505nm band of I_2, following electron-beam excitation of HI/rare gas mixtures at high buffer gas pressures ($4-6\times10^3$ torr) [21,22]. Ion-pair state formation in e-beam excitation of Br_2 has also been reported recently by the same group[23].

The I_2 laser, operating on the $D'(2_g) \rightarrow A'(2_u)$ (ion-pair to valence) bound-bound transition at 342nm, is well known. Ion-pair formation may be initiated by either electron-beam or optical excitation. The D' → A' band system has been characterised by Tellinghuisen[8] and the effect of the addition of foreign gases on emission intensities is well known[13]. The 505nm band has also been observed by several groups[13,14,24-26] and assigned by Hemmati and Collins[14] to the transition $D'(2_g) \rightarrow {}^3\Delta_{2u}$ (the ${}^3\Delta_{2u}$ state is repulsive, correlating to $I^2P_{3/2}$ and $^2P_{1/2}$). Guy et al. noted a slight variation in the pressure intensity dependence of the 342 and 505nm bands, but stated that this was within their experimental error and agreed with the spectroscopic assignment of Hemmati and Collins for the 505nm band[13]. Time-resolved studies by Killeen and Eden have shown that when ion-pair state formation occurs as a result of electron beam excitation of HI/argon mixtures, the fluorescence decay profiles for the 342nm and 505nm bands are clearly different[22].

From these studies it was concluded that the $D'(2_g)$ state is not responsible for the emission observed at 505nm.

As described in section 4.3, direct excitation of the $\beta(1_g)$ state under collision-free conditions gives rise to emission at 342nm ($\beta(1_g) \rightarrow A(^3\Pi_{1u})$) and 500nm ($\beta(1_g) \rightarrow 1_u$). Addition of Ar leads to additional contributions from $D'(2_g) \rightarrow A'(2_u)$ and $D'(2_g) \rightarrow {}^3\Delta_{2u}$ in the same spectral regions. Under these conditions, it would be expected that the 342 and 500nm bands would show similiar temporal decay profiles, apparently contradicting the results of the time-resolved studies of Killeen and Eden.

Killeen and Eden report that superfluorescence is observed to occur on the 342nm band, i.e. the gain coefficient for this transition is so great that amplification by stimulated emission occurs within the sample[21,22]. Under these circumstances, superfluorescence terminating on the A' state becomes the dominant loss mechanism for the D' state and as a result of this coherent phenomenon, the radiative lifetime of the D' state is shortened to 1.1ns from 6.8ns[21,27]. No emission will therefore be observed from the D' state at 505nm. Superfluorescence is much less likely to occur on the $\beta \rightarrow A$ transition as the molecules in the β state will be continually collisionally transferred into the superfluorescing D' state. However, spontaneous $\beta \rightarrow A$ fluorescence will occur at 342nm as well as $\beta \rightarrow 1_u$ emission at 505nm. Thus, the temporal decay profiles of the 342 and 505nm bands will be different. Under these circumstances the 342nm band is some six orders of magnitude stronger than the 505nm band. One puzzling point is that when the

partial pressure of HI is reduced to suppress superfluorescence on the D' → A' band, the two bands still have different temporal decay half-widths. It may be that the 505nm band has both β → 1_u and D' → 2_u components and a full double exponential fit of this decay is required rather than simple measurement of the half-width.

4.7 Summary

In conclusion, the spectroscopic studies reported in this chapter lead to a greater understanding of the emission spectrum of electronically excited I_2 in the presence of buffer gases.

The resolution of this long standing problem is not only of academic interest, but is also of relevance to the understanding of the kinetics of I_2 ion-pair → valence excimer transitions, upon which it is hoped to base a new visible excimer laser.

4.8 References

1. D.L. Rosseau and P.F. Williams, Phys. Rev. Lett. **33**, 1368 (1974)
2. J. Tellinghuisen, Phys. Rev. Lett. **34**, 1137 (1975)
3. J.C.D. Brand, A.R. Hoy, A.K. Kalkar and A.B. Yamashita, J. Mol. Spec. **95**, 350 (1982)
4. J.P. Perrot, B. Femelat, J.L. Subtil, M. Broyer and J. Chevaleyre, Mol. Phys. **61**, 85 (1987)
5. P. Luc, J. Mol. Spec. **80**, 50 (1980)
6. U. Heeman, H Knöckel and E. Tiemann Chem. Phys. Lett. **90**, 17 (1982)

7. K.S Viswanathan, A. Sur and J. Tellinghuisen, J. Mol. Spec. **86**, 393 (1981)
8. J. Tellinghuisen, J. Mol. Spec. **94**, 231 (1982)
9. J.P. Perrot, M. Broyer, J. Chevaleyre and B. Femelat, J. Mol. Spec. **98**, 161 (1983)
10. K.S. Viswanathan and J. Tellinghuisen, J. Mol. Spec. **101**, 285 (1983)
11. K.P. Lawley, M.A. MacDonald, R.J. Donovan and A. Kvaran, Chem. Phys. Lett. **92**, 322 (1982)
12. T. Ishiwata and I. Tanaka, Laser Chem. **7**, 79 (1987)
13. A.L. Guy, K.S. Viswanathan, A. Sur and J. Tellinghuisen, Chem. Phys. Lett. **73**, 582 (1980)
14. H. Hemmati and G.J. Collins, Chem. Phys. Lett. **67**, 5 (1979)
15. M.D. Danyluk and G.W. King, Chem. Phys. **22**, 59 (1977)
16. G.W. King, I.M. Littlewood and J.R. Robins, Chem. Phys. **56**, 145 (1981)
17. J. Chevaleyre, J.P. Perrot, J.M. Chastan, S. Valignat and M. Broyer, Chem. Phys. **67**, 59 (1982)
18. S. Churassy, F. Martin, R. Bacis, J. Vergès and R.W. Field, J. Chem. Phys. **75**, 10 (1981)
19. J. Tellinghuisen, J. Chem. Phys. **82**, 4012 (1985)
20. F.W. Dalby, C.P.D. Levy and J. Vanderlinde, Chem. Phys. **85**, 23 (1984)
21. K.P. Killeen and J.G. Eden, Appl. Phys. Lett. **43**, 539 (1983)
22. K.P. Killeen and J.G. Eden, J. Opt. Soc. Am. B **2**, 430 (1985)
23. D.C. Shannon, K.P. Killeen and J.G. Eden, J. Chem. Phys. **88**, 1719 (1988)
24. V.N. Baboshin, L.D. Mikheev, A.B. Pavlov, V.P. Fokanov,

M.A. Khodakorskii and A.P. Shirokikh, Sov. J. Quantum. Electron. **11**, 683 (1981)

25. M.J. Shaw, C.B. Edwards, F. O'Neill, C. Fotakis and R.J. Donovan, Appl. Phys. Lett. **37**, 346 (1980)
26. M. Martin, C. Fotakis, R.J. Donovan and M.J. Shaw, Nuovo Cim. **63**, 300 (1981)
27. M.C. Sauer, N.A. Mulac, R. Cooper and F. Grieser, J. Chem. Phys. **64**, 4587 (1976)
28. O. Oldenberg, Z. Physik **25**, 136 (1924)
29. T. Ishiwata, A. Tokunaga, T. Shinzawa and I. Tanaka, J. Mol. Spec. **117**, 89 (1986)

Chapter 5
MEASUREMENT OF THE VIBRONIC EXCITATION FUNCTION AND RATE CONSTANTS FOR REACTION BETWEEN $I_2(f0_g^+, v'=n)$ AND Xe

5.1 Introduction

The results of a laser optical-optical double resonance study of the chemical reaction:

$$I_2(f0_g^+, v'=n) + Xe \rightarrow XeI(B^2\Sigma_{1/2}) + I(^2P_{3/2})$$

$$n=50 \rightarrow 107$$

are presented and discussed in this chapter. Firstly, however, it is useful to consider the aims and objectives of this work against the the background of studies of similiar systems reported in the literature.

5.2 Reactions of noble gas atoms with halogen and interhalogen diatomic molecules

The pioneering work of Golde, Setser and their co-workers in the 1970's on the reactions of rare gas atoms with halogen containing molecules opened up new opportunities for the detailed study of rare-gas monohalide formation [1,2]. These transient chemical species, which are only signficantly bound in electronically excited states, play an important role as the lasing media in high power UV excimer gas lasers. In these laser systems, the rare gas monohalide molecules RgX^* (Rg = rare gas atom, X = halogen), are generally produced in electrical discharges. The kinetics of excimer formation under these conditions are extremely complicated and in order to gain a partial understanding of the key processes involved it is important to study model reactions under well defined conditions, where the energy available in the entrance channel has been predetermined. The first studies to successfully achieve this involved

the use of flowing afterglow methods to electronically excite Rg metastable states and to monitor the subsequent reaction with halogen containing compounds, by collecting and dispersing chemiluminescence from RgX^* products.

$$Rg(^3P) + RX \rightarrow RgX^*(B,C,D) + R \rightarrow Rg + X + h\nu + R$$

The ground states of rare gas monohalides are essentially repulsive and hence the observed product chemiluminescence is bound–free in nature. This bound–free emission provides the basis for the operation of a wide range of rare–gas halide excimer systems. Analysis of this fluorescence allows product state vibrational distributions to be determined, as well as branching ratios, for reactive and purely physical quenching of Rg^* by halogen containing compounds. It has been observed that physical quenching is more important when polyatomic halide precursors are used. In these cases, as the complexity of the collision partner increases, so does the number of non–reactive exit channels available to soak up excess energy.

5.2.1 Comparison with the alkali metals

Armed with the knowledge that the entrance channel properties for these processes strongly resemble those for reactions of ground state alkali metal atoms with rare gases, Setser and co–workers were able to draw close analogies between these two classes of reaction [2]. The cross–sections for reactions involving rare–gas metastables closely match those involving the alkali metal atoms and are generally greater than $100Å^2$. These large cross–sections are attributed to a harpooning, curve–crossing mechanism occurring at

large internuclear distances, as first described by Polanyi in 1932 [3] and developed by Magee in 1940 [4]. The crossing is that from the $Rg-X_2$ potential to the $Rg^+-X_2^-$ ionic surface and is facile for partners with low ionisation potentials and large electron affinities respectively [4]. The ionization potentials for Rg $^*(^3P_2)$ metastable atoms and ground state alkali metal atoms are almost identical [2]. Inelastic scattering studies have also shown that the long range parts of the Rg^*-X_2 and alkali-X_2 potential curves show similiar behaviour [5]. The possibility of varying degrees of spin-orbit excitation in the Rg^*/X_2 entrance channel is one important difference between the two types of reaction.

5.2.2 Experimental Techniques

This work inspired new experimental activity mainly aimed at unravelling the complicated reaction dynamics of these processes. These reactions may involve one or more curve-crossing and recrossing steps before emerging onto the appropriate ionic surface leading to the observed excimer product formation. The new techniques which have been developed to study these reactions are all based on the observation of product state chemiluminescence. RgX^* fluorescence originates from an electronically excited, bound ion-pair state and terminates on one of the spin-orbit components correlating with ground state rare gas and halogen atoms [6-9]. Thus, the radiative decay from the upper state is bound-free in nature, terminating on a repulsive state. There is now sufficient, precise information available on these potential curves to allow product state vibrational distributions to be determined by inversion

techniques [10]. Such analysis is only useful, however, where the fluorescence has been collected under "nascent", collision-free conditions; generally at total pressures of less than 1 torr. This is particularly important for the determination of product state branching ratios where the radiative lifetimes of the product states involved may vary by up to an order of magnitude.

The wide range of techniques developed to probe these reactions in greater detail can be grouped together according to the information derived from a particular technique [11]:

(a) Observation of chemiluminescence emission and excitation ("action") spectra following laser excitation of "collision pairs" or jet-cooled van der Waals complexes [12-16]. This restricts the impact parameter and/or precursor geometry for reaction. The available energy can be controlled by using a tunable laser excitation source.

(b) Use of ultraviolet radiation sources to excite ion-pair states of the halogen partners; exploiting the wide range of molecular states available above reaction threshold [17-26]. This is potentially a highly efficient source of excitation as the excess energy in the entrance and exit channels is of the same form - namely, molecular vibronic energy.

(c) Reactions carried out by reacting laser-aligned, ground state halogen molecules (eg. IBr) with rare-gas metastable beams. This gives information on the importance of approach geometry or the "steric factor" [27].

(d) Beam–gas studies of translationally hot rare–gas metastables in collision with thermal ground state halogen molecules [28,29]. Dispersed chemiluminescence is collected under single collision conditions, allowing determination of nascent product state distributions, giving information on branching ratios for the available excited channels. These studies have recently been extended to yield information on average product state rotational alignments [11].

The work presented in this chapter falls in category (b). However, as many studies in category (a) involve excitation of molecular states it is valuable to consider both of these techniques in more detail.

5.2.3 Reactions of electronically excited halogens

Setser et al. have observed direct excitation of transient van der Waals bound "collision pairs" in two–photon laser excitation of Xe/Cl_2, ICl and CCl_4 mixtures [13]. Chemiluminescence from highly vibrationally excited $XeCl^*$ ($B^2\Sigma_{1/2}$) is observed, indicating that the $Xe^+–Cl^-$ surface forms the exit channel. The following mechanism has been proposed to explain the experimental results:

$$"Xe–Cl_2" \rightarrow Xe^+Cl_2^- \rightarrow XeCl^*(B) + Cl$$

A separate study of the Xe+Cl atomic photo–association reaction rules out dissociation of Cl_2 followed by photo–association as the mechanism for reaction. Contributions from Xe^*, Xe_2^* and Cl_2^* electronically excited states which could subsequently react to give XeCl(B) are ruled out on the grounds that the time profile for chemiluminescence shows a prompt risetime in contrast with the Xe^*

($^3P_2$) + Cl_2 reaction. Hence, Setser et al. have concluded that direct excitation onto the ionic surface is taking place via two photon absorption. As the two potential curves involved have different slopes, the excitation wavelength determines the atom-molecule distance at which electron transfer occurs, in accordance with the Franck-Condon principle. Thus, the entrance channel geometry is well defined with r=4-5Å for the single photon wavelength range 300-330nm.

Boiveneau and co-workers have successfully observed rare-gas halide chemiluminescence following two photon laser excitation of jet-cooled Van der Waals species [14-16]. The weakly bound complexes were prepared in a supersonic nozzle expansion using seeded Xe/Br_2 and Xe/Cl_2 mixtures. Detailed information on the dynamics of these complex photochemical systems has been obtained. The study of the chemical reaction

$$(Xe\text{-}Cl_2)^* \rightarrow XeCl^* + Cl$$

by Boiveneau et al. highlights the value of this technique [14]. State-selected chemiluminescence excitation spectra were obtained as a function of laser wavelength by collecting fluorescence at 308 and 345nm, probing the B and C states of XeCl respectively. The form of these excitation or action spectra is accounted for by invoking two separate excitation routes. Both of these involve pumping of the final state via a repulsive intermediate state, $Xe\text{-}Cl_2(^1\Pi_{1u})$. This state is strongly coupled to the $Xe^+Cl_2^-$ ionic surface and direct formation of XeCl(B,C) states is expected to occur. There are no discrete resonances in the exit channel and

hence the "action" spectrum for XeCl formation obtained by this process is expected to be continuous. This is observed for the XeCl(C) state excitation spectrum. However, there is discrete vibrational structure in the XeCl(B) excitation spectrum. This is attributed to a second pathway, where $Xe-Cl_2(^1\Pi_u)$ rearranges to $Xe^+Cl^-(X)-Cl$, prior to absorption of the second photon. The structure on the B state excitation spectrum is assigned to excitation of discrete vibrational levels of Xe^+Cl^- $(B^2\Sigma_{1/2})$ from the ground state. No $XeCl(C^2\Pi_{3/2})$ state is formed via this pathway as this would require rearrangement to $Xe^+Cl^-(A^2\Pi_{3/2})-Cl$ followed by excitation to the C state at energies outside those covered by the experimental action spectrum.

An important dynamical result obtained by limiting the geometry of the precursor complex is that the excimer product is observed to be vibrationally cold [15]. This can be explained by considering the nature of the $Xe^+Cl_2^-$ potential energy surface. The geometry of the complex is frozen with r(Xe-Cl)=3.3Å, resulting in electron transfer at much closer range than in the thermal collision experiment (harpooning at ca.5Å). The consequence of sampling this region of the $Xe^+Cl_2^-$ potential surface is that the excess energy is transferred into translational energy of the recoiling Cl atom rather than into product internal energy. No chemiluminescence has been observed following excitation of $Xe-I_2$. In this case there is strong coupling to repulsive states which can interact with the ionic surface at short distances. No quantitative information on the effect of increasing reactant internal energy on $XeCl^*$ excimer yield is available. The yield of $XeCl^*$ was monitored as a function of excitation wavelength.

However, these yields are not normalised to the cross-sections for absorption into the precursor states.

Use of techniques which exploit the molecular excitation channel is now widespread. These include excitation by synchrotron radiation (SR), spectrofluorimeters and coherent laser radiation. Synchrotron electron storage rings are efficient sources of pulsed, tunable UV and VUV radiation. These sources are particularly suitable for time and wavelength resolved spectroscopic studies and by using SR, Donovan and co-workers have been able to elucidate the salient features of the reactions of Xe with ICl($E0^+$) and IBr($E0^+$) [22,11]. A complementary study of the reaction of Xe with $I_2(D0_u^+)$ has also been carried out using a spectrofluorimeter [21]. The general strategy is to excite a molecular ion-pair state by single photon absorption in the UV region and to disperse the chemiluminescence arising as a consequence of the reaction:

$$Xe + XY^* (E/D) \rightarrow XeX^*(B,C) + Y$$

It has been shown that the onset of reaction under thermal conditions is close to that predicted thermochemically, implying that there is no significant barrier to reaction [21,22]. The thermochemical threshold is estimated by evaluating the energy required to break the X-Y bond and form XeX in the appropriate excited state. The yield of excimer product has also been determined as a function of excitation wavelength and in the case of Xe/IBr($E0^+$), an excitation function, corrected for absorption cross-section has been obtained [11]. Reactions involving interhalogens give the possibility of two chemical products. The branching ratio for XeI and

XeBr formation as a function of excitation wavelength has been determined for Xe/IBr($E0^+$) [11]. These studies were limited by the bandwidth of the synchrotron radiation levels for a given SR excitation wavelength. However, Donovan and co-workers have minimised this problem by carrying out extensive spectroscopic studies of the ion-pair states involved in reaction. Bibinov and co-workers have also used vacuum UV radiation to study the reactions of excited halogen molecules, although their fluorescence spectra generally show lower resolution than those collected at Daresbury by Donovan et al [25].

Zimmerer et al. have used synchrotron radiation to study Rg+Cl_2^*, where Rg=Kr, Ar and Xe [18,19]. Although much of this work has concentrated on measuring kinetic parameters for the relaxation of $RgCl^*$ by Rg, the relative efficiency of $ArCl^*$ formation has been determined as a function of vibrational quanta in the Cl_2 ion-pair state . The yields of $ArCl^*$ from individual vibronic levels have been normalised to the known absorption cross-sections for Cl_2, and are observed to increase with increasing vibrational quantum number in the range v'=0 to 4. These vibrational levels are supported in a Rydberg-type minimum in the double well potential arising from the interaction of a Cl_2 Rydberg state and ion-pair state which correlates adiabatically with $Cl^+(^1S)$ and $Cl^-(^1S)$.

Ehrlich and Osgood have reported observation of XeBr($B^2\Sigma_{1/2}$) following two photon excitation into $Br_2(D'2_g)$ [17]. It appears from the experimental dispersed fluorescence spectra that extensive relaxation of the intermediate states is occuring at the high

pressures used (up to pXe=600torr).This will almost certainly result in excitation of a range of ion-pair vibrational states. However, a rate constant for formation of $XeBr^*$ has been obtained , although collisional relaxation in the intermediate state means that the total excitation energy supplied is not well determined.

An optical-optical double resonance study of the reaction:

$$Cl_2^*(^1\Sigma_u^+, v'=0, J'=10) + Xe \rightarrow XeCl^* + Cl$$

has been carried out by Ishiwata et al. [26]. Pumping of the $Cl_2^*(^1\Sigma_u^+)$ ion-pair state was achieved by exciting a Xe/Cl_2 mixture with single laser pulses at 19924.7cm^{-1}. This gives one photon resonant, three photon excitation of the $^1\Sigma_u^+$ state via an accidental resonance with v'=12 in the $B(0_u^+)$ intermediate state. Dispersing emission from the excited mixture shows the presence of $XeCl^*(B,C)$ along with the fluorescence from the $Cl_2(^1\Sigma_u^+)$ ion-pair state. Dispersed fluorescence was collected for a range of Xe partial pressures (1-100 torr) and application of a time-inte grated kinetic analysis gave a reaction rate constant of $3.0\pm0.5\times10^{-10}cm^3molecule^{-1}s^{-1}$.

5.2.4 Objectives

"Accidental", one colour double resonance fails to exploit the inherent advantages of the OODR technique. Two colour experiments with tunable dye lasers allow the preparation of a wide range of reactant states in the entrance channel, enabling detailed studies of these reactions to be carried out. The aims of the work described in this chapter were as follows:

(1) Achieve excitation of the $f(0_g^+)$ state of I_2 using two-colour OODR and establish if reaction occurs with Xe. Donovan and O'Grady have shown that reaction occurs following excitation of $I_2(D0_u^+)$ [21]. Extending this work should provide information on the importance of the electronic identity of the reacting ion-pair state.

(2) Monitor the yield of XeI^* as a function of vibrational quantum number in the $f(0_g^+)$ state, thus obtaining an excitation function for XeI^* production normalised to the efficiency of absorption into the ion-pair state.

(3) Measure state-specific (single rovibronic level) rate constants for chemical and physical quenching of $I_2(f0_g^+)$ by Xe.

Some of the studies reviewed above have achieved these objectives in part for related Rg/X_2^* systems [11,18]. Use of the OODR technique with two tunable dye lasers has allowed the above objectives listed above to be realised, resulting in a detailed study of the $Xe/I_2(f0_g^+)$ system. Interpretation of the dispersed fluorescence spectra obtained was greatly facilitated following the detailed spectroscopic and quenching studies described in Chapter 3.

5.3 Experimental Details

The pulsed output from a high power excimer laser (Lambda Physik EMG 201 MSC), operating on the 308nm XeCl(B-X) lasing transition was used to simultaneously pump two dye lasers. The first dye laser (Lambda Physik FL3002E), operating with Rhodamine 6G dye solution as the lasing medium, was used to selectively excite

single rovibronic levels of the $B(0_u^+)$ state of I_2. The second dye laser was used , in conjunction with second harmonic generating techniques, to pump molecules excited by the first laser from the B state to the $f(0_g^+)$ ion-pair state. Spectrosopic grade Xe (99.9%,BDH) was introduced to the reaction cell from an external gas handling line. At higher pressures of Xe (>5 torr), Xe/I_2 samples were pre-mixed in a sealed bulb before introduction to the cell. A purified sample of I_2 was contained in a side arm adjacent to the cell. Fluorescence was collected at right angles to the incident laser beams and dispersed using a high resolution monochromator (Jobin-Yvon HRS2; 0.6m.) Dispersed fluorescence at the exit slit of the monochromator was detected by a photomultiplier (Hammamatsu R928) and the signal relayed to a boxcar integrator (Stanford Research Systems; SR250). The output from the boxcar was relayed directly to a chart recorder (Kipp and Zonen). A full description of the experimental set up is given in Chapter 2.

5.4 Results

5.4.1 Excitation of $I_2(f0_g^+)$

The reaction of $I_2(f0_g^+)$ and Xe has been studied over the range v'=0 to 107. Excitation of the $f(0_g^+)$ state was achieved by use of the OODR technique. The molecules were first pumped to the intermediate B state using a narrow bandwidth,tunable laser locked to the transition:

$$B(0_u^+) \leftarrow X(0_g^+) \quad (17-1)\ P(70)$$

Care was taken to select a transition which resulted in excitation of

a single rovibronic level of the B state. The number of excited states which may be accessed from this level are then limited by the selection rules governing the absorption of radiation:

$$\Delta\Omega=0,\pm1,\ \Delta v=n,\ \Delta J=\pm1$$

Thus, the f state could be prepared in only two rotational states for a given intermediate level. The probe laser bandwidth ($0.2cm^{-1}$) was sufficiently narrow to resolve the P and R branch transitions in excitation, permitting pumping of a single rovibronic level in the upper state. This allowed a fully state-selected dynamical study to be carried out on the $f(0_g^+)$ ion pair state of I_2. The advantages of the OODR technique in allowing excitation of ion-pair state vibronic levels which lie outside the Franck-Condon region for the ground state of I_2 are described in Chapter 1. All spectroscopic assignments were carried out using the well known, calibrated B → X absorption spectrum of I_2 and the available molecular constants for the B and f states [30-32]. Confirmation of these assignments was given by simulation of dispersed fluorescence spectra from the f state, described in Chapter 3.

5.4.2 Physical Quenching of I_2 by Xe

Below reaction threshold the addition of Xe results in collisional quenching of the $I_2(f0_g^+)$ state. By dispersing fluorescence emission from Xe/I_2 mixtures excited below threshold the main radiative decay channel can be identified as electronic quenching. Inter ion-pair state energy transfer occurs in the presence of Xe and new band systems are observed at 270,325,340 and 425nm. Following the study of the emission spectrum of I_2 in Ar, excited by Tesla

discharge, these can be assigned to the F, D, D' and E ion-pair states of I_2 respectively [33]. As the Xe pressure is increased the 340nm $D'(2_g) \rightarrow A'(2_u)$ band system increases in intensity. This phenomenon results from successive collisional transfer steps resulting in transfer to the lowest lying ion-pair state of I_2 (i.e. the $D'(2_g)$ state). One consequence of studying physical quenching processes by monitoring dispersed fluorescence is that no information can be directly obtained as to the nature of "dark" decay channels.

5.4.3 Chemical quenching with Xe

Addition of Xe efficiently quenches fluorescence from $I_2(f0_g^+)$ and for excitation above v'=52, a new emission system appears around 253nm (see Figure 5.1). This fluorescence is readily assigned as XeI (B → X), the excited XeI being formed in the reaction:

$$I_2(f0_g^+) + Xe \rightarrow XeI(B) + I(^2P_{3/2})$$

Increasing the partial pressure of Xe results in an increase in XeI emission intensity and further loss of I_2 emission (see Figure 5.2). XeI formation is only observed to occur when the second dye laser is tuned to an ion-pair state resonance. This rules out the possibility of XeI formation via the excitation of "collision pairs", as described in Setser and Ku [13]. In order to determine the vibronic threshold for this reaction, the intensity of chemiluminescence from XeI was monitored as a function of vibrational level in the f state. The Franck-Condon factors for ion-pair state excitation vary substantially from level to level. To normalise for this the intensity of XeI chemiluminescence was ratioed against the intensity of fluorescence

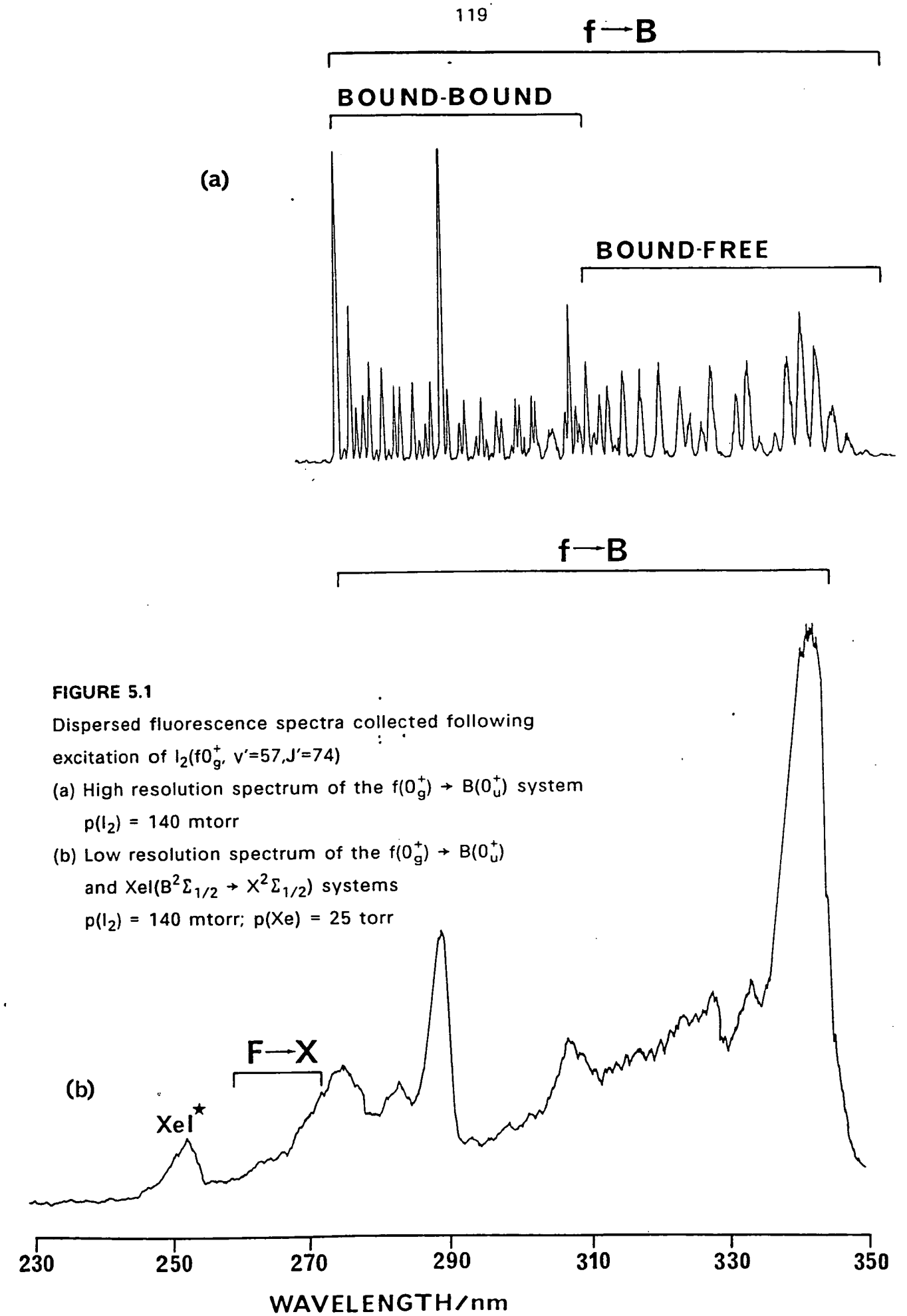

FIGURE 5.1

Dispersed fluorescence spectra collected following excitation of $I_2(f0_g^+, v'=57, J'=74)$

(a) High resolution spectrum of the $f(0_g^+) \rightarrow B(0_u^+)$ system
$p(I_2)$ = 140 mtorr

(b) Low resolution spectrum of the $f(0_g^+) \rightarrow B(0_u^+)$ and $XeI(B^2\Sigma_{1/2} \rightarrow X^2\Sigma_{1/2})$ systems
$p(I_2)$ = 140 mtorr; p(Xe) = 25 torr

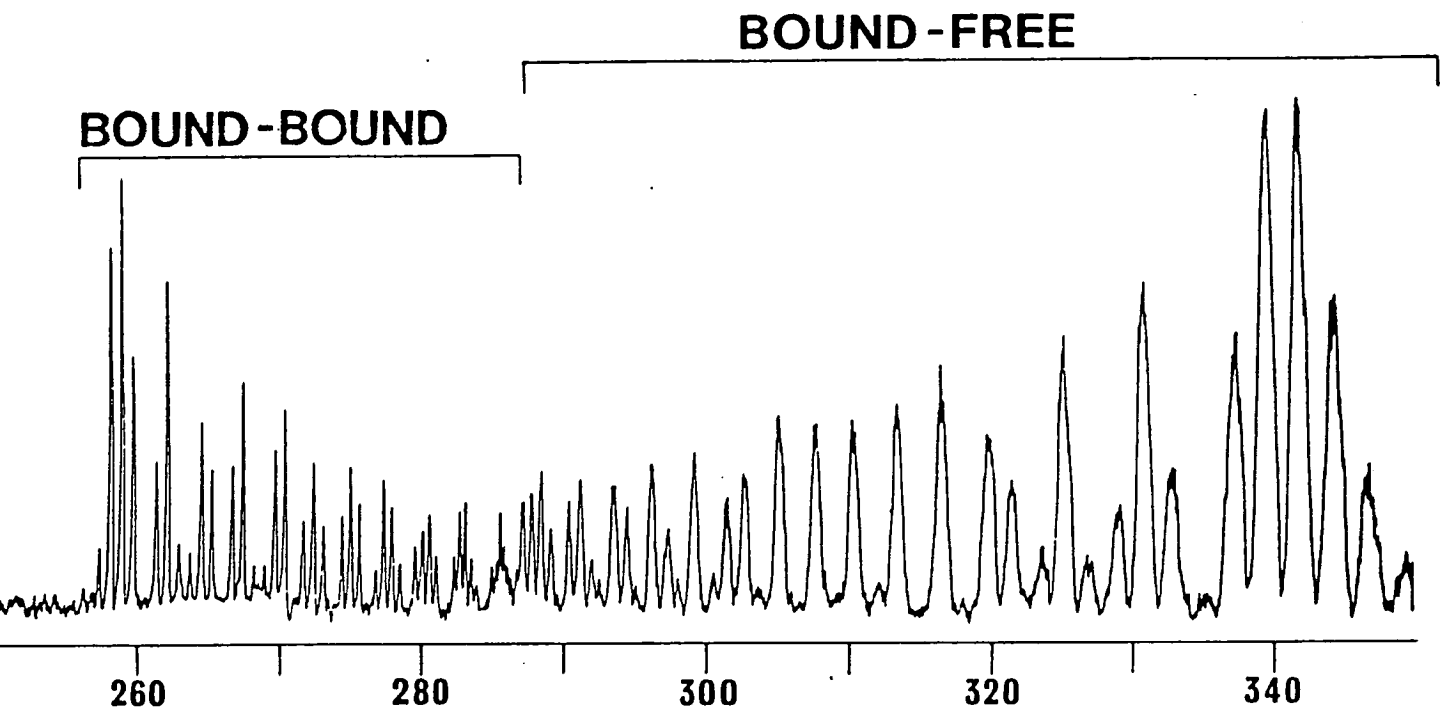

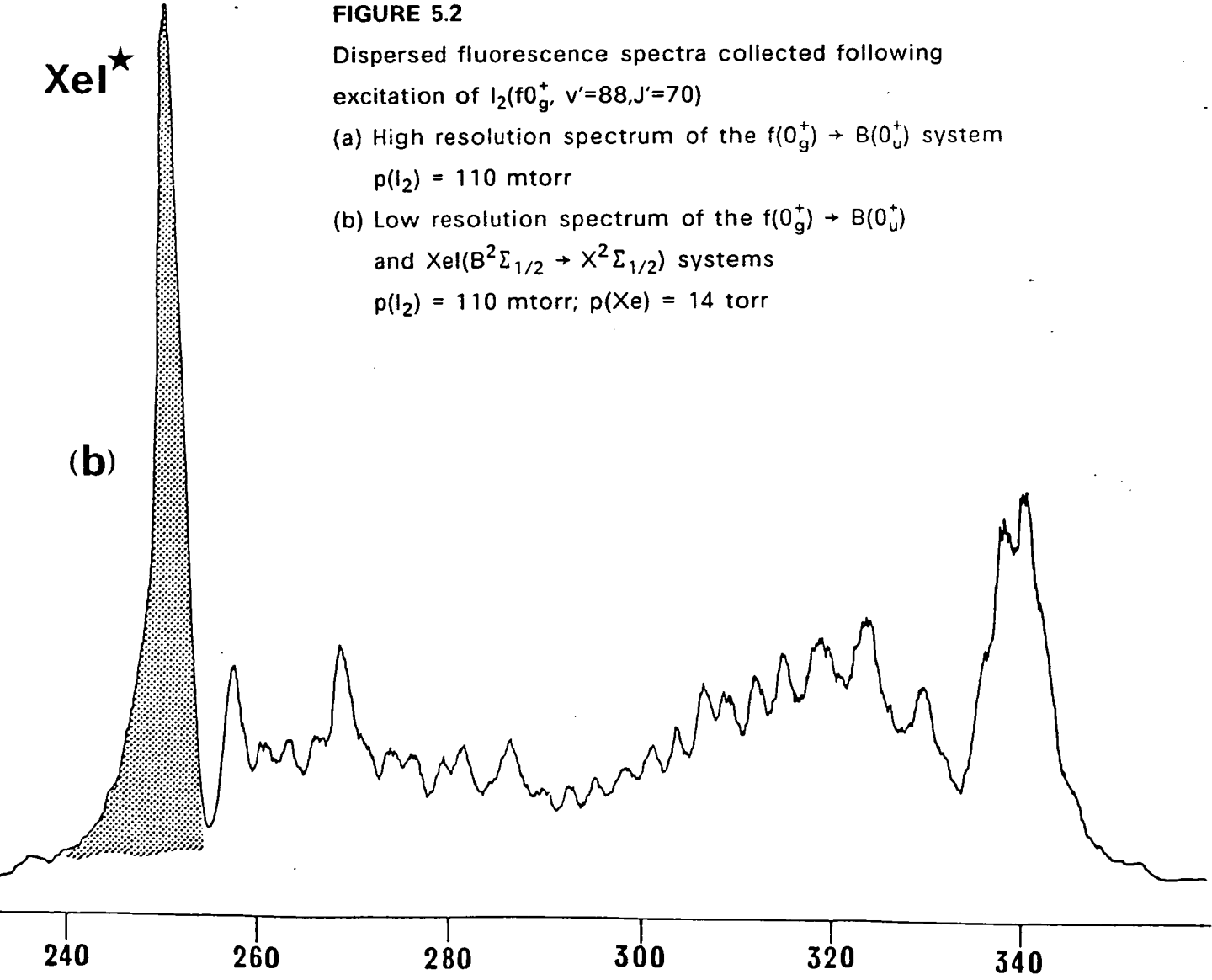

FIGURE 5.2

Dispersed fluorescence spectra collected following excitation of $I_2(f0_g^+, v'=88, J'=70)$

(a) High resolution spectrum of the $f(0_g^+) \rightarrow B(0_u^+)$ system
$p(I_2)$ = 110 mtorr

(b) Low resolution spectrum of the $f(0_g^+) \rightarrow B(0_u^+)$ and $XeI(B^2\Sigma_{1/2} \rightarrow X^2\Sigma_{1/2})$ systems
$p(I_2)$ = 110 mtorr; p(Xe) = 14 torr

from I_2 with no Xe present.

In order to carry out a time-integrated kinetic analysis of this system, the following reaction scheme was used:

1. $I_2 \rightarrow I_2^*$ absorption (5.1)
2. $I_2^* + Xe \rightarrow XeI^* + I$ reaction (5.2)
3. $I_2^* \rightarrow I_2 + h\nu_1$ fluorescence (5.3)
4. $I_2^* + Xe \rightarrow I_2^{*'} + Xe$ quenching (5.4)
5. $XeI^* \rightarrow Xe + I + h\nu_2$ chemiluminescence (5.5)

$I_2^{*'}$ denotes other states of I_2 populated by physical quenching. Physical quenching of $XeI^*(B^2\Sigma_{1/2})$ and of I_2^* by I_2 are not important under the experimental conditions used. It is assumed that the laser excitation has a square pulse time profile (approx. width 10ns) giving instantaneous excitation to the upper state. The intensity of fluorescence is then proportional to the time integrated population of the upper state. From the above scheme, processes 5.2 - 5.4 contribute to the loss of $I_2^*(f0_g^+)$.

$$-d[I_2^*]/dt = k_2[Xe][I_2^*] + k_3[I_2^*] + k_4[Xe][I_2^*]$$

$$\Rightarrow -d[I_2^*]/dt = k'[I_2^*]$$

where

$$k' = k_2[Xe] + k_3 + k_4[Xe]$$

Integrating this expression with respect to time yields the I_2^* concentration at time t:

$$[I_2^*] = [I_2^*]_0.e^{-k't} \qquad (5.6)$$

where

$$[I_2^*]_0 = [I_2^*] \text{ at } t=0.$$

The total integrated fluorescence intensity, $I(I_2^*)$, is given by:

$$I(I_2^*) \propto k_3 \int_0^\infty [I_2^*]\, dt$$

$$\Rightarrow I(I_2{}^*) \propto k_3[I_2^*]_0/k' \qquad (5.7)$$

The time dependence of the XeI^* population is given by:

$$-d[XeI^*]/dt = -k_2[Xe][I_2^*] + k_5[XeI^*]$$

Substitution for $[I_2^*]$ from (5.6) and multiplication by the integrating factor, $e^{-k_5 t}$, allows this expression to be integrated, yielding:

$$[XeI^*]e^{-k_5 t} = k_2[Xe][I_2^*]_0 . e^{-(k'-k_5)t}/-(k'-k_5) + K$$

At t=0, $[XeI^*]=0$

$$\Rightarrow K = k_2[Xe][I_2^*]_0/(k'-k_5)$$

Thus at time t:

$$[XeI^*] = k_2[Xe][I_2^*]_0 . e^{-k_5 t} - e^{-k' t}/(k'-k_5) \qquad (5.8)$$

and the total integrated intensity of fluorescence emission from XeI^*, $I(XeI^*)$, is given by:

$$I(XeI^*) \propto k_5 \int_0^\infty [XeI^*]\, dt$$

Following substitution for $[XeI^*]$ from (5.8) and integration, it can be shown that:

$$I(XeI^*) \propto k_2[Xe][I_2^*]_0/k'$$

Thus,

$$I(XeI^*)/I(I_2^*) = k_2[Xe][I_2^*]_0 k'/k' k_3[I_2^*]_0$$

$$\Rightarrow I(XeI^*)/I(I_2^*) = k_2[Xe]/k_3 \qquad (5.9)$$

Thus, the reaction rate constant can be determined by monitoring the XeI^* and I_2^* emission intensities as a function of pressure. Also, determination of the ratio $I(XeI^*)/I(I_2^*)$ as a function of vibronic level, for fixed pXe, will give the excitation function for XeI^* formation, assuming the radiative lifetime of $I_2(f0_g^+)$ to be constant.

The rate constant for removal of I_2^* by Xe via all channels can also be obtained. When no Xe is present

$$I(I_2^*)_0 \propto k_3[I_2^*]_0 \cdot \int_0^\infty e^{-k_5 t}\, dt$$

$$\Rightarrow I(I_2^*)_0 \propto [I_2^*]_0$$

Dividing the above by (5.7) yields:

$$I(I_2^*)_0/I(I_2^*) = k'/k_3 = k_3/(k_2[Xe] + k_3 + k_4[Xe])$$

$$\Rightarrow I(I_2^*)_0/I(I_2^*) = (k_{Xe}[Xe]/k_3) + 1 \qquad (5.10)$$

where $k_{Xe} = k_2 + k_4$ = rate constant for removal by Xe (all channels)

Thus, by monitoring the intensity of emission of $I_2(f0_g^+)$ as a function of Xe partial pressure, k_{Xe} may be determined provided the fluorescence lifetime of the f state is known.

The above time-integrated kinetic scheme has the advantage that, in contrast to Stern-Volmer analysis, the assumption of a steady-state population of $I_2(f0_g^+)$ does not need to be invoked. The pulsed nature of the experiments render such an assumption invalid.

5.5 Determination of the vibronic excitation function

Fig 5.3 shows the vibronic excitation function obtained for the reaction of $I_2(f)$ with Xe, using equation (5.9). The Optical-Optical Double Resonance technique was used to populate the $f(0_g^+)$ state in specific rovibronic levels from v'=0 up to v'=107. Details of the assignments of rovibronic resonances in the OODR excitation spectrum are given in Chapter 3. Use of OODR allows the entrance channel for reaction to be precisely defined. The I_2 molecule is prepared with well determined electronic, vibrational and rotational energies and the Xe atomic collision partner is in its electronic ground state. Use of two independently tunable dye lasers allows selective population of a range of ion-pair rovibronic levels ,enabling the effect of internal energy on reaction to be studied.

The lowest level for which XeI^* chemiluminescence was detected was $I_2(f0_g^+, v'=52)$. The relative fluorescence intensity of the XeI^* product is observed to increase upon excitation to successively higher vibronic levels of the $f(0_g^+)$ state up to v'=88. Between v'=88 and 101 the yield of $XeI^*(B)$ appears to be independent of $f(0_g^+)$ vibrational level, before increasing again from v'=104. A full discussion of the nature of this excitation function is given in section 5.6 .

5.5.1 Measurement of state-specific rate constants

The intensities of the $XeI^*(B \rightarrow X)$ and $I_2(f0_g^+ \rightarrow B0_u^+)$ emission systems have been monitored as a function of Xe partial pressure, following excitation into $I_2(f0_g^+$, v'=62 and 93). XeI^* fluorescence intensity is

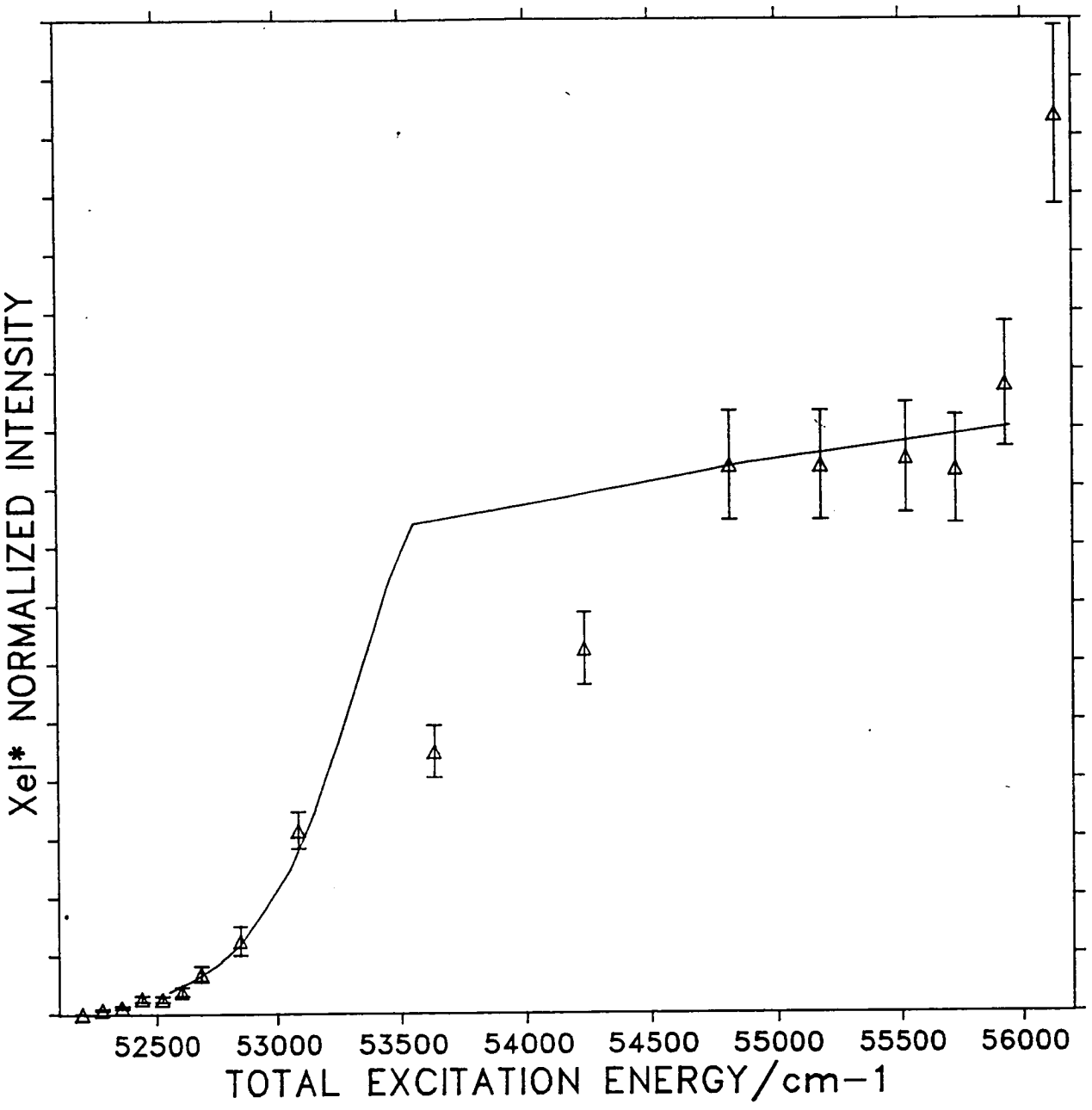

FIGURE 5.3

Emission intensity ratio $(Xe^*)/(I_2^*)_0$ as a function of total excitation energy for the vibrational range $f(0_g^+, v'=50-107)$. The levels $v'=62$ and 93 correspond to excitation energies of $52845cm^{-1}$ and $55177cm^{-1}$, respectively. The solid line represents a fit to the experimental data, using a harpooning model (see 5.6) .

shown as a function of Xe pressure in Fig 5.4 and varies linearly with the pressure of Xe as predicted by equation (5.9) . XeI^* emission intensity is observed to decrease at higher pressures. This is thought to be due to quenching of the intermediate state in the double resonance excitation process and quenching of XeI^* by Xe.

Figure 5.4 shows the experimental pressure dependences of the XeI^* and I_2 emission systems, obtained by measuring the total integrated emission from each of these states, for v'=93. The intensity of the blue extremum of the $I_2(f0_g^+)$ emission is measured. The ratio of this height to the total emission intensity from the vibronic level initially excited is determined by measuring the area under the emission band when only I_2 is present in the cell. The slope of this plot has been used to determine the values of the reaction and total removal rate constants using equations 5.9 and 5.10, along with those for v'=62. The radiative lifetime of $I_2(f0_g^+)$ has not yet been determined, although lifetimes for the $D(0_u^+)$, $E(0_g^+)$, $\beta(1_g)$ and $D'(2_g)$ states have been reported (15, 28, 12 and 6.7 ns respectively) [34-36]. It is reasonable to assume that the radiative lifetime for $I_2(f0_g^+)$ lies in this range and a value of 20 ns has been taken in estimating the rate constants listed in Table 5.1.

5.6 XeI^* Excitation function

Fig 5.3 shows the integrated fluorescence intensity of XeI^* plotted as a function of vibronic level in the $f(0_g^+)$ ion-pair state of I_2. The onset of reaction lies between 52100 and 52900cm^{-1} which can be compared with the value of 52300cm^{-1} for the thermodynamic

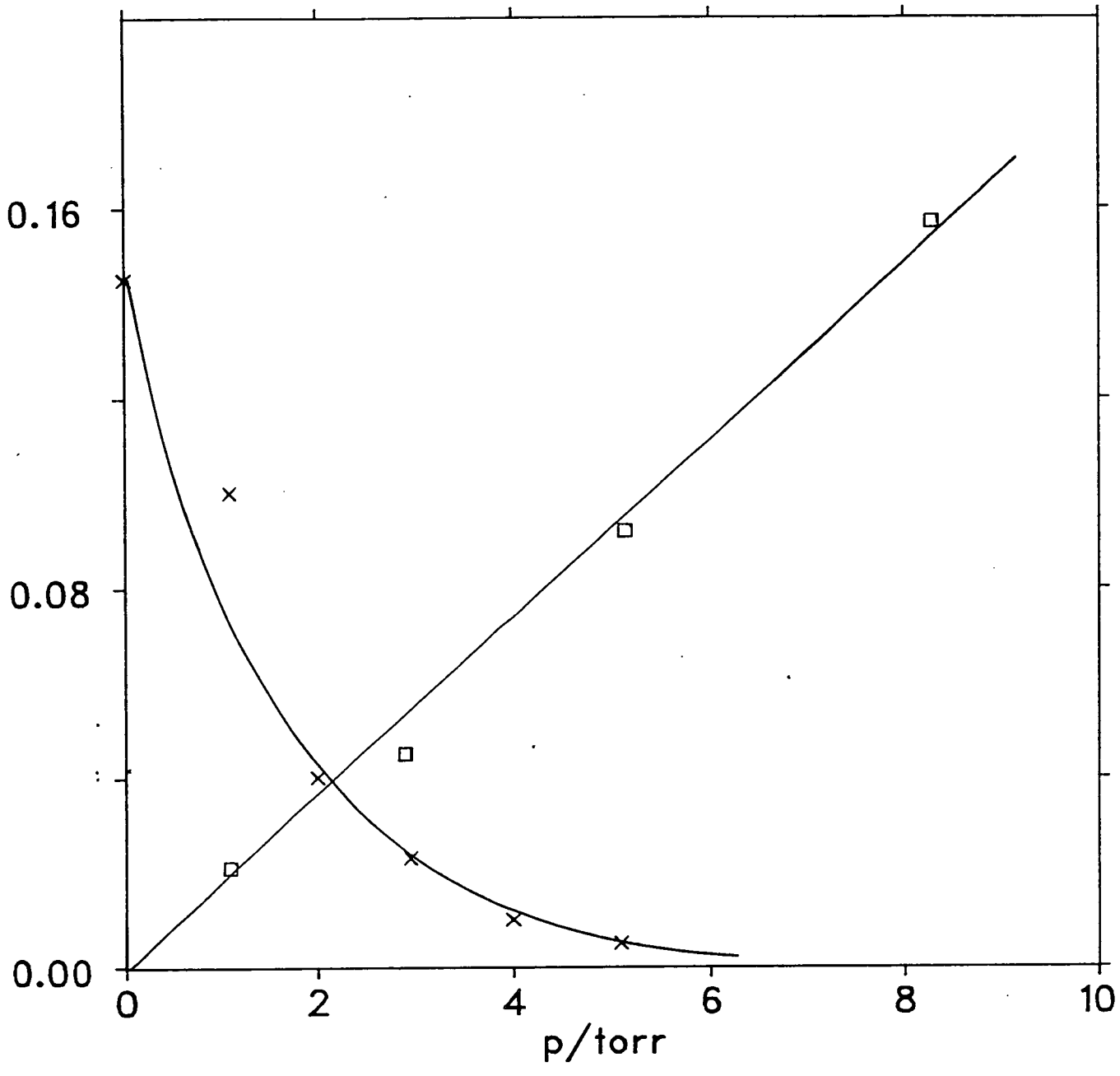

FIGURE 5.4

Growth of $XeI^*(B)$ (squares) and loss of $I_2(f0_g^+)$ (crosses) as a function of Xe partial pressure.

The XeI^* values should be divided by 30 for a direct comparison

Table 5.1

Rate constants for removal of $I_2(f0_g^+)$ by Xe, (cm^3 $molecule^{-1}$ s^{-1}).

v'	Total removal	Reaction
62	$2.7\pm0.7 \times 10^{-10}$	$3.5\pm0.5 \times 10^{-11}$
93	$7.7\pm0.7 \times 10^{-10}$	$1.6\pm0.1 \times 10^{-10}$

(estimated by assuming a radiative lifetime of 20 ns for the $f(0_g^+)$ state.)

threshold, indicating the absence of any substantial barrier in the entrance channel for reaction. The reaction rate is observed to increase with ion-pair vibronic energy in contrast with molecular beam studies of the reactions of excited rare-gas atoms where, in general, reaction cross-sections are observed to decrease with increasing translational energy. Excitation to the $f(0_g^+)$ ion-pair state increases the effective electron affinity of I_2. As a result of this, crossing to the ionic $Xe^+I_2^-$ surface occurs at large r. In terms of the simplest quantitative harpooning model developed by Magee [4]:

$$R_c = e^2/(IP(Xe)-EA(I_2)) \qquad (5.11)$$

Where,

R_c = curve crossing distance
$IP(Xe)$ = ionisation potential of $Xe(^1S_0)$
$EA(I_2)$ = electron affinity of $I_2(f0_g^+)$

The reaction cross-section can then be estimated from

$$\sigma = \pi R_c^2 \qquad (5.12)$$

The first step in modelling the effect of vibrational energy on the reaction cross-section is to estimate the effect on the electron affinity of the halogen partner. Accurate determination of electron affinities for halogen molecules has proved to be one of the limiting factors in the many models developed to calculate harpooning cross-sections. However, Gislason has described a method for estimating "reactive" electron affinities for halogen molecules which gives good agreement with experimental observations of alkali metal/halogen reactions. The potential curves for $I_2(X0_g^+)$, $I_2(f0_g^+)$ and $I_2^-(^2\Sigma_u^+)$ are shown in Figure 5.5 . The curves

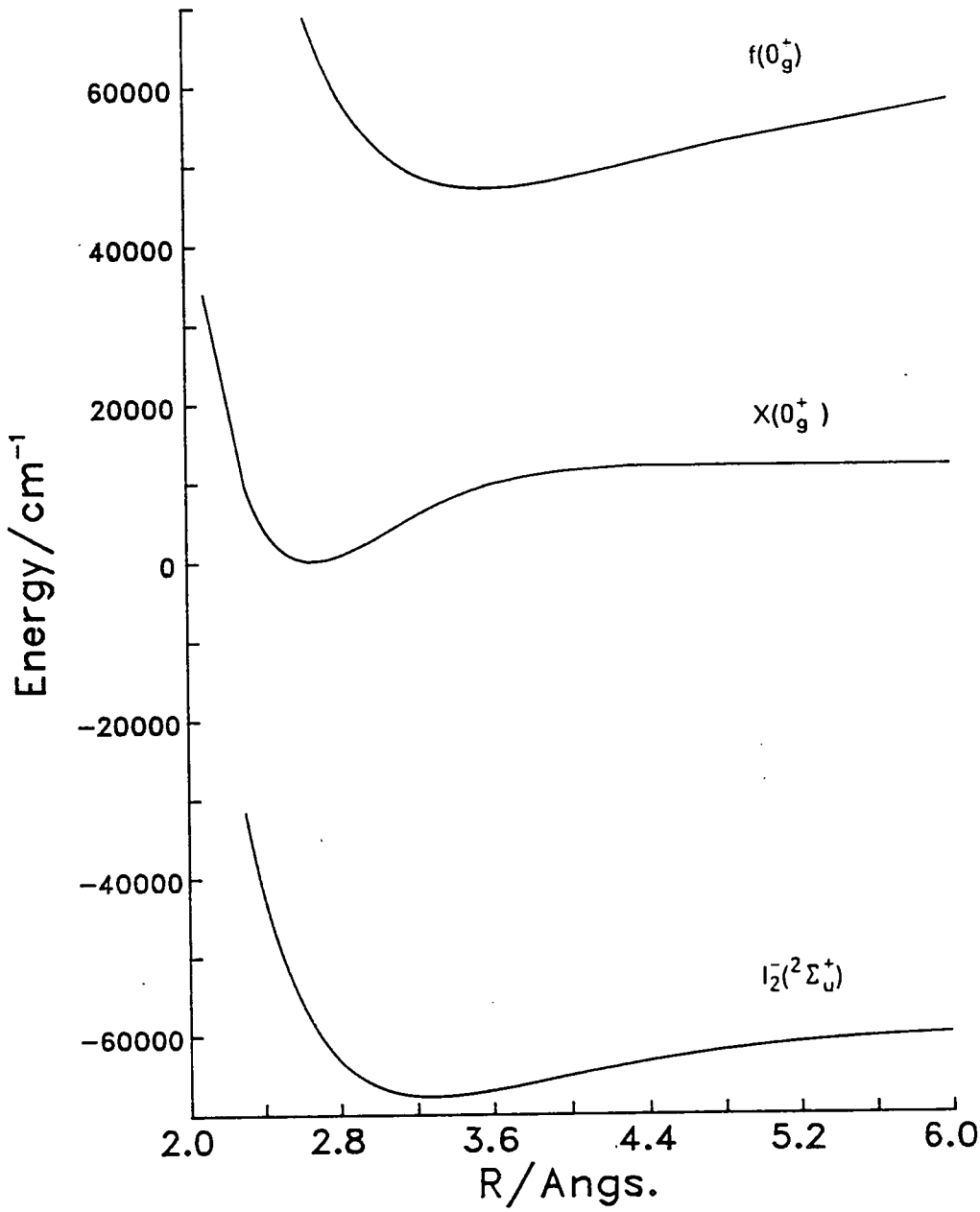

FIGURE 5.5

Potential curves for

$I_2(X0_g^+)$ $I_2(f0_g^+)$ and $I_2^-(^2\Sigma_u^+)$

for the X and f states were constructed from the RKR analyses of Tellinghuisen and Perrot et al. respectively [32,38]. The I_2^- potential was obtained by fitting the calculated values of Tasker et al. for D_e, ω_e and r_e to a Morse potential curve [39]. The electron affinity at a given internuclear distance, R, is calculated by subtracting the value for I_2^- from the appropriate covalent curve. It is assumed that transfer to the ionic surface is governed by Franck-Condon restrictions. Thus for higher vibrational levels, the electron affinities at the outer turning points are estimated to give the "reactive" electron affinity to be used in cross-section calculations.

It is known from the studies of the reactions of alkali metal atoms with diatomic halogen molecules that the simple harpooning model of Magee does not give exact quantitave values for $M+X_2$ reaction cross-sections. Gislason and Sachs have found that the $M+X_2$ covalent potential surface, assumed to be flat in equation 5.11, has a significant effect on the reactive cross-section. A "refined" harpooning model has been developed taking into account the functional form of the covalent potential [37,40]. Although this model gives quantitative estimates for cross-sections of up to 10% greater than the predictions of the simple harpooning model, a similiar dependence on the halogen electron affinity is observed. In the following discussion, the simple harpooning model has been applied to describe the effect of halogen vibronic energy on the reaction cross-section. This model accounts for the major attributes of harpooning reactions with cross-sections of less then $200Å^2$ and is more straightforward to apply than the refined model which would require calculation of the long range $Xe-I_2^*$ potential surface. Fig 5.6

shows the calculated "reactive" electron affinities of the $I_2(X0_g^+)$ and $I_2(f0_g^+)$ states, as a function of vibronic energy. Using the model of Magee , the crossing radii for the reactions (a) $I_2(X0_g^+)+Xe^*(^3P_2)$ and (b) $I_2(f0_g^+)+Xe(^1S_0)$ have been calculated for v'=0-100. The results are shown in Fig 5.7. The cross-section for the reaction of the $Xe^*(^3P_2)$ metastable with $I_2(X)$ shows a marked dependence upon the available vibronic energy in the entrance channel, as predicted by Herschbach for alkali-halide formation from ground state halogen molecules [41]. Indeed, a key feature in modelling such reactions is the accurate estimation of the internal energy of the diatomic partner. This effect arises as a result of the close matching of the ionisation potential of $Xe^*(^3P_2)$ with the reactive electron affinity of $I_2(X)$ (approximately 4 and 2-3eV respectively). The reaction of $I_2(f)$ with ground state Xe is expected to be less sensitive to vibronic energy. In this case the denominator of equation 5.11 is dominated by the large ionisation potential for $Xe(^1S_0)$ of 12.125ev and changing the reactive electron affinity from 8 to 9eV has a less significant effect on R_c.

Figure 5.8 shows the cross-section for reaction (b) calculated using equation 5.12. The reaction cross-section is observed to increase with vibronic energy in the f state. However, the slope of this plot is far shallower than the experimental excitation function. Fig 5.3 shows the results of the above calculation scaled to match the calculated cross-section at v'=93 (σ=73.4Å^2) with the experimental value (σ= 60±20Å^2). If the post-threshold behaviour was described by a step function then the experimental curve should show a steep increase followed by levelling off to match the calculated curve. However, the post threshold increase is observed to

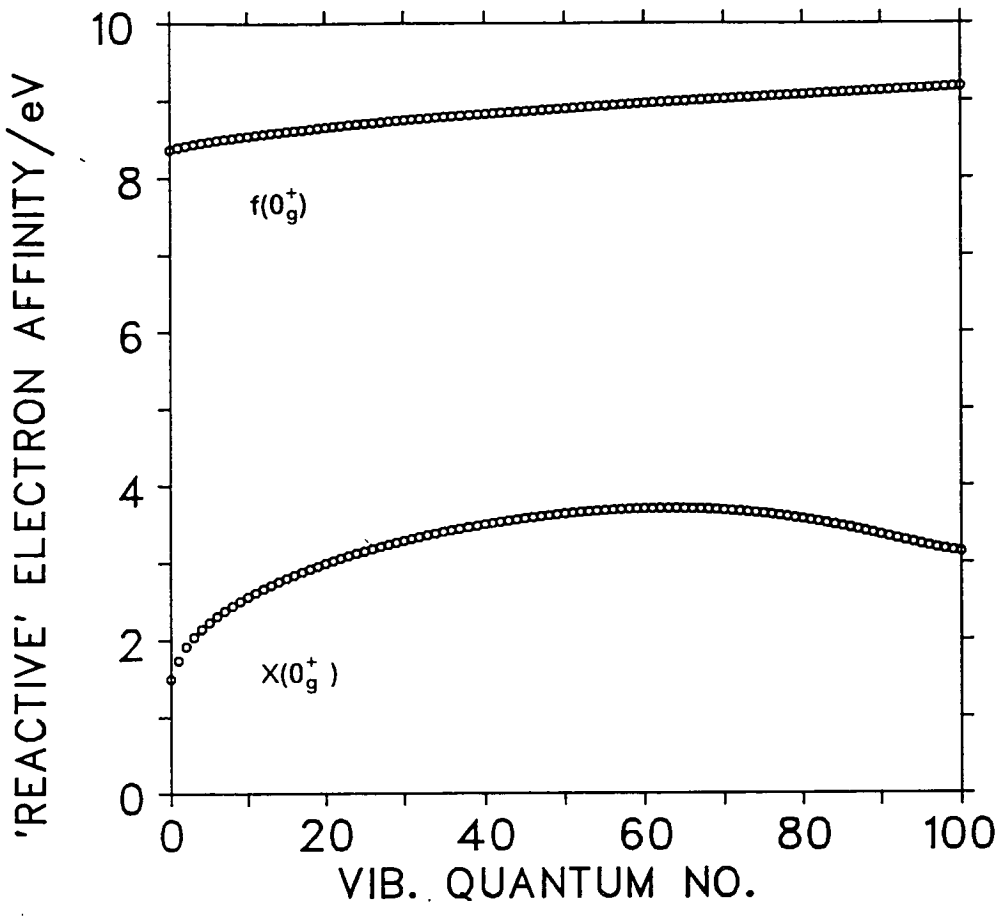

FIGURE 5.6

Reactive electron affinities for I_2(X and f) as a function of vibronic energy.

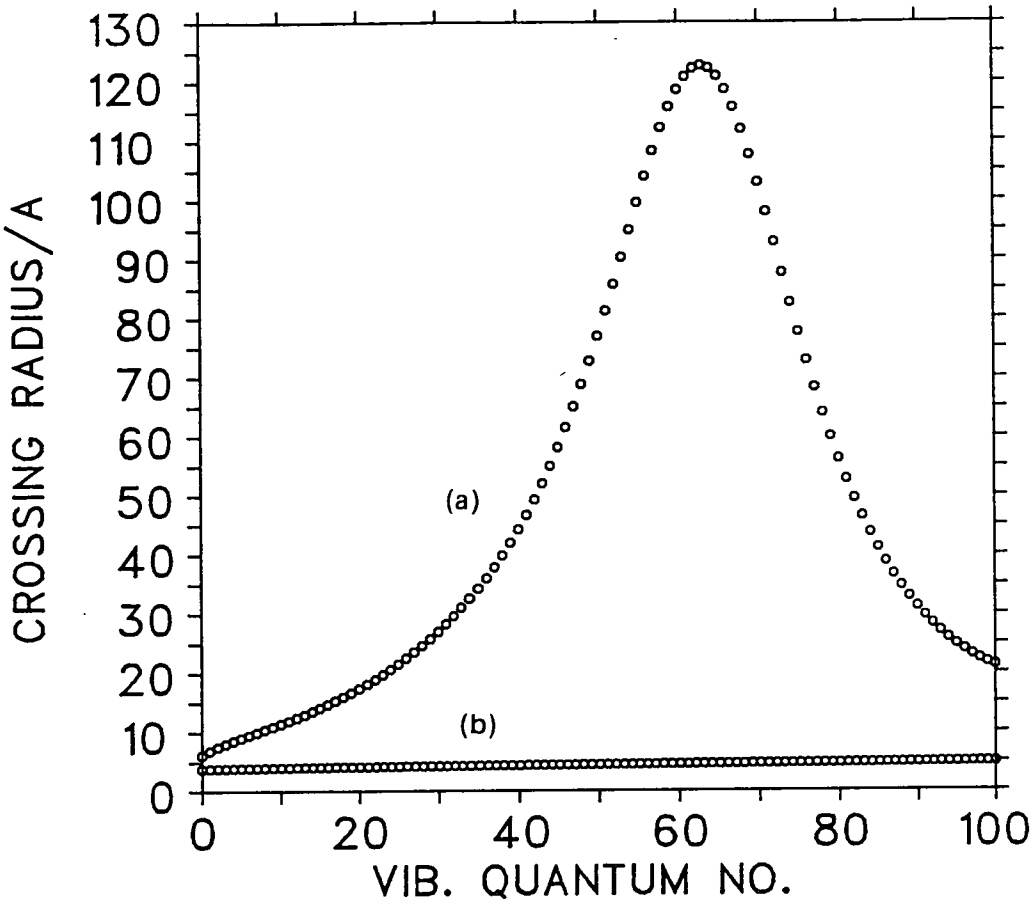

FIGURE 5.7

Calculated crossing radii for the reactions:

(a) $I_2(X0_g^+) + Xe^*(^3P_2)$

(b) $I_2(f0_g^+) + Xe(^1S_0)$

as a function of I_2 vibrational quantum number.

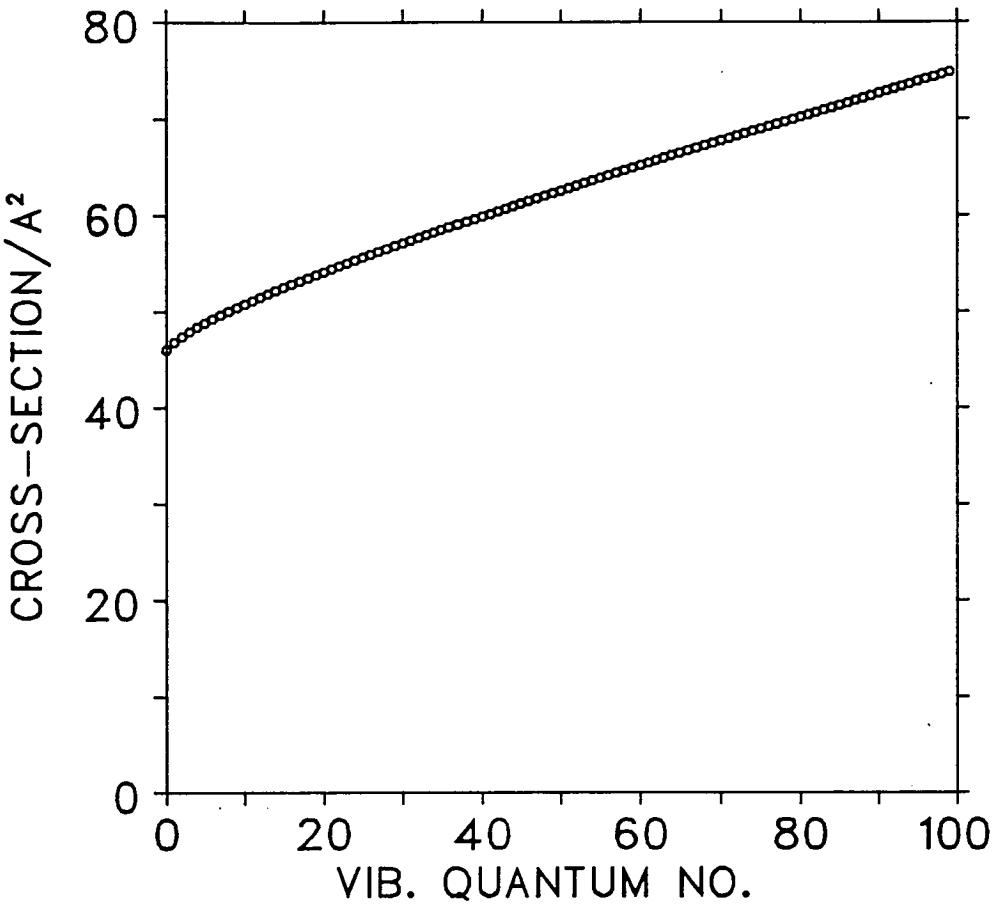

FIGURE 5.8

Calculated cross-sections for the reaction:
$I_2(f0_g^+) + Xe(^1S_0) \rightarrow Xe!^*(B^2\Sigma_{1/2}) + I(^2P_{3/2})$
as a function of vibrational quantum number.

be far gentler than this. The absorption corrected curve obtained by Donovan et al. for the IBr/Xe reaction shows similiar behaviour [11]. Coupling of the translational energy of the Xe atoms to reaction may result in observation of product formation below reaction threshold. In this case, the reaction rate constant would be given by

$$k = \int_{v^*}^{\infty} \sigma(v)\, v\, P(v)\, dv \quad ,v^* = \text{threshold velocity} \qquad (5.13)$$

It is reasonable to assume that the cross-section, σ, is independent of v over the distribution of available speeds, giving:

$$k(v) = \sigma \int_{v^*}^{\infty} v\, P(v)\, dv \qquad (5.14)$$

P(v) is the distrubtion of molecular velocities and can be modelled using the Maxwell-Boltzmann distribution, in three dimensions, to give:

$$k(v) = \sigma\, 2\pi\, (a/\pi)^{3/2}\, \exp(-av^2)\, a^{-2}(1+av^2) \qquad (5.15)$$

where $a = \mu/2kT$

The above quantity was calculated using the cross-section values predicted by the simple harpooning model. In order to match the results of this calculation with the observed excitation function the reaction threshold has to be moved to higher energies, implying a barrier to reaction. The solid curve on Fig 5.3 shows the effect of introducing a barrier of 1500cm^{-1} and convoluting the cross-section for the distribution of available kinetic energies. This gives a better fit to the experimental result in the threshold region, but deviates strongly above 53,200cm^{-1}. If this were taken as the explanation for the XeI^* excitation curve then the observation of the onset of reaction close to the thermodynamic threshold would be a

coincidence. However, similar onsets have been observed for a range of reactions of halogens and interhalogens with Xe. There is no obvious explanation for the presence of a barrier to reaction although preparation of the reacting I_2 molecule in a high rotational quantum state might affect this. Thus, whilst not discounting this explanation, it is important to consider other factors which might explain the experimental results.

The production of higher electronically excited states of XeI or $I^*(^2P_{1/2})$ can be ruled out on energetic grounds. Formation of $I^*(^2P_{1/2})$ requires approximately 60000cm^{-1} whilst the thermodynamic threshold for production of $XeI^*(D^2\Sigma_{1/2})$ is estimated to be close to 62000cm^{-1}. It is possible that consumption of I_2^* in dark channels may play an important role, possibly through coupling to non-reactive Rydberg states.

The above model assumes that once the collision partners approach within R_c, reaction will automatically ensue. However, consideration of the rate constants listed in Table 5 indicates that reaction is not the major channel and also that the branching ratio for reaction varies as a function of vibronic energy. The dominant channels are physical quenching transfer processes into other ion-pair states. Lawley has shown that these quenching processes are orbiting controlled and thus are expected to have cross-sections which are greater than the corresponding harpooning values [42]. The key to accurately modelling the XeI^* excitation function clearly lies in working out the branching ratios for reaction and electronic quenching, as a function of vibrational quantum number. One way

to estimate this would be to carry out a phase-space calculation , taking into account the ratio of available reaction and quenching product states. At threshold, XeI^* can only be formed in its lowest vibrational state. As the available energy is increased, the number of possible XeI^* products will be expected to show a marked increase with respect to the electronic quenching channel.

In conclusion, the excitation function for formation of XeI^* for OODR excitation of Xe/I_2^* mixtures has been measured as a function of vibrational level in the $f(0_g^+)$ ion-pair state. State specific rate constants for reaction and total removal have been measured, indicating that the branching ratio for reaction is a function of excitation energy. A simple harpooning model gives a qualitative description of the observation that the yield of XeI^* increases as a function of vibronic energy in the ion-pair state. The above study has successfully demonstrated the versatility of the OODR technique for the study of gas phase reactions involving highly excited species. By judicious selection of the intermediate state, reactions of heavy species, such as I_2 , may be studied as a function of electronic, vibrational and even rotational energy.

5.7 References

1. M.G. Golde and B.A. Thrush, Chem. Phys. Lett. **29**, 484 (1974)
2. D.W. Setser, T. Dreiling, H.C. Brashears, Jr. and J. H. Kolts, Discuss. Farad. Soc. **67**, 255 (1979) and references therein.
3. M. Polanyi, "Atomic Reactions", (Williams and Norgate, London, 1932)

4. J.L. Magee, J. Chem. Phys. **8**, 687 (1940)
5. J.L. Fraites and D.H. Winicur, Mol. Phys. **35**, 927 (1978)
6. M.F. Golde, J. Mol. Spec. **58**, 261 (1975)
7. J.E. Velazco and D.W. Setser, J. Chem. Phys. **62**, 1990 (1975)
8. C.A. Brau and J.J. Ewing, J. Chem. Phys. **63**, 4640 (1975)
9. J. Tellinghuisen, A.K. Hays, J.M. Hoffman and G.C. Tisone, J. Chem. Phys. **65**, 4473 (1976)
10. K. Tamagake, D.W. Setser and J.H. Kolts, J. Chem. Phys. **74**, 4286 (1981)
11. R.J. Donovan, P. Greenhill, M.A. MacDonald, A.J. Yencha, W.S. Hartree, K. Johnson, C. Jouvet, A. Kvaran and J.P. Simons, Farad. Discuss. Chem. Soc. **84**, 221 (1987)
12. J.K. Ku, G. Inoue and D.W. Setser, J. Phys. Chem. **87**, 2989 (1983)
13. D.W. Setser and J.K. Ku, "Photophysics and Photochemistry Above 6eV" (Elsevier, Amsterdam, 1985)
14. M. Boiveneau, J. LeCalve, M.C. Castex and C. Jouvet, Chem. Phys. Lett. **128**, 208 (1986)
15. M. Boiveneau, J. LeCalve, M.C. Castex and C.Jouvet, Chem. Phys. Lett. **128**, 528 (1986)
16. M. Boiveneau, J. LeCalve, M.C. Castex and C. Jouvet, J. Chem. Phys. **84**, 4712 (1986)
17. D.H. Ehrlich and R.M. Osgood, J. Chem. Phys. **73**, 3038 (1980)
18. M.C. Castex, J. LeCalve, D. Haaks, B. Jordan and G. Zimmerer, Chem. Phys. Lett. **70**, 106 (1980)
19. T. Moller, B. Jordan, G. Zimmerer, D. Haaks, J. LeCalve and M.C. Castex, Z. Phys. D. **4**, 73 (1986)
20. J.P.T. Wilkinson, M. MacDonald and R.J. Donovan, Chem. Phys.

Lett. **101**, 284 (1983)

21. B.V. O'Grady and R.J. Donovan, Chem. Phys. Lett. **122**, 502 (1985)
22. J.P.T. Wilkinson, E.A. Kerr, K.P. Lawley, R.J. Donovan, D. Shaw, A. Hopkirk and I. Munro, Chem. Phys. Lett. **130**, 213 (1986)
23. J.P.T. Wilkinson, M.A. MacDonald and R.J. Donovan, J. Photochem. **35**, 123 (1986)
24. R.J. Donovan, A.J. Holmes, P.R.R. Langridge-Smith and T. Ridley, J. Chem. Soc. Farad. Trans II **84**, 541 (1988)
25. N.K. Bibinov and I.P. Vinogradov, Opt. Spectrosc. **59**, 191 (1985)
26. T. Ishiwata, A. Tokunaga and I. Tanaka, Chem. Phys. Lett. **112**, 356 (1984)
27. M.S. deVries, V.I. Srdanov, C.P. Hanrahan and R.M. Martin, J. Chem Phys. **78**, 5582 (1983)
28. K. Johnson, R. Pease, J.P. Simons and P.A. Smith, J. Chem. Soc. Farad. Trans. II **82**, 1281 (1983)
29. K. Johnson, J.P. Simons, P.A. Smith and A. Kvaran, J. Chem. Phys. **84**, 371 (1987)
30. S. Gerstenkorn and P. Luc, "Atlas du spectre d'absorption de la molécule d'iode", (CNRS, Paris, 1978)
31. P. Luc, J. Mol. Spec. **80**, 41 (1980)
32. J.P. Perrot, A.J. Bouvier. A. Bouvier, B. Femelat and J. Chevaleyre, J. Mol. Spec. **114**, 60 (1985)
33. A.L. Guy, K.S. Viswanathan, A. Sur and J. Tellinghuisen, Chem. Phys. Lett. **73**, 582 (1980)
34. A.B. Callear ,P. Erman and J. Kurepa, Chem. Phys. Lett. **44**, 599 (1976)
35. J. Chevaleyre, J.P. Perrot, J.M. Chastan, S. Valignat and

M. Broyer, Chem. Phys. **67**, 59 (1982)

36. M.C. Sauer, W.A. Mulac, R. Cooper and F.Grieser, J. Chem. Phys. **64**, 4587 (1976)
37. E.A. Gislason in "The Alkali Halide Vapours", Ed. P. Davidovits and D. McFadden (Academic, New York, 1978)
38. J. Tellinghuisen, M.R. McKeever and A. Sur, J. Mol. Spec. **82**, 225 (1980)
39. P.W. Tasker, G.G. Balint-Kurti and R.N. Dixon, Mol. Phys. **32**, 1651 (1976)
40. E.A. Gislason and J.G. Sachs, J. Chem. Phys. **62**, 2678 (1975)
41. D.R. Herschbach, "Reactive Scattering in Molecular Beams", Adv. Chem. Phys. **10**, 319 (1966)
42. K. Lawley, Chem. Phys. **127**, 363 (1988)

Appendix A
Conferences and Lectures Attended

A.1 Lectures Attended

In accordance with the regulations of the University of Edinburgh, Department of Chemistry, the following lecture courses were attended during the last three years:

1. Atmospheric Chemistry
2. Lasers
3. Quantum Chemistry
4. EMAS-SCRIBE Users Course
5. Signal Processing
6. Mass Spectrometry
7. Recent Advances in Physical Chemistry

A.2 Conferences and Meetings Attended

1. High Resolution Spectroscopy Group; York (1985) and Reading (1987)
2. Scottish Quantum Chemistry Group; Strathclyde (1986)
3. International Symposia on Gas Kinetics; Bordeaux (1986) and Swansea (1988)
4. Gas Kinetics Discussion Group; Edinburgh (1987)
5. XIth International Symposium on Molecular Beams; Edinburgh (1987)
6. 84th Faraday Discussion; Birmingham (1987)

In addition, all regular research group meetings were attended along with departmental seminars. A number of joint meetings with the spectroscopy group at Heriot-Watt University were also attended.

Appendix B
Publications

J. Chem. Soc., Faraday Trans. 2, 1988, 84(5), 541–548

Optical-Optical Double Resonance (OODR) Studies of the Ion-pair States of the Halogens

Part 1.—Vibronic Threshold for the Chemiluminescent Reaction between $I_2(f\,0_g^+)$ and Xe

Robert J. Donovan,* Andrew J. Holmes, Patrick R. R. Langridge-Smith† and Trevor Ridley

Department of Chemistry, University of Edinburgh, West Mains Road, Edinburgh EH9 3JJ

The technique of optical-optical double-resonance (OODR) spectroscopy has been used to study the collisional dynamics of the $f(0_g^+)$ state of I_2 in the presence of Xe. Using the $B(^3\Pi_{0_u^+})$ state as an intermediate we have succeeded in selectively populating specific rovibronic levels of the $f(0_g^+)$ state from $v'=0$ up to $v'=107$. Dispersed fluorescence has been observed from a number of single rovibronic levels in this range. The energetic threshold for the chemiluminescent reaction

$$I_2(f\,0_g^+, v'=n)+Xe \rightarrow XeI(B\,^2\Sigma_{1/2})+I(^2P_{3/2})$$

has been determined as $52\,460\pm400\ cm^{-1}$, which corresponds to $v'=52$–57. The reaction was monitored by observing fluorescence from $XeI(B\,^2\Sigma_{1/2})$ at 253 nm.

The potential minima of the lowest group of ion-pair states of I_2 lie at *ca.* $40\,000\ cm^{-1}$.[1] This lowest group consists of six states (0_g^+, 0_u^+, 1_g, 1_u, 2_g, 2_u) which correlate asymptotically with $I^+(^3P_2)$ and $I^-(^1S_0)$. Two more groups of six states, correlating with $I^+(^3P_{1,0})+I^-(^1S_0)$ and $I^+(^1D_2)+I^-(^1S_0)$, lie higher in energy by *ca.* $7000\ cm^{-1}$ and $12\,000\ cm^{-1}$, respectively.

The collisional behaviour of the $D(0_u^+)$ state of I_2, which belongs to the lowest group of ion-pair states, has been studied in some detail.[2,3] It has previously been shown that $I_2(D0_u^+)$ reacts with Xe to yield $XeI(B\,^2\Sigma_{1/2})$ and an approximate threshold has been determined for this process.[4]

In this work we present our first results on the collisional behaviour of the $f(0_g^+)$ state of I_2, which lies in the second group of ion-pair states. Note that the $f(0_g^+)$ state is not accessible from the ground electronic state using single-photon excitation owing to the symmetry restriction ($g \not\leftrightarrow g$). We have therefore employed double-resonance techniques to access the $f(0_g^+)$ state[5,6] and, by using various vibronic levels of the $B(^3\Pi_{0_u^+})$ intermediate state, have succeeded in selectively populating the entire $f(0_g^+)$ vibrational manifold between $v'=0$ and 107. This has enabled us to determine the vibronic threshold for the reaction

$$I_2(f\,0_g^+)+Xe \rightarrow XeI(B\,^2\Sigma_{1/2})+I(^2P_{3/2}). \quad (1)$$

† Nuffield Foundation Science Research Fellow.

Experimental

Two dye lasers were employed which were simultaneously pumped by a single excimer laser (Lambda Physik EMG201 MSC), operating on the 308 nm XeCl line. The first dye laser (Lambda Physik FL3002E) employed an intracavity etalon which provided a bandwidth of 0.04 cm^{-1}. This laser was used to pump selectively single rovibronic levels of the $B(^3\Pi_{0_u^+})$ state of I_2. The second dye laser (Lambda Physik FL2002) had a bandwidth of 0.2 cm^{-1} and was used to pump molecules, excited by the first laser, from the $B(^3\Pi_{0_u^+})$ state to the $f(0_g^+)$ state.

Samples of I_2 and Xe/I_2 mixtures were contained in a simple glass cell, fitted with Spectrosil quartz windows which were attached by fluorocarbon wax. Fluorescence was collected and imaged onto the entrance slit of a Jobin-Yvon HRS2 ($f/7$, 0.6m) monochromator using a 5 cm ($f/1.5$) focal-length condenser lens and 15 cm focal-length field lens. The dispersed emission at the exit slit was monitored using a Hamamatsu R928 photomultiplier, the output of which was fed to a Stanford Research Systems SR250 gated integrator, interfaced to an IBM PC-XT286 microcomputer. Wavelength-resolved emission spectra were also recorded, at somewhat lower resolution, using a Jarrell-Ash polychromator and an EG & G optical multichannel analyser (OMA III).

Results

Spectroscopic Studies

An excitation spectrum for the levels $v' = 51$–54 in the $f(0_g^+)$ state of iodine, recorded using the optical-optical double-resonance technique, is shown in fig. 1. The molecules were first pumped to the intermediate $B(^3\Pi_{0_u^+})$ state, using the line-narrowed laser locked to the transition:

$$B(^3\Pi_{0_u^+}) \xleftarrow[(19\text{-}2)R(72)]{} X(^1\Sigma_g^+).$$

The second laser was then used to pump molecules from the $B(^3\Pi_{0_u^+})$ state to selected rovibronic levels of the $f(0_g^+)$ ion-pair state. The simplicity of this excitation spectrum is a very clear demonstration that we have succeeded in pumping a single rovibronic level in the initial (B–X) step. Without an intracavity etalon it is difficult to pump a single rovibronic level, owing to the congested nature of the B–X system, with the double-resonance fluorescence excitation spectrum becoming more complex as more intermediate levels are involved.

We have recorded dispersed fluorescence emission from a wide range of $I_2(f\,0_g^+)$ vibrational levels up to $v' = 107$. Dispersed fluorescence spectra from several low-lying levels of the $f(0_g^+)$ state ($v' = 0, 1, 3, 5$) are shown in fig. 2. The bound-bound fluorescence around 340 nm is readily assigned as:

$$f(0_g^+, v' = n) \rightarrow B(^3\Pi_{0_u^+}, v'' = n).$$

The oscillatory continuum emission observed in the region of 290 nm is much weaker, and is assigned to the bound-free transition:

$$f(0_g^+, v' = n) \rightarrow {}^1\Pi_{1u} \quad (2431 \text{ state}).\dagger$$

Perpendicular transitions, $\Delta\Omega = \pm 1$, have been observed to be weaker in general than parallel transitions, $\Delta\Omega = 0$, for a range of halogen valence ion-pair systems in absorption.[7] We have found in many instances that this propensity rule also holds for fluorescence. Both the bound-bound and bound-free fluorescence systems in fig. 2 clearly reflect the structure of the upper $f(0_g^+)$ state vibronic wavefunction. We have

† The orbital occupancy, $\sigma^i\pi^j\pi^{*k}\sigma^{*l}$ is given as ($ijkl$).

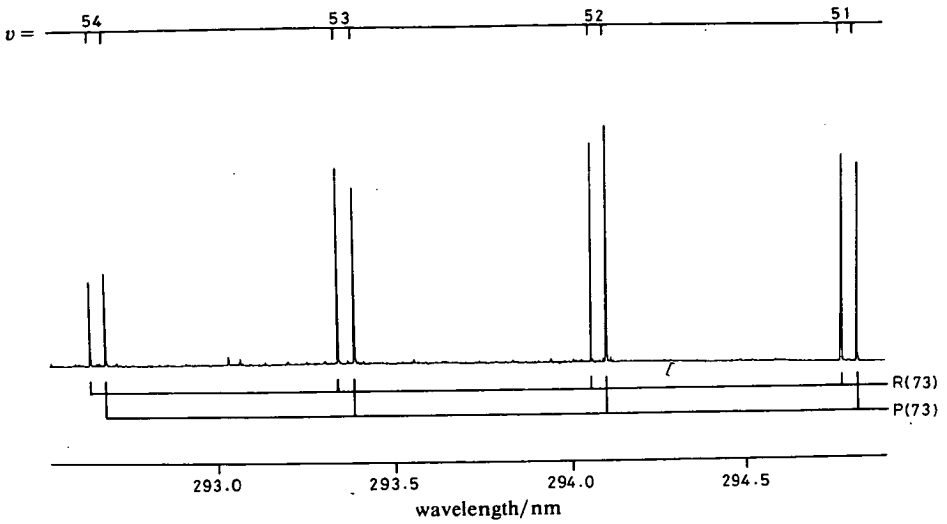

Fig. 1. OODR fluorescence excitation spectrum of the $f(0_g^+) \leftarrow B(^3\Pi_{0_u^+})$ transition of I_2 showing resolved P(73) and R(73) rotational lines from the intermediate $B(^3\Pi_{0_u^+}, v''=19, J''=73)$ rovibronic level.

recently carried out a detailed OODR study of the $E(0_g^+)$ state of I_2, lying in the first ion-pair cluster, and have also observed emission from low vibrational levels of the $E(0_g^+)$ state to the $^1\Pi_{1u}$ (2431) state.[8] Analysis of the observed oscillatory continuum systems involving this lower state should yield detailed information on the $^1\Pi_{1u}$ state, as both the $E(0_g^+)$ and $f(0_g^+)$ ion-pair states of I_2 are well characterised around their respective potential minima.[5,9]

A high-resolution dispersed fluorescence spectrum from a single rovibronic level ($v'=88$, $J'=70$) of I_2 ($f\,0_g^+$) is shown in fig. 3(*a*). An extensive fluorescence system is observed between 340 and 260 nm which is assigned to the transition:

$$f(0_g^+, v'=88) \rightarrow B(^3\Pi_{0_u^+}, v''=n).$$

Below $\lambda = 287.5$ nm the fluorescence is to bound levels of the $B(^3\Pi_{0_u^+})$ state, while at longer wavelengths oscillatory continuum structure is observed [*i.e.* fluorescence to the continuum of the $B(^3\Pi_{0_u^+})$ state]. We will present a more detailed analysis of this and similar spectra elsewhere.[8]

Chemical and Physical Quenching with Xe

Addition of Xe efficiently quenches the fluorescence from $f(0_g^+)$, and a new emission system appears around 253 nm [see fig. 3(*c*)]. This fluorescence system is readily assigned as $XeI(B\,^2\Sigma_{1/2} \rightarrow X\,^2\Sigma_{1/2})$, the excited XeI being formed in the reaction

$$I_2(f\,0_g^+) + Xe \rightarrow XeI(B\,^2\Sigma_{1/2}) + I(^2P_{3/2}).$$

In order to determine the vibronic threshold for this reaction, the intensity of chemiluminescence from XeI ($B\,^2\Sigma_{1/2}$) was monitored as a function of vibrational level in the $f(0_g^+)$ state. The following excitation scheme was adopted to provide good Franck-Condon overlap over the wide energy range of interest:

$$f(0_g^+) \xleftarrow[(n-17)P(69)R(69)]{} B(0_u^+) \xleftarrow[(17-1)P(70)]{} X(0_g^+).$$

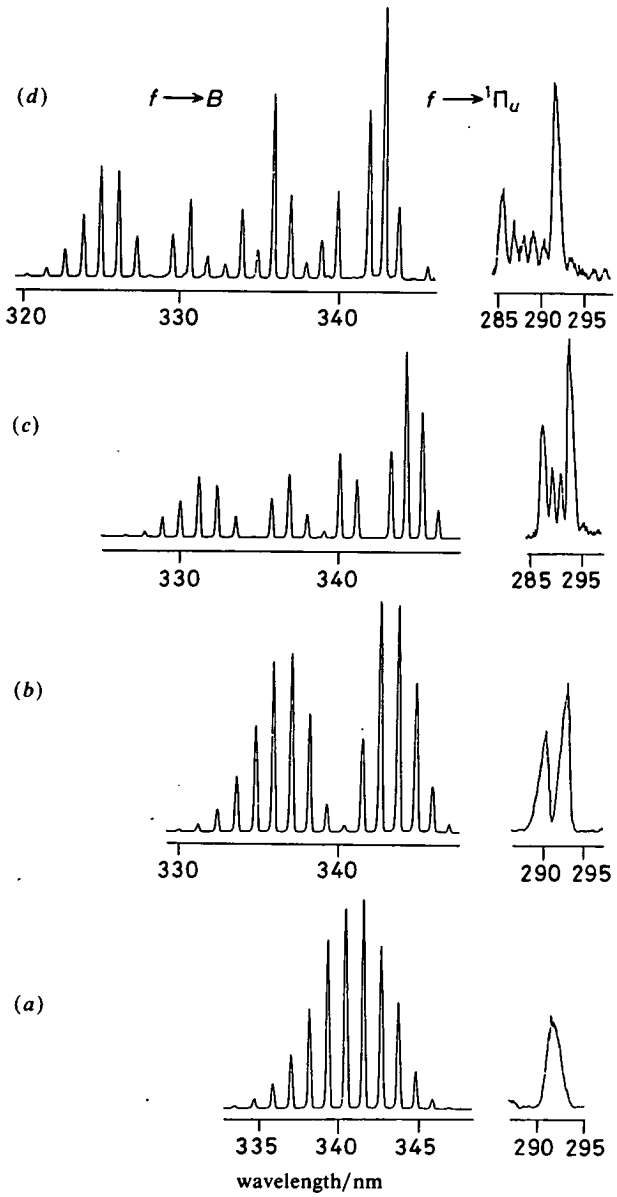

Fig. 2. Dispersed fluorescence spectra from single rovibronic levels of the $f(0_g^+)$ state to the $B(^3\Pi_{0_u^+})$ and $^1\Pi_{1u}$ (2431) states at high resolution: (*a*) from $I_2(f\,0_g^+,\ v'=0,\ J'=74)$, (*b*) from $I_2(f\,0_g^+,\ v'=1,\ J'=74)$, (*c*) from $I_2(f\,0_g^+,\ v'=3,\ J'=74)$, (*d*) from $I_2(f\,0_g^+,\ v'=5,\ J'=74)$.

The Franck–Condon factors vary substantially from level to level and the intensity of the XeI($B\,^2\Sigma_{1/2}$) chemiluminescence at 253 nm was ratioed against the intensity of fluorescence from $I_2(f\,0_g^+)$ with no Xe present, $(I_2^*)_0$. The weaker XeI($B\,^2\Sigma_{1/2} \rightarrow A\,^2\Pi_{3/2}$) system expected in the 330 nm region and any XeI($C\,^2\Pi_{3/2}$) emission are obscured by $I_2(f\,0_g^+)$ fluorescence.

We have found that the onset of the chemiluminescence lies between $v'=52$ and 57. The intensity of the chemiluminescence increases rapidly upon excitation to successively

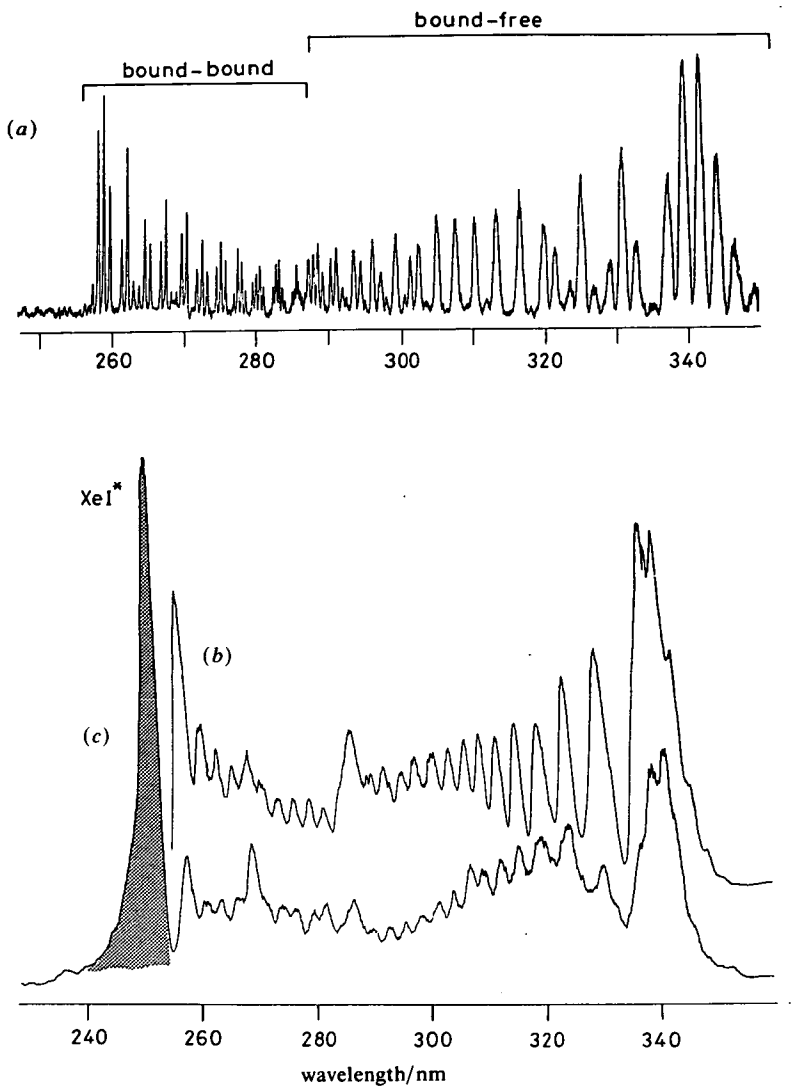

Fig. 3. Dispersed fluorescence spectra following excitation of $I_2(f\,0_g^+,\ v'=88,\ J'=70)$. (*a*) High-resolution spectrum of the $f(0_g^+) \rightarrow B(^3\Pi_{0_u^+})$ system $[p(I_2)=1.46\times10^{-2}\ \mathrm{kN\ m^{-2}}]$. (*b*) Low-resolution spectrum of the $f(0_g^+) \rightarrow B(^3\Pi_{0_u^+})$ system $[p(I_2)=1.46\times10^{-2}\ \mathrm{kN\ m^{-2}}]$. (*c*) Low-resolution spectrum of the $I_2(f0_g^+ \rightarrow B\,^3\Pi_{0_u^+})$ and $XeI(B\,^2\Sigma_{1/2} \rightarrow X\,^2\Sigma_{1/2})$ systems $[p(I_2)=1.46\times10^{-2}\ \mathrm{kN\ m^{-2}},\ p(Xe)=1.87\ \mathrm{kN\ m^{-2}}]$.

higher vibronic levels, as shown in fig. 4. These studies have been carried out under conditions where the mean relative translational energy available in the reactive encounter amounts to *ca.* 310 $\mathrm{cm^{-1}}$ ($T=300$ K), which prevents observation of a sharp threshold. It should also be noted that all these measurements refer to I_2 molecules excited to rotational levels $J'=68$ and 70 in the vibronic manifold of the $f(0_g^+)$ state. The reaction threshold, and indeed the reaction cross-section, could well depend upon the rotational quantum state. For the present we simply note that the levels $J'=68$ and 70 lie *ca.* 100 $\mathrm{cm^{-1}}$ above the $J'=0$ level and that this introduces a further small uncertainty into our determination of the threshold for reaction. Taking both of these factors into account, we estimate that the reaction threshold lies between 52 000 and 52 100 $\mathrm{cm^{-1}}$. This may

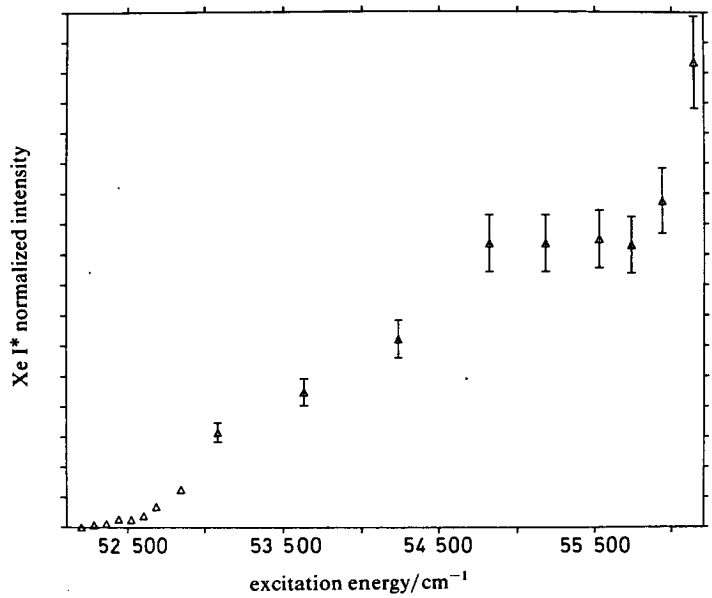

Fig. 4. Emission intensity ratio $(XeI^*)/(I_2^*)_0$ as a function of total excitation energy for the vibrational range $f(O_g^+, v' = 50\text{-}107)$. The levels $v' = 62$ and 93 correspond to excitation energies of 52 845 and 55 177 cm^{-1}, respectively.

be compared with the value of 52 300 cm^{-1} for the thermodynamic threshold, showing the absence of any substantial barrier in the entrance channel.

The total quenching (chemical + physical) rate constant for I_2 ($f\,0_g^+$) with Xe can be obtained by monitoring the quenching of f-state fluorescence as a function of the Xe partial pressure (Stern–Volmer method), provided that the radiative lifetime is known. Unfortunately the radiative lifetime of $I_2(f\,0_g^+)$ has not been determined, although lifetimes for the $D(0_u^+)$, $E(0_g^+)$, $\beta(1g)$ and $D'(2g)$ states have been reported (15, 28, 12 and 6.7 ns, respectively).[10–12] It is reasonable to assume that the radiative lifetime of the f-state lies in this range, and if we take a value of 20 ns, our data for quenching of the f-state fluorescence by Xe yield a total quenching rate constant of $(7.7 \pm 0.7) \times 10^{-10}$ cm^3 molecule^{-1} s^{-1}, for $v' = 93$.

Discussion

The threshold determined here for reaction (1) is very close to that determined for the reaction

$$I_2(D\,0_u^+) + Xe \rightarrow XeI(B\,^2\Sigma_{1/2}) + I(^2P_{3/2}) \qquad (2)$$

namely $52\,083 \pm 550$ cm^{-1}.[4] It appears, therefore, that the electronic identity of the reacting ion-pair state is not important. It is known that collisions with noble-gas atoms can induce efficient interstate transfer between ion-pair states in the same cluster.[2,3] However, little is known about transfer between states in different ion-pair clusters. Furthermore, highly efficient vibrational relaxation within the ion-pair manifold is known to occur with collision partners where only the physical quenching channel is open, and transfer to levels below threshold might compete with reaction. Our results suggest that collision with Xe causes mixing between the ion-pair states and that total vibronic energy is the most important factor influencing the reaction threshold. Thus we might expect

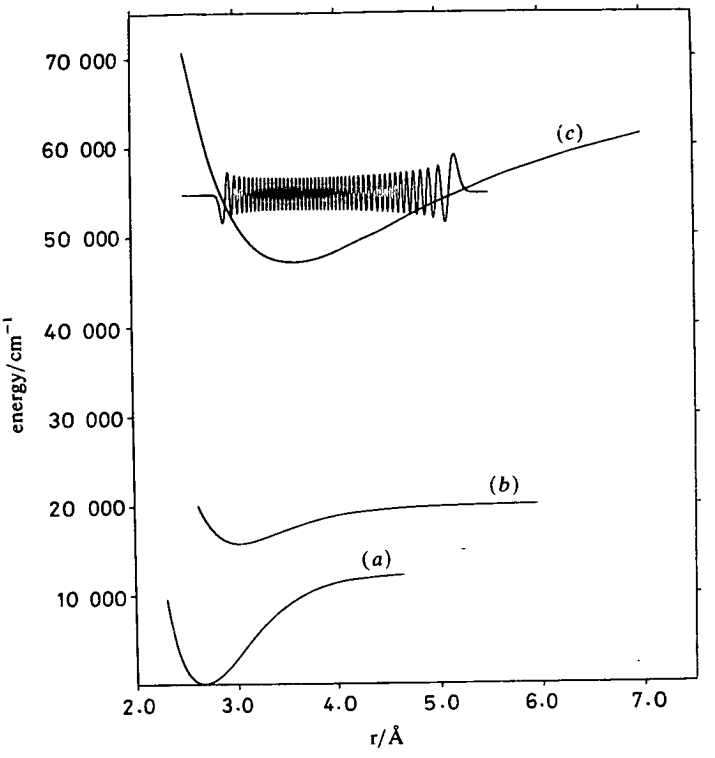

Fig. 5. Potential curves for (*a*) $X(^1\Sigma_g^+)$, (*b*) $B(^3\Pi_{0_u^+})$ and (*c*) $f(0_g^+)$ ($v'=93$) states of I_2; note the large amplitude of vibration for $v'=93$ of the $f(0_g^+)$ state.

several, if not all, of the ion-pair states of I_2 to have the same energetic threshold. It will be important in future work to establish branching ratios into the various exit channels, as these could vary substantially between different electronic states.

The mechanism for reaction between $I_2(f\,0_g^+)$ and Xe is thought to involve electron transfer from Xe into the core vacancy on $I_2(f\,0_g^+)$. This vacancy greatly enhances the effective electron affinity of I_2 and brings about efficient coupling to the $Xe^+I_2^-$ charge-transfer potential surface. Reaction then proceeds on this surface, as described previously.[13] Increasing the vibrational energy of the halogen partner results in extension of the ion-pair bond, and this will increase the collision cross-section. The soft attractive outer limb of the ion-pair potential is dominated by the Coulombic ($1/r$) term, thus for $v'=93$ the outer turning point has increased to 5.2 Å (see fig. 5), making a very large target for the incoming Xe atom.

The excitation function shows some evidence of structure at energies $>54\,800$ cm^{-1}, corresponding to excitation into I_2 ($f\,0_g^+$, $v'=88$) and beyond. This may possibly be due to interactions with Rydberg states or other ion-pair states. The production of higher electronically excited XeI* states or $I^*(^2P_{1/2})$ can be ruled out on energetic grounds. Formation of $I^*(^2P_{1/2})$ requires *ca.* 60 000 cm^{-1}, whilst the thermodynamic threshold for XeI* ($D\,^2\Sigma_{1/2}$) production is *ca.* 62 000 cm^{-1}.

We conclude that the ion-pair states of the halogens offer a very fertile area for the detailed study of the separate effects of electronic, vibrational and rotational energy on chemical reactivity and for the study of competition between chemical and physical quenching channels. At higher energy other channels are expected to open, leading to higher electronic states of the products, allowing the study of electronic correlations

between reactants and products. Information on product state vibrational and electronic distributions should also provide information on the nature of the potential surfaces controlling these processes.

A point of particular importance is the fine control of reactant rovibronic energy offered by studies involving excited ion-pair states. This contrasts with the much coarser tuning inherent in studies involving excited noble-gas atoms. Some flexibility has been achieved in excited-atom studies by varying the collision energy; however, this leads to a rapid fall in reaction cross-section with increasing translational energy.[13] With excited ion-pair states the reaction cross-section increases with vibronic energy. Clearly vibronic energy is more effective than translational energy in promoting reaction in rare-gas–halogen systems.

We thank the U.G.C. for an equipment grant, the S.E.R.C. for a studentship for A.H., and the Nuffield Foundation for the award of a Science Research Fellowship to P.R.R.L-S.

References

1 K. S. Viswanathan and J. Tellinghuisen, *J. Mol. Spectrosc.*, 1983, **101**, 285.
2 M. Martin, C. Fotakis, R. J. Donovan and M. J. Shaw, *Nuov. Cim.*, 1981, **B63**, 300.
3 R. J. Donovan, B. V. O'Grady, L. Lain and C. Fotakis, *J. Chem. Phys.*, 1983, **78**, 3727 and references therein.
4 B. V. O'Grady and R. J. Donovan, *Chem. Phys. Lett.*, 1985, **122**, 503.
5 J. C. D. Brand and A. R. Hoy, *J. Mol. Spectrosc.*, 1983, **97**, 379.
6 J. P. Perrot, A. J. Bouvier, A. Bouvier, B. Femelat and J. Chevaleyre, *J. Mol. Spectrosc.*, 1985, **114**, 60.
7 J. C. D. Brand, A. R. Hoy and S. M. Jaywant, *J. Mol. Spectrosc.*, 1984, **106**, 388.
8 R. J. Donovan, A. J. Holmes, P. R. R. Langridge-Smith, K. P. Lawley and T. Ridley, to be published.
9 J. P. Perrot, M. Broyer, J. Chevaleyre and B. Femelat, *J. Mol. Spectrosc.*, 1983, **98**, 161.
10 A. B. Callear, P. Erman and J. Kurepa, *Chem. Phys. Lett.*, 1976, **44**, 599.
11 J. Chevaleyre, J. P. Perrot, J. M. Chastan, S. Valignat and M. Broyer, *Chem. Phys.*, 1982, **67**, 59.
12 M. C. Sauer, W. A. Mulac, R. Cooper and F. Grieser, *J. Chem. Phys.*, 1976, **64**, 4587.
13 R. J. Donovan, P. Greenhill, M. A. MacDonald, A. J. Yencha, W. S. Hartree, K. Johnston, C. Jouvet, A. Kvaran and J. P. Simons, *Faraday Discuss. Chem. Soc.*, 1987, **84**, in press.

Paper 7/1887; *Received* 21*st October*, 1987